UC Berkeley
UC Berkeley Electronic Theses and Dissertations

Title
Using morphology and structure to tune solid-state thermal properties

Permalink
https://escholarship.org/uc/item/01h2v1jw

Author
Hippalgaonkar, Kedar

Publication Date
2013

Peer reviewed|Thesis/dissertation

Using morphology and structure to tune solid-state thermal properties

By

Kedar Hippalgaonkar

A dissertation submitted in partial satisfaction of the

Requirements for the degree of

Doctor of philosophy

In

Mechanical Engineering

In the

Graduate Division of the
University of California, Berkeley

Committee in charge:
Professor Costas Grigoropoulos, Chair
Dr. Arunava Majumdar,
Professor Chris Dames
Professor Peidong Yang, Outside Member

Spring 2013

Using morphology and structure to tune solid-state thermal properties

Abstract

Using Morphology and Structure to tune Solid-State Thermal Properties

By

Kedar Hippalgaonkar

Doctor of Philosophy in Mechanical Engineering

University of California, Berkeley

Professor Costas Grigoropoulos, Chair

Diffusive phonon transport in nanostructured materials has been a subject of intense interest and micro-fabricated platforms have been used to measure the thermal conductivity of nanowires. In this work, we demonstrate how the limits of heat transport can be tested in three novel material systems by extending this platform to probe material structure and provide a direct correlation to their thermal properties.

Phonons are lattice vibrations and their scattering in solids has largely been explained like collision of particles. Since the development of nanostructures, diffusive boundary scattering from large surface-to-volume ratio materials has been studied in nanowires and superlattices. To beat this diffusive scattering limit, we designed integrated silicon nanowires with rough surfaces with 30% reduction in thermal conductivity. Subsequently, we took a significant step further by making nanostructures with broadband roughness close to the dominant phonon wavelength (1-10 nm) at room temperature. The decrease in thermal conductivity of intrinsic silicon by a factor of ~30 from 140 W/m-K to 5 W/m-K in this sub-diffusive regime might be due to multiple scattering stemming from coherent phonon wave effects. Transmission Electron Microscopy (TEM) based techniques including three-dimensional tomography were then used to map out the morphology and find that we can reduce the thermal conductivity to as low as 1 W/m-K, while preserving the single-crystalline core, which is as low as that amorphous silicon or silica. Correlating the surface roughness and porosity to the measured thermal conductivity opens up a new paradigm to observing wave physics in thermal phonons at room temperature in nanomaterials.

Secondly, the platform developed previously was extended to be compatible with TEM, allowing us to characterize the crystal structure of measured nanowires. While phonon optics experiments in the 1970s showed a crystallographic direction dependent thermal conductivity, we performed the first 1-1 mapping of nanowire growth

direction and thermal conductivity in Bismuth Nanowires. In the boundary scattering regime with diameter 100 nm, a nanowire in the $[\overline{1}02]$ direction had k = 8.5 W/m-K, ~6 times higher than a nanowire in the $[110]$ direction with k = 1.5 W/m-K.

Finally, this thesis also studies tapered Vanadium Oxide beams to study asymmetric phonon physics that manifest in temperature dependent thermal rectification. The interplay between electrons and phonons and the possibility of asymmetric scattering rates prompted us to look closely at the existence of Metal-Insulator interfaces that could result in thermal rectification. Between 150K and 340K, the V_nO_{2n-1} phases could be either metallic or insulating with nanoscale domains. We performed high resolution Auger spectroscopy on single-crystal Vanadium Oxide beams that show a stoichiometry variation and measured thermal rectification as high as 22%. The rectification behavior turns off (<4%) once the whole beam reaches the insulating phase, higher than 340K.

Our platform thus couples materials characterization, especially TEM, with thermal property measurement to enhance understanding of thermal phonons.

In memory of Shri. Jagannath Rao Hippalgaonkar

and

Dedicated to my grandfather, Dr. Swanand Santpur

TABLE OF CONTENTS

List of Figures:

List of Tables:

Acknowledgements

My first visit to Berkeley was filled both with awe and a sense of belonging. It is laid back, serious and inspiring all at the same time, just like I aspired to be. Arun fortified this spirit when I first met him, when he talked about science and cricket with equal passion. I knew I fit in. And I knew this is where I'd pursue my passion for doing something original. When Arun was at Berkeley in the first two years of my PhD, the group meetings and happy hours were an absolute treat. I learnt to ask the right questions; the answers followed. I learnt to 'dig deep'. And I learnt that the folks in my lab were at their incisive uninhibited best when slightly inebriated. Big picture perspectives were gained, egos were shed and 'game-changing' ideas were discussed. I can only imagine how things would've been had Arun not left for ARPA-E in 2009.

But, it laid the foundation for fabulous friendships. Joe, Jon, Kaal, Chris, Robert, Renkun, Duan, Yang, Jayakanth, Dusan, Jae Hun, Dongyan, Baoling, Karma, Shannon and Cheng were partners in crime. This was the best part of being in Arun's lab. Renkun was my mentor and an epitome of efficiency; I hope I inherit at least a fraction of his ability to get things done. Much of how I picture the physics of heat is courtesy of his insight. JK is a great friend, and the innumerable discussions about science, life, morality, pedagogy, ethics, north gate 'sightings' etc. were truly rewarding (not so sure about the last one…). Dusan is Yin to my Yang. Even though his approach to life is different from mine (and how!), we share the same values. Together, we've learnt what the important things in life are, and I'll strive to achieve these in my future. Jae Hun is a yogi, and I hope he'll never regret not giving 100% while he's in Korea!

Special thanks to Jongwoo, for spending painstaking hours with his 'chopstick fingers' and getting the nanowires to behave. Peter showed me that the TEM was so much more than 50+ buttons and a cool-looking green beam in an otherwise dark room. Chris Dames was a constant source of support and encouragement in the last two years of my doctorate, and gave valuable practical advice. Through him, his group members always gave my research a priority, which I will always be thankful for. Ramesh showed me the ropes and was always full of real-life advice that I suspect are his anglicized renditions of Thirukural couplets. Xiang was extra-ordinarily supportive in the 'last year' of my PhD. Thanks to Costas Grigoropoulos for being available to sign off on all administrative matters in Arun's absence.

The 1635 MLK gang, now that's a legacy! Ganesh, Gopal, Shivang, Varun, Surya, and Buxi will remain my strongest Berkeley association. Cheers to late night 'bhasad', and thanks for providing an escape from an otherwise mundane PhD. Vijay, Aalok, Anjan - you guys will remain the best of pals forever, like it or not! Thank you Srini Uncle,

CHAPTER 1

HEAT TRANSFER IN SOLID STATE SYSTEMS

1.1 INTRODUCTION

Propagating electricity, light, sound or heat through solids has been of immense interest to human beings right from the advent of Science and Technology. Understanding electronic transport through solids was a natural result of attempts to discern the internal electronic structure of atoms. The picture of how electrons are occupied around the solid nuclei consisting of neutrons and protons was developed in the early 20th century (1911-13) by Ernest Rutherfold and Niels Bohr, even before the era of quantum mechanics. The motion of the valence electrons as a free electron gas was sufficient to understand simple transport phenomena, for example, Ohm's law and the relation between the electrical and thermal conductivity of metals. A solid that is thus opaque to the naked eye is transparent to these conduction electrons due to Pauli's Exclusion Principle, allowing electrons the freedom to move freely without being scattered by other electrons or by the ionic core. Further, in the case of a periodic lattice in a crystal, the picture of Energy Bands was subsequently developed allowing for a distinction between metals, semiconductors and insulators as well as a clearer understanding of magneto-transport. The insight gained from this band picture was that electrons were not traversing as individual particles through ions inside the solid core, instead they moved as wave-packets in such a way that they didn't see the ionic core. However, in order to understand the motion of these electrons under the influence of an external applied electric field, a simple kinetic model suffices, which is discussed briefly in this treatise.

Transport of light through vacuum, on the other hand, is well understood and has been a cornerstone of physics since James Clark Maxwell's equations in 1861, with the speed of light in vacuum, c being a fundamental constant. Absorption, transmission and other forms of manipulation of light in solids have also been studied extensively in the past century and are directly related to the band structure of solids. If light does not interact with solids, then there is no energy transfer from the EM wave to the solid. The starting point to understand propagation of light through solids is observing that they behave as

waves described by Maxwell's Equations. It can be shown that the EM wave travels at a speed c/n, where n is the real part of the refractive index of the solid. The refractive index is intimately related to the dielectric function of the solid, which defines the response of a crystal to the EM field. Since the dielectric function depends on the electronic band structure of the solid, a direct link between optical and electronic energy transfer is established.

While there is a plethora of work that focuses on electronic and EM wave based energy transfer in solids, the focus of this thesis is on energy transfer in the form of heat in crystalline solids. Similar to the behavior of electrons and light in matter, the transport of heat is not easy to interpret if we only consider the vibration of atoms about their equilibrium positions, where they transfer energy only if their motion results in an excess of energy. It is difficult to fathom how such a simple mechanism can result in a very high thermal conductivity in an electrically insulating crystal such as Diamond (2000 W/m-K) or Silicon (140 W/m-K) at room temperature, whereas the amorphous phase of the same material has a thermal conductivity orders of magnitude smaller (~1 W/m-K). In metals, the electrons transfer heat, resulting relatively high values of conductivity, such as Copper (300 W/m-K). In order to understanding this fascinating phenomena of how relatively massive atoms can transfer energy efficiently in the form of heat in crystalline solids, one must develop a framework where the individual particle model is replaced by that of a collective motion (similar to the band picture of electrons). The first part of this thesis will focus on reviewing existing understanding of thermal energy of solids as normal modes of vibration. This normal basis allows heat waves to be described as quanta of thermal energy called 'phonons'. The phonons can thus be described to be carrying heat with group velocities close to the speed of sound in the solid (the limits of these will be discussed in detail in later sections). As will be seen in this section, the atoms need to be treated as resting in a harmonic potential with quadratic displacement about their equilibrium state. Hence, with this normal mode basis, we can then treat the phonons as orthogonal to each other, but undergoing scattering due to any anharmonicities. Another convenience is treating phonons as a kinetic gas where they can further scatter from any imperfections in the crystal, including boundaries. In addition, this description allows the identification of relevant length scales of the system, in particular, the wavelength, mean free path and the coherence length of the phonons: all of which will be described in detail in this section. In order to understand the basics of phonon transfer in dielectric solids and how this can be manipulated, let us describe the mathematical basis for phonons first.

1.2 PHONONS

1.2.1 Classical Lattice Vibrations

A classical picture of masses connected by springs is sufficient to identify the relationship between energy and how this energy is distributed amongst lattice waves that have wavelengths as integer multiples of the lattice spacing in a periodic lattice. In other words, one can derive a dispersion relation that describes the energy occupation with different wavevectors in a discrete lattice, similar to the dispersion relation of electrons or photons.
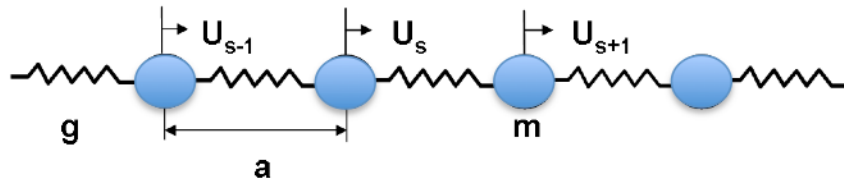
Figure 1.1 One Dimensional Spring Mass System

Consider the picture in Figure 1.1 where the atoms are separated by a lattice constant a, each with a mass, m and connected by a spring with spring constant g. If the sth atom is displaced by a distance u_s, the force equation for that atom can be written as:

$$m\frac{d^2 u_s}{dt^2} = g\left(u_{s+1} + u_{s-1} - 2u_s\right)$$

(1.1)

if only nearest neighbor interactions are considered. This is similar to a wave equation with a solution of the form

$$u_s = u_0 \exp\left(-i\omega t\right)\exp\left(inka\right)$$

(1.2)

Here, ω is the angular frequency and $k = 2\pi/\lambda$ is the wavevector, where λ is the wavelength. Using this ansatz, the dispersion relation can be derived as follows:

$$\omega = \sqrt{\frac{2g}{m}}\left(1 - \cos ka\right)^{\frac{1}{2}}$$

(1.3)

There is an obvious limit to the smallest wavelength possible, which has to be λ = 2a.

Hence, the range of possible wavenumbers spans -π/a < k < π/a. Equation (1.3) can be plotted as the dispersion relation as shown in Figure 1.2 below:
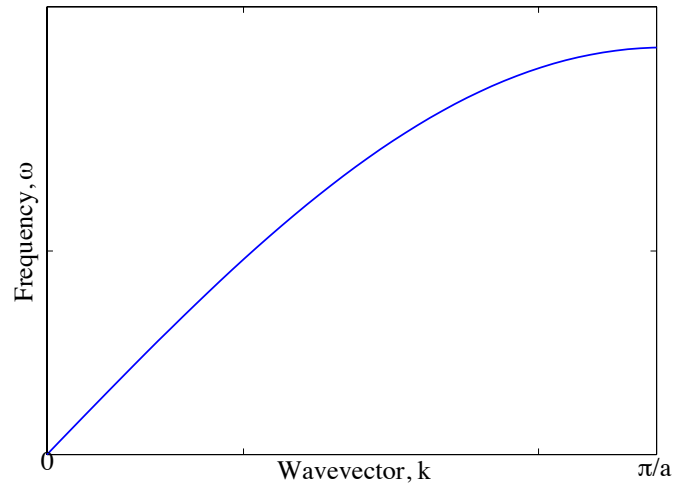
Figure 1.2 One Dimensional Dispersion Relation for phonons

In the classical limit, as *ka* → 0, the dispersion relation can be approximated as:

$$\omega = \sqrt{\frac{g}{m}} ak \tag{1.4}$$

The speed of phonon wave propagation is defined as its group velocity given by v_g = *dω/dk*. In this linear regime, especially in the long wavelength (classical) limit it is a constant and is equal to the speed of sound in the crystal. Hence, heat travels close to the speed of sound in a crystalline solid and the branch shown in Figure 1.2 is called the acoustic branch of the dispersion relation. In the other extreme, when the wavelength of is very short (*k* → π/a), the atoms vibrate out of phase with each other and the group velocity reduces to zero. Hence, no energy transfer occurs in this limit. Of course, real crystals are three dimensional in nature. In order to address the transport of energy via atomic vibration in real solids, we must first define a mathematical construction that enables physical understanding and captures important symmetry effects.

4

1.2.2 Lattice Structure and the Brillouin Zone

A perfect three- dimensional crystal would have translational symmetry as defined by the *lattice* and the *basis vectors*. A *lattice* is a periodic array of points in space, which define any atom in the crystal, $\mathbf{R} = n_1\mathbf{a_1} + n_2\mathbf{a_2} + n_3\mathbf{a_3}$, where n_1, n_2 and n_3 are arbitrary integers and $\mathbf{a_1}$, $\mathbf{a_2}$ and $\mathbf{a_3}$ are translational vectors. A *basis* is the building block of the lattice consisting of an atom or a group of atoms inside a *primitive unit cell* that are then translated using the *primitive translation vectors* to reconstruct the lattice. Note, that for a multi-atom basis, $\mathbf{R}$ doesn't describe every atom in the crystal, instead describing every repeating basis. To understand this more clearly, let us consider the case of Silicon. As a diamond cubic crystal structure, the basis is comprised of two Silicon atoms, where two face-centered cubic primitive unit cells are displaced from each other by one-quarter of a body diagonal as illustrated in Figure 1.3.
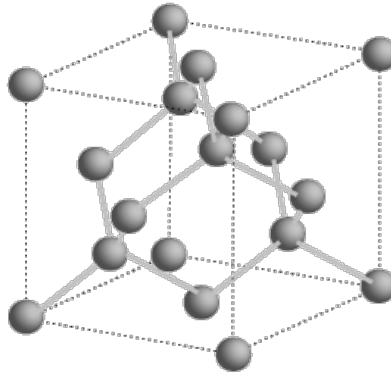
Figure 1.3 Crystal Structure of Cubic Silicon

Such a translational invariance that defines the symmetry of the crystal is very powerful as it indicates that an intrinsic property of the crystal doesn't change under any translation by the lattice vectors. The strength of this construction can be seen more clearly once a Fourier Transform of the primitive lattice vectors is taken to define the crystal in *reciprocal space*. That is,

$$b_1 = 2\pi\frac{a_2 \times a_3}{a_1 \cdot a_2 \times a_3}; \quad b_2 = 2\pi\frac{a_3 \times a_1}{a_1 \cdot a_2 \times a_3}; \quad b_3 = 2\pi\frac{a_1 \times a_2}{a_1 \cdot a_2 \times a_3} \quad (1.5)$$

where $\mathbf{b_1}$, $\mathbf{b_2}$, $\mathbf{b_3}$ are primitive reciprocal lattice vectors that help define any reciprocal lattice vector, $\mathbf{G}$ given by:

$$G = \upsilon_1 b_1 + \upsilon_2 b_2 + \upsilon_3 b_3 \quad (1.6)$$

A *Brillouin Zone* is defined as a primitive cell in the reciprocal space that helps define the reciprocal lattice. Once this Fourier Transform based construction is complete, we can realize that the set of reciprocal lattice vectors determines in entirety the requirement for diffraction due to elastic scattering of any form of waves from the lattice structure. In other words, the first Brillouin Zone can uniquely identify all symmetries of the constituent crystal and is used extensively in diffraction-based studies of crystal lattices. Figure 1.4 shows the first Brillouin Zone of a face-centered cubic crystal.
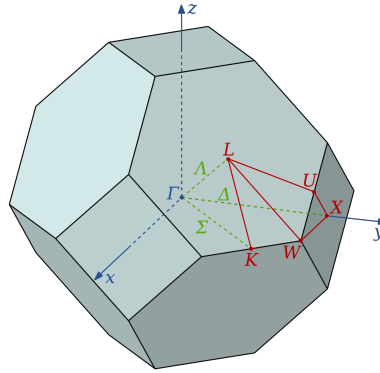
Figure 1.4 First Brillouin Zone of a 3D fcc crystal

The *Γ-point* is the center of the Brillouin Zone. In the directions (100), (010) and (001), the *X-point* defines where the x,y and z axes meet the edge of the zone. Further, the most closely packed direction along the body diagonal of the crysal in the (111) direction meets the zone edge at the *L-point*. These are noted to be high symmetry directions in the crystal structure and the significance of these different directions will be revisited later in this thesis. The reciprocal lattice vector, **G** joins the *Γ-points* of two adjacent Brillouin Zones and thus is sufficient to uniquely define the crystal. Interestingly, this is related to the range of independent values of the allowed wavevectors, *k* in a discrete lattice as described in Section 1.2.1.

In a one-dimensional linear lattice described above, $-\pi/a < k < \pi/a$ gives the range of the first Brillouin Zone. The difference from continuum is thus clear in this new construction in reciprocal space. While in the classical limit of lattice vibrations, as $a \rightarrow 0$, $k_{max} \rightarrow \infty$. However, in the discrete lattice case, values of *k* outside the first Brillouin Zone only serve to replicate solutions for the elastic waves as any value of *k* outside these limits can be brought back to the first Brillouin Zone by subtracting **G** where n is any integer. It is instructive to repeat the lattice vibration analysis for a two-atom basis. Following Kittel et. al.[1] consider the case of two atoms of different mass, m_1 and m_2 vibrating in parallel planes interacting with each other with a force constant, *g* as illustrated in Figure 1.5.

6
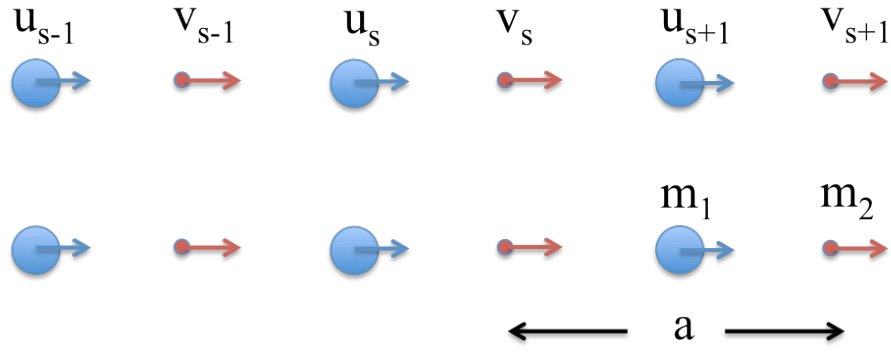
Figure 1.5 Two atom basis vibration system

The force equations for the plane of atoms is given by [1]:

$$m_1 \frac{d^2 u_s}{dt^2} = g(v_s + v_{s-1} - 2u_s);$$

$$m_2 \frac{d^2 v_s}{dt^2} = g(u_{s+1} + u_s - 2v_s);$$

(1.7)

Assuming plane wave solutions again, one can obtain a dispersion relation for the two-dimensional case as well. There will be two solutions for $\omega = f(k)$, resulting in two branches – *acoustic and optical*. These are easy to understand in the long-wavelength limit, where $ka \to 0$. The dispersion relation can then be shown to reduce to:

$$\omega = \sqrt{\frac{2g(m_1 + m_2)}{m_1 m_2}} \qquad optical\,branch$$

$$\omega = \sqrt{\frac{2g}{(m_1 + m_2)}} ka \qquad acoustic\,branch$$

(1.8)

This splitting of the dispersion relation into two branches can also occur if the spring constants are different and the masses of the two-atom basis are the same, as could typically occur in a real crystal. This analysis can be extended to a three-dimensional structure as well. The key physics here is that when there are p atoms in the primitive cell (multiple atom basis), there are $3p$ branches to the dispersion relation, of which 3 are acoustic and the rest $3p$-3 are optical branches. For example, consider the case of silicon, which has two atoms in the primitive cell. Hence, there are 6 branches, with 3 acoustic and 3 optical branches. The optical branches typically have very low group velocity, as can be seen from Equation (1.8) and hence carry very little energy. The atoms here are vibrating out of phase with each other. In a polar crystal these can be very useful for coupling with EM waves, which have an oscillating E-field as well. Furthermore, in each

7

branch of the dispersion relation, there are two polarizations, *longitudinal* and *transverse*. In summary, for two-atom silicon, there are six branches: one LA (longitudinal acoustic), two TA (transverse acoustic), one LO (longitudinal optical) and two TO (transverse optical). Figure 1.6 shows the dispersion relation of Silicon that accounts for all the modes in different symmetry directions.
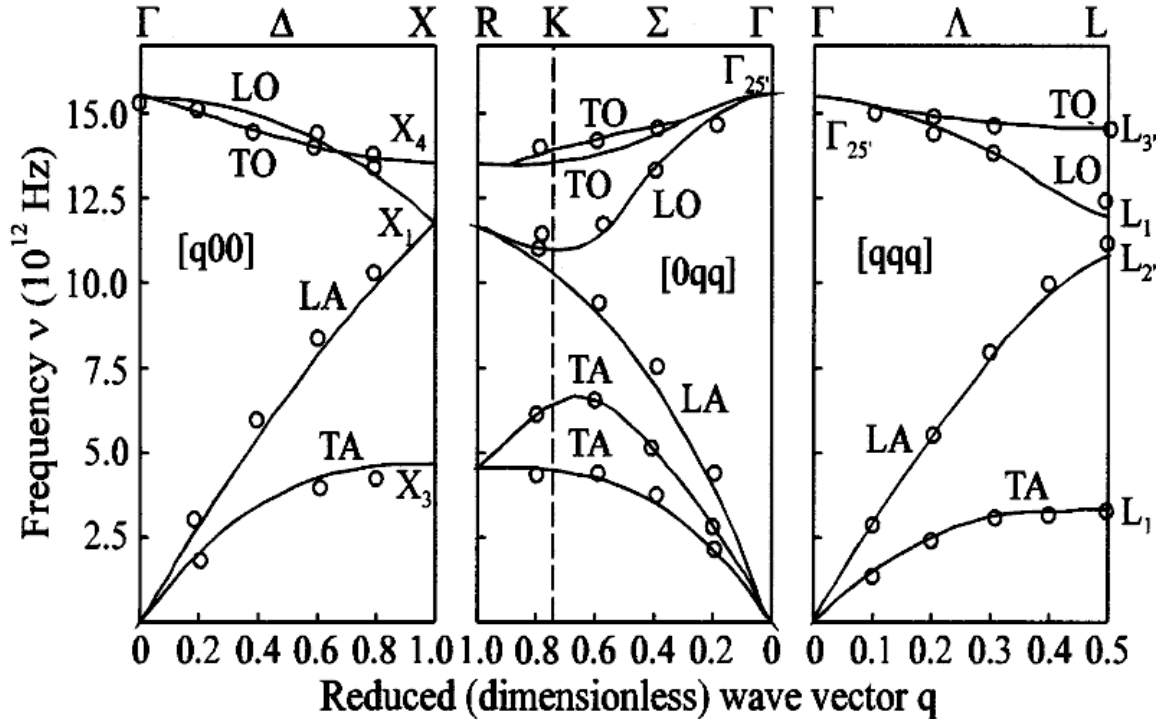
Figure 1.6 Dispersion relation of silicon (adapted from the Dolling [2]). The zone center is the Γ-point, while the L- and X-points are shown as described in the text.

Heat, as described before, is mainly carried by the acoustic modes having a finite group velocity. Consider energy propagation in the long-wavelength limit in the (100) direction (Γ-X direction in the Brillouin Zone (BZ)). The LA modes have a group velocity $v_g = d\omega/dk$ ~8440 m/s, while the TA modes carry energy slower at around 5860 m/s (both in the long wavelength limit, close to the BZ center). It is a matter of debate whether the LA or the TA modes carry a larger fraction of the heat [3]. Further, it can be seen from Figure 1.6 that the group velocity is direction dependent. Also, the two TA modes lie on top of each other in the X- (along the axes) and L- (body diagonal) directions. However, in the K- (intersection of two hexagonal faces of the BZ, see Figure 1.4) direction, the TA modes actually have two different group velocities. The significance of direction-dependent group velocities will become clearer in Chapter 4 when we look at the thermal properties of single-crystalline Bismuth nanowires grown in different crystallographic directions. Also, the role of the group velocity and whether it can be manipulated remains

an interesting problem in solid-state systems and will be addressed later on in Chapter 1 and also in Chapter 3.

1.2.3 Phonons

The connection between energy and travelling waves can be clearly understood by the dispersion relation described in the previous sections. However, there is a correlation between how a single atom oscillates about its equilibrium position and how energy is transferred by lattice vibrational waves. Further, discreteness of the lattice plays a role, which has not been considered in the continuum picture. Both of these effects are non-trivial, leading to important insight on how heat moves in a solid.

Firstly, when the equation of motion (1.1) was considered for an atom in a linear chain, the dispersion relation details out the possible energy states that can be occupied. In reality, each atom can be treated as a harmonic oscillator and a general quantum mechanical framework can be derived to describe the quantization of energy states. The Hamiltonian, H for the system of N atoms in a one-dimensional chain with a harmonic potential is given by:

$$H = \sum_{i=1}^{N} \left(\frac{p_i^2}{2m} + \frac{1}{2} m\omega^2 (x_i - \bar{x})^2 \right)$$

(1.9)

where p_i and x_i are the momentum and position operators for the ith atom with mass m. Hence, we are solving the time-independent Schrödinger's Equation:

$$H\psi = E\psi$$

(1.10)

Using an energy raising/lowering operator defined as [4]

$$a_{\pm} \equiv \frac{1}{\sqrt{2\hbar m\omega}} \left(\mp ip_i + m\omega x_i \right)$$

(1.11)

It can be shown that the eigenstates of energy are given by:

$$E_n = \left(n + \frac{1}{2} \right) \hbar\omega$$

(1.12)

where n is an integer and $\hbar\omega/2$ is the zero-point energy. The energy levels allowed for the quantum mechanical oscillator, E_n, are thus discrete. These discrete or quantized vibrational states of energy are called *phonons*. The energy quantum is hence $\hbar\omega$. Thus,

now the allowed vibrational energies of crystal waves are observed to be quantized. The physical picture that develops is that propagation of energy is like a packet of energy consisting of *n* phonons at any energy level. In order to link this observation with the energy dispersion relation developed in the earlier question, we must answer the central question: how many phonon states are available per unit frequency range? This is defined as the Density of States, *D(ω)* and is directly related to the discreteness of the lattice, as is discussed below.

In order to determine the density of states that determine the energy level occupation, again the reciprocal lattice concept becomes important. Consider periodic boundary conditions over N primitive cells within a cube with side L. Periodic Boundary Conditions hence require that:

$$\exp\left[i\left(k_x x + k_y y + k_z z\right)\right] \equiv \exp\left[i\left(k_x(x+L) + k_y(y+L) + k_z(z+L)\right)\right] \quad (1.13)$$

where *k* is the wavevector or the inverse wavelength in reciprocal space. Then, there is one allowed value of *k* per unit volume $\left(2\pi/L\right)^3$ in *k-space*. The number of orthogonal plane wave solutions to the Hamiltonian is equal to the number of atoms in the system. Hence, there are N normal modes in the system. Thus, we see that the number of states, N, in three dimensional reciprocal space is:

$$N = \frac{\frac{4}{3}\pi k^3}{\left(\frac{2\pi}{L}\right)^3} = V \cdot \frac{k^3}{6\pi^2} \quad (1.14)$$

where $V=L^3$ is the volume of the crystal. Then, the density of states, *D(ω)* is defined as:

$$D(\omega) \equiv \frac{dN}{d\omega} = \frac{dN}{dk} \bigg/ \frac{d\omega}{dk} = \frac{Vk^2}{2\pi^2 v_g} \quad (1.15)$$

Here, $v_g=d\omega/dk$ is the group velocity approximated for an isotropic dispersion relation as is shown in Figures 1.2 and 1.6. When $v_s \sim v_g = \omega/k$, this approximation is called the Debye Approximation [5]. Let us consider the thermal vibrational energy at any temperature. It can be loosely estimated that $\hbar\omega \approx k_B T$ (explained below), where $\hbar$ is the reduced Planck's constant, k_B is the Boltzmann Constant and T is the absolute temperature. At room temperature (~300K), we can then estimate that $\omega \sim 6.25$ THz. Looking at Figure 1.6, at room temperature for silicon, all of the TA modes and most of the LA modes are energized and carrying energy. One can then see the limitation of the linear Debye Approximation, as the zone-edge TA modes do not travel with a large sound velocity. In fact, as discussed earlier, the zone-edge phonon modes mostly behave as standing waves and carry no heat at all, though there are exceptions. Therefore, while the Debye

Approximation, $\omega = v_s k$, captures the dispersion relation accurately for lower temperatures, inaccuracies becoming significant for the higher energy modes occupied at higher temperatures. Nevertheless, this approximation allows us to simplify the mathematics sufficiently to gauge the physics of heat transfer.

1.2.4 Phonon Statistics and Heat Capacity

The equilibrium distribution of phonons follows the Bose-Einstein distribution and is given as [6]

$$\langle n \rangle = \frac{1}{\exp\left(\dfrac{\hbar\omega}{k_B T}\right) - 1} \tag{1.16}$$

Then, using Equation (1.12), the total energy in the crystal is [7]:

$$E = \sum_{k,p}\left(\langle n \rangle_{k,p} + \frac{1}{2}\right)\hbar\omega_{k,p} \tag{1.17}$$

where p is the polarization of the phonon mode and k is the wavevector. The summation is over the entire Brillouin Zone for both transverse and acoustic modes. At higher temperature, $\langle n \rangle \approx k_B T/\hbar\omega$ which gives $\langle E \rangle \approx k_B T$. This is a general estimate for the thermal vibrational energy and has been used above in estimation of phonon energy modes to gauge the validity of Debye's linear approximation as well. Since for a bulk solid the discretization is very dense, the summation over the Brillouin Zone can be replaced by an integral in *k-space*, which can then be transformed to an integral in energy by using the Density of states $D(\omega)$ to convert variables from k to ω as below:

$$E = \sum_{p}\int \frac{dk}{(2\pi)^3}\left(\langle n \rangle_{k,p} + \frac{1}{2}\right)\hbar\omega_{k,p};$$

$$E = \sum_{p}\int d\omega D_p(\omega)\left(\langle n \rangle_{p} + \frac{1}{2}\right)\hbar\omega_{p} \tag{1.18}$$

The heat capacity of the crystal can then be defined as:

$$C_v \equiv \frac{\partial E}{\partial T} = \sum_{p}\int d\omega D_p(\omega)\frac{\partial \langle n \rangle_{p}}{\partial T}\hbar\omega_{p} \tag{1.19}$$

11

In order to capture all the phonon modes present in the Brillouin Zone, we can define a cutoff wavevector, $k_D = (6\pi^2 N/V)^{1/3}$ from Equation (1.14). $\eta = N/V$ is an intrinsic property of the crystal, giving the number density of atoms. Then, a *Debye Temperature,* θ_D can be defined as the upper limit to the integral in Equation (1.19):

$$\hbar\omega_D = k_B\theta_D; \quad where\, \omega_D = v_g k_D$$

$$Hence, \theta_D = \frac{hv_g\left(6\pi^2\eta\right)^{1/3}}{k_B} \tag{1.20}$$

This can be used to simplify Equation (1.18) to [7]:

$$C_v = 9\eta k_B \left(\frac{T}{\theta_D}\right)^3 \int_0^{3\theta_D/T} \frac{x^4 dx}{\left(e^x - 1\right)^2} \tag{1.21}$$

Equation (1.21) is very insightful in the low and high-temperature limits. When $T \ll \theta_D$, $C_v \approx 234\eta k_B\left(T/\theta_D\right)^3$ for a 3-dimensional solid. This has been observed experimentally for many solids, see the illustration in Figure 1.7 for silicon below [8]. The other extreme is when $T \gg \theta_D$. Then, Equation (1.21) tends to a constant independent of temperature given by $C_v \approx 3\eta k_B = 3R$, where R is the universal gas constant. This is called the Dulong-Petit Limit, which can also be derived by taking into account all six degrees of freedom of every vibrating atom in the lattice structure. Then, from Equipartition of Energy, the energy per atom is given by $6*(1/2k_BT)=3k_BT$. Hence, for a number density of atoms given by η, $C_v = \partial E/\partial T = 3\eta k_B$. Most solids asymptote to this value irrespective of whether they are metals, insulators or semiconductors. As can be seen in Figure 1.7 for silicon, the high temperature value is ~25 J.mol^{-1}.K^{-1}, which is very similar to Copper or Lead. This observation was perplexing to scientists in the early 20th century – how can a metal with a very large electron density have the same specific heat at high temperature as an insulator with no itinerant electrons? The answer lies in the fact that most of the internal energy is carried by the phonons, which follow the Bose-Einstein Distribution. Hence, at any temperature T, the energy is carried by all phonons occupying the dispersion relation. In a metal, things are different, since the electrons follow the Fermi-Dirac Statistics, which forces only electrons within an energy bandwidth of ~k_BT of the Fermi Level to contribute to the specific heat. This number density is much smaller and hence the heat capacity due to electrons is much smaller.
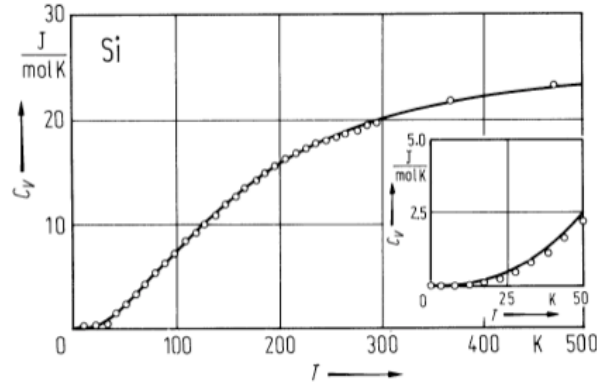
Figure 1.7 Specific heat at constant volume of crystalline Silicon. At low temperatures, $C_v \propto T^3$ while at higher temperatures, C_v approaches the Dulong-Petit Limit.

1.2.5 Kinetic Theory of Gases and Thermal Conductivity

Now that we have defined phonons as particles, it is possible to make an approximation that gives us some physical insight on how phonons transfer heat in the presence of a temperature gradient. This process has historically been understood as diffusive and is illustrated by Fourier's Law:

$$q = -\kappa \nabla T \qquad (1.22)$$

where q is the local heat flux (W.m^{-2}), ∇T is the temperature gradient (K.m^{-1}) and κ is then defined as the thermal conductivity (Wm^{-1}K^{-1}). This ubiquitous relationship can be derived under some approximations using Boltzmann Transport or Kinetic Theory. One approach to understanding the origin of κ is using the kinetic theory of gases. This assumes that thermal transport in a solid under a temperature gradient occurs with 'heat-carrying particles' scattering off each other and the boundaries of the system, in the process transferring energy in a diffusive fashion. Now we know that one can identify these particles in a solid as phonons. However, to further breakdown the thermal conductivity and gain more insight on what determines this intrinsic property of any material, we will have to dig deeper into how these phonon particles interact with each other, imperfections in the crystal as well as boundaries of the system. We'll also keep in mind the limitations of approximating the phonons purely as particles, since in reality, these are wave-like lattice vibrations that are normal modes.

The kinetic theory of gases describes a large number of small particles moving about randomly colliding with each other and boundaries of the system. A few basic assumptions are central to building this theory. All collisions are considered to be elastic, conserving energy. The large number of particles allows applying statistical averaging to obtain macroscopic properties of the gas. The only interaction between particles is collisions. An important time (and subsequently length) scale results from assuming that

13

the time during collisions is much smaller than the time between collisions. Hence, one can define a mean free time (length) as $\tau_\ell(\ell)$. For $t < \tau_\ell$, particles travel ballistically. However, to define a relaxation time, one has to consider many collisions to reach local thermal equilibrium. Also, energy and momentum relaxation times can be different. While an elastic collision might conserve energy, the momentum can change, thus typically momentum relaxation times are shorter than energy relaxation times. All particles are treated classically with equations defining their motion being time-reversible. This picture provides an intuitive understanding of how energy is transferred with a large number of phonons being occupied at any particular temperature subject to Bose-Einstein statistics.

Consider a particle moving across a region in the x-direction through a temperature difference of ΔT as shown in Figure 1.8.
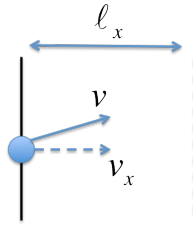
Figure 1.8 Motion of a particle carrying mass and energy across an average distance ℓ_x under temperature gradient ΔT with a velocity in the x-direction given by v_x

Then,

$$\Delta T = \frac{dT}{dx}\ell_x = \frac{dT}{dx}v_x\tau \qquad (1.23)$$

Here, τ is the average time between collisions. From the continuity equation, the net flux of energy is given by:

$$j_U = -n\bar{v}_x[c\Delta T] \qquad (1.24)$$

where the energy change experienced by the particle is given by $c\Delta T$, c being the specific heat of the particle moving with an average velocity $\bar{v}_x$ in the x-direction. Then, considering an average of the momentum in the x-direction, $\bar{v}_x^2 = \frac{1}{3}\bar{v}^2$. Substituting Equation (1.23) in (1.24) we get

$$j_U = -\frac{1}{3}n\bar{v}^2c\tau\frac{dT}{dx} = -\frac{1}{3}Cv\ell\frac{dT}{dx} \qquad (1.25)$$

Here, $\ell \equiv v\tau$ is the mean free path of phonons and $C \equiv nc$ is the specific heat of the phonon gas. Comparing Equations (1.22) and (1.25) the kinetic theory defines the thermal conductivity as:

$$\kappa = \frac{1}{3}Cv\ell \tag{1.26}$$

This simplified analysis is valid for any type of energy carrier requiring only a single assumption of local thermal equilibrium such that the energy density can be defined as a function of the local temperature. For any solid, the contribution to thermal conductivity can subsequently be seen to consist of both electrons and phonons carrying heat. For metals, the specific heat due to electrons (around room temperature) is small and so is the mean free path due to strong scattering from phonons. However, large number density free electrons contributing to conduction travel at the Fermi Velocity ($\sim 10^6$ m/s) and hence the major contribution to thermal conductivity in metals comes from electrons that have a relatively small effective mass. This is in stark contrast to the overall specific heat of the metal, where the main contribution is due to the lattice. In insulators, however, there are no free electrons. The lattice vibrations travel at speeds around 10^3 m/s, but they scatter less with mean free paths being longer. Hence, the main contribution to thermal conductivity in insulators is phonons.

1.2.6 Boltzmann Transport Theory and the Particle Picture

Although kinetic theory provides an intuitive understanding of what goes on behind energy transfer, it fails under conditions of local temperature non-equilibrium. One instance is when the system size becomes comparable to the mean free path, ℓ. A more fundamental, but also complicated theory called Boltzmann Transport Equation (BTE) addresses this problem. It looks at a statistical ensemble of energy carriers and evolution of this ensemble with time away from equilibrium under conditions of diffusion and drift (in the presence of an external field).

In the general form, BTE can be written as [9]:

$$\frac{\partial f}{\partial t} + \vec{v} \cdot \nabla f + \vec{F} \cdot \frac{\partial f}{\partial \vec{p}} = \left(\frac{\partial f}{\partial t} \right)_{scattering} \tag{1.27}$$

where $f(\vec{r}, \vec{p}, t)$ is the statistical distribution function of an ensemble of carriers that varies with time t, position $\vec{r}$ and momentum $\vec{p}$. $\vec{F}$ is the force applied to the carriers. The terms on the left are *drift* terms and the right is the *scattering* term, which defines the rate of deviation of the ensemble away from the equilibrium distribution. In attempting to solve the equation in its most rigorous form, seven variables have to be considered, three

15

in position-space, three in momentum-space and time. Various techniques have been employed successfully to simplify the problem and transport coefficients can be extracted for different forms of fields: thermal and electrical conductivities, diffusion coefficients, Seebeck coefficient etc. While the left hand side of the equation is relatively straightforward to understand, consisting of forcing terms, the right hand side in its complete form is nonlinear having to consider scattering of a carrier from $(\vec{r}, \vec{p})$ to $(\vec{r}', \vec{p}')$. In order to linearize the BTE, the relaxation-time approximation is often invoked. Here, one *has to assume* that the energy carriers are *particles*.

$$\left(\frac{\partial f}{\partial t}\right)_{scattering} = \frac{f_0 - f}{\tau(\vec{r}, \vec{p})} \tag{1.28}$$

The linearized BTE implies that once the system of particles is taken out of it's equilibrium statistical ensemble, f_0 such that $f - f_0$ is non-zero, then collisions will bring it back to equilibrium with an exponential relaxation time, τ such that $f - f_0 \approx \exp(-t/\tau)$. Of course, the equilibrium distribution could be of any type, Maxwell-Boltzmann for gas molecules, Fermi-Dirac for electrons and Bose-Einstein for phonons and photons.

Let us reconstruct the energy flux from the perspective of particle scattering (similar to the kinetic theory developed above) but with the BTE construct now to guide us. The energy flux, similar to Equation (1.24) can be written as:

$$\vec{q}(\vec{r}, t) = \sum_{\vec{p}} \vec{v}(\vec{r}, t) f(\vec{r}, \vec{p}, t) \varepsilon(\vec{p}) \tag{1.29}$$

where $\vec{q}(\vec{r}, t)$ is the energy flux, $\vec{v}(\vec{r}, t)$ is the velocity and $\varepsilon(\vec{p})$ is the particle energy. By converting the summation into an integral and introducing the density of states, $D(\varepsilon)$:

$$\vec{q}(\vec{r}, t) = \int \vec{v}(\vec{r}, t) f(\vec{r}, \varepsilon, t) \varepsilon D(\varepsilon) d\varepsilon \tag{1.30}$$

When the length of the system is larger than the average mean free path, ℓ then the gradient term is approximated $\nabla f \approx \nabla f_0$ then the linearized BTE can be solved in 1D as:

$$f = f_0 - \tau v_x \frac{\partial f_0}{\partial x} \tag{1.31}$$

This is similar to the kinetic theory in that quasi-equilibrium is assumed (in the linear regime, the ensemble doesn't deviate much from equilibrium). Only the scattering term is hence non-equilibrium. Then, Equation (1.30) can be written as:

$$q_x(x) = -\frac{\partial T}{\partial x} \int v_x^2(\varepsilon) \tau(\varepsilon) \frac{\partial f_0}{\partial T} \varepsilon D(\varepsilon) d\varepsilon \qquad (1.32)$$

Thus, the more general form of the thermal conductivity (compare with Equation (1.26)) is:

$$\kappa = \frac{1}{3} \int v^2(\varepsilon) \tau(\varepsilon) \frac{\partial f_0}{\partial T} \varepsilon D(\varepsilon) d\varepsilon \qquad (1.33)$$

Note here that we have utilized the general relation $v_x^2 = 1/3 v^2$.

In summary, the thermal conductivity depends on the ***energy-dependent*** group velocity $v(\varepsilon)$, scattering time $\tau(\varepsilon)$ and density of states from the ω-k dispersion relation $D(\varepsilon)$. In the kinetic theory, a group velocity that is equal for all phonons is used in the estimation of the mean free path. In reality, the large wavevector (short wavelength) phonons travel slower than the small wavevector (large wavelength) phonons. An energy integral as done in Equation (1.33) prevents this overestimation leading to a more accurate determination of the average mean free path. The linearized BTE thus provides a more holistic breakdown of thermal conductivity, however it suffers from the limitation that phonons behave only as particles in the relaxation time approximation.

Since many forms of phonon scattering are present in a solid, the net relaxation time is determined by considering all the scattering methods in parallel. This formulation is called Matthiessen's Rule such that the effective scattering time, τ_{eff} is given by:

$$\frac{1}{\tau_{eff}} = \frac{1}{\tau_{phonon-phonon}} + \frac{1}{\tau_{impurities}} + \frac{1}{\tau_{boundary}} \qquad (1.34)$$

Each of these terms adds an extra length-scale (scattering time) to the limit and we can imagine that the strongest scattering will limit the mean free path the most, hence the parallel treatment of different scattering forms. Note here that we are not considering all possible phonon collisions (eg. electrons, dislocations etc) and only the ones most relevant for our study. It is also important to note that scattering is strongly temperature and energy-dependent. Let us try to understand where each of these terms comes from below.

Phonon-Phonon Scattering: As described earlier, in the particle picture, when phonons scatter with each other, they can alter both the momentum and/or the energy of the impinging phonons. For simplicity, only 3-phonon processes are considered here. While phonons are massless particles, they carry crystal momentum, which is defined as $\hbar k$ for a phonon with wavevector k.
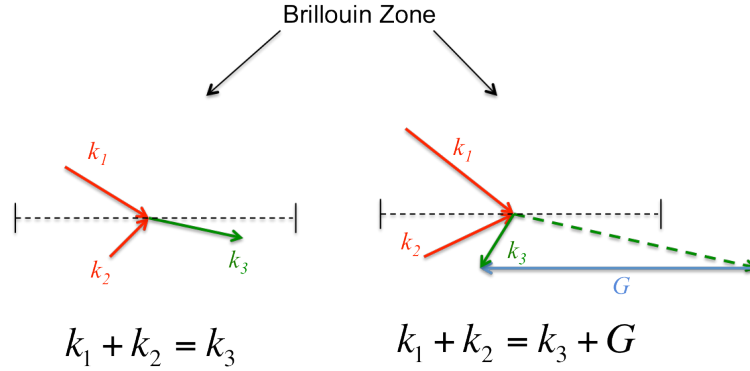
Figure 1.9 Vector Representations of Normal (N) and Umklapp (U) Phonon-Phonon Scattering

During any collision between two phonons, overall energy and crystal momentum have to be conserved. An equilibrium distribution of phonons moving under a temperature gradient in a crystal will not be affected by scattering from other phonons of the type described in the first part of Figure 1.9 above. Such collisions are called Normal (N) processes and do not provide a resistance to heat transfer. However, the second kind, where overall crystal momentum is only conserved when the momentum of the resultant phonon is reversed (dressed by the reciprocal vector, G to keep the phonon count in the Brillouin Zone intact) does cause resistance to heat flow. Such processes are called Umklapp (U) processes. Thus, phonons with small wavelengths (large wavevector) tend to scatter with other phonons following the U-processes and hence cause a resistance to heat flow that is proportional to ω^2 [10], [11] derived from Fermi's Golden Rule given by:

$$\frac{1}{\tau_{ph-ph}} \approx \frac{1}{\tau_{U,k\lambda}} = \gamma_{k\lambda}^2 \frac{2k_B T}{M v_{k\lambda}^2} \frac{\omega_{k\lambda}^2}{\omega_D} \tag{1.35}$$

where $\gamma_{k\lambda}$ is the mode Grüneisen anharmonicity parameter, $v_{k\lambda}$ is the mode group velocity and ω_D is the Debye Frequency, all defined for the mode $k\lambda$. Umklapp resistance is related to the anharmonicity of the crystal and is dominant at higher temperature, where the phonon wavelengths are longer. The distribution of phonon wavelengths as a function of temperature will be discussed more in detail in the next section. In summary, umklapp scattering is an inelastic process and is the dominant scattering mode at higher temperatures.

Phonon-Impurity Scattering: Any imperfections in the crystal can scatter phonons, although the scattering cross-section depends upon many factors, including the wavelength of the impinging phonons and the strength of the impurity scattering field. From the phonon perspective, a defect can be understood as a change in mass, the spring constant, or the local strain field. Klemens [12] came up with a comprehensive picture of how lattice vibrations can scatter from defects by using second order perturbation theory

18

and considering scattering of an incoming phonon with wavevector, k to an outgoing phonon with wavevector, k'. The Klemens' expression for the impurity scattering time in a three-dimensional crystal is given by:

$$\frac{1}{\tau_{impurities}} = 3\frac{a^3}{G}S^2\frac{\omega^4}{\pi v_g}$$

(1.36)

where a is the lattice constant of the crystal, G is the number of atoms in the crystal and $v_g = d\omega/dk$ is the group velocity that can be frequency dependent and derived from the dispersion relation. S is the scattering cross-section, which he elucidated as:

$$S^2 = S_1^2 + (S_2 + S_3)^2$$

$$S_1 = \frac{\Delta M}{M}\frac{1}{2\sqrt{3}}; S_2 = \frac{\delta(v^2)}{v^2}\frac{1}{\sqrt{6}}; S_3 = Q\gamma\frac{\Delta R}{R}\sqrt{\frac{2}{3}}$$

(1.37)

Here, S_1 arises from the mass difference due to an impurity/vacancy, S_2 arises from the difference in the local potential energy due to a binding force or spring constant change, and S_3 arises from local strain fields. For example, if there was a vacant spot instead of an atom, we can expect $\Delta M/M = -1$, $\delta(v^2)/v^2 = -1$, $and\ Q = 3.2$. Note that in this treatment, the lattice vibrations are not treated as particles and the wavelength matters. In the long wavelength limit (or at lower temperatures), we can use the Debye Approximation where $\omega=v_s\lambda$. Substituting this into Equation (1.36), $\tau_I \propto \lambda^{-4}$, which is commonly known as the Rayleigh Limit [13]. Here, the scattering from impurities is again wavelength dependent, and is elastic, since the energy is conserved. In the small wavelength limit, the cross section is proportional to the projected area of the defect and is different from Equation (1.36); for example, for a spherical defect, this is just πR^2. Another important observation is that the scattering cross-section is not directly temperature dependent.

Phonon-Boundary Scattering: Casimir [14] treated scattering from the boundary such that a perfectly rough surface absorbed all phonons incident upon it, and re-emitted them at a rate depending on the absolute temperature of the surface, just like a black body. This resulted in a well-studied (both theoretically and experimentally) diffusive picture for surface scattering as illustrated in Figure 1.10(b) [13], [15]. The other extreme of a perfectly smooth surface specularly reflecting the phonons has never been observed experimentally (see Figure 1.10(a))
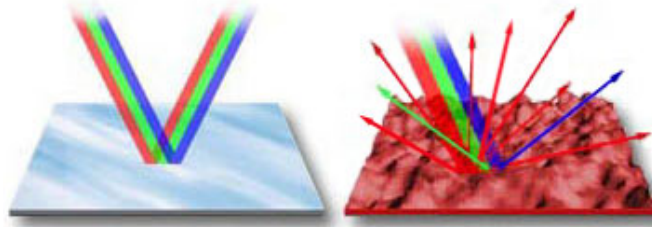
Figure 1.10 (a) Specular Reflection where the incoming wave is reflected off the surface (b) Diffusive scattering where the reflected wave loses it's memory and can scatter in any direction

Ziman [9] estimated the average mean free path from the boundary to be given by:

$$\Lambda_B = \frac{1+p}{1-p} \Lambda_{0B} \qquad (1.38)$$

where p defines the specularity ranging from perfectly diffusive ($p=0$) to perfectly specular ($p=1$) and Λ_{0B} is the mean free path for perfectly rough surfaces. Thus, the scattering time limited by boundary scattering can then be defined as:

$$\frac{1}{\tau_{boundary}} = \frac{v_g}{\Lambda_B} \qquad (1.39)$$

In the case when $p=0$, this is known as the Casimir Limit [14]. However, how rough the surface is compared to the phonon wavelength is what really determines if the scattering if diffusive or not. While super-diffusive (tending towards specular) transport has been demonstrated experimentally [16–20], it is challenging to observe anything below the diffusive Casimir Limit. Nanostructuring provides a unique opportunity to tailor boundary scattering in different ways, but this will be discussed in much more detail in Chapters 3 and 4 in this thesis.

As can be seen from studying three different phonon scattering regimes, they are significant in different temperature regimes. At very low temperatures, all the phonons are not populated and hence scattering times are low, hence dominated by first the boundary and then impurities. As temperature goes up and all phonons get occupied Umklapp scattering increases, thus increasing thermal resistance due to inter-phonon coupling. The effective scattering time coupled with the group velocity of the phonons as described in Equation (1.34) determines one important length scale of the problem – the **frequency dependent mean free path**. Extensive experimental [21–23] and theoretical [21], [24] studies have been performed in the last few years that show the accumulated contribution of frequency dependent mean free paths to the thermal conductivity, which are not reviewed here. When phonons are assumed to behave as particles, they scatter off lattice defects, the boundary and other phonons to produce a finite thermal resistance that is then used to define the thermal conductivity of the crystal. However, we should

remember that phonons are actually lattice vibrations with finite wavevectors spanning the Brillouin Zone. This brings us to the second important length-scale in the problem – the phonon wavelength.

1.2.7 Bose-Einstein Distribution and the Dominant Phonon Wavelength

As described in Section 1.2.4, phonon occupation follows Bose-Einstein Statistics, which can be rigorously derived using quantum statistical mechanical laws. In the high temperature limit, the Bose-Einstein statistical distribution is well approximated by the Maxwell-Boltzmann Distribution for particles, in which case, as pointed out in Equation (1.17), $\langle n \rangle \approx k_B T / \hbar \omega$. Then, the average energy occupied by phonons at a particular temperature is given by $\langle E \rangle \approx \langle n \rangle \hbar \omega = k_B T$. Utilizing the Debye Approximation $\omega = 2\pi v_s / \lambda$, the dominant wavelength carrying the energy of phonons can then be defined as:

$$\lambda_d \cong \frac{2\pi \hbar v_s}{k_B T}$$

(1.40)

This is an order of magnitude estimate at best, since there are a number of approximations involved in deriving this formulation. For Silicon at 300K using the longitudinal speed of sound at room temperature as an approximation for v_g=8433 m/s, and substituting $\hbar = 1.034 \times 10^{-34} Js$ for the reduced Planck's constant and $k_B = 1.38 \times 10^{-23} JK^{-1}$, $\lambda_d \sim 8\text{Å}$. Obviously, the dominant wavelength can not be less than the lattice spacing of the crystal, but typically the order of magnitude estimate can be used to guess that the dominant wavelength, $\lambda_d \sim 1$ nm [25]. In order to define the dominant wavelength accurately, one can use the Wien's Displacement Law for inspiration. In the case of blackbody emission from a body, the maximum value of the Planck's Distribution can be determined by considering the spectral distribution of the intensity, $I(\lambda)$ and then finding the wavelength where $dI(\lambda)/d\lambda = 0$ [25]. In the case of phonons a similar analysis can be attempted; however one has to be careful, as the weightage has to be determined for how much heat is carried by which phonons, which differs from occupation of heat [26].

Dames and Chen [26] were able to derive the wavelength distribution of phonons contributing to thermal conductivity by considering a crystal in the diffusive boundary scattering regime *(p=0)*. This was a clever trick employed so that the phonon mean free path, ℓ would now be a function of the phonon wavelength. Then, the spectral thermal conductivity can be written as a function of wavelength similar to Equation (1.33):

$$\kappa(\lambda) = \int_0^\lambda d\lambda \, C_v(\lambda) \cdot v(\lambda) \cdot \ell \tag{1.41}$$

Here, the analysis is considerably stronger than the order of magnitude estimation above, since a more accurate analytical model can be used for the dispersion relation that defines the phonon group velocity. The Debye Model overestimates the group velocity for the higher energy, small wavelength phonons. Using the Born-von Karman model to define the phonon energies, $\omega = \omega_0 \sin(\lambda_0 k / 4)$, the spectral group velocity, $v(\lambda)$ can be more accurately estimated. Here, $\omega_0 \equiv 4 v_g / \lambda_0$ with λ_0 is obtained by considering all the phonons in the Brillouin Zone as $\lambda_0 = 2\pi \big/ \left(6\pi^2 N\right)^{1/3}$ for a three dimensional crystal. For silicon, they derive λ_0 as $0.55 nm$. Then, the accumulative spectral thermal conductivity can be subsequently estimated as:

$$\frac{\kappa(\lambda)}{\kappa_{total}} = \frac{\displaystyle\int_0^\lambda C_v(\lambda) \cdot v(\lambda) d\lambda}{\displaystyle\int_0^{\lambda_0} C_v(\lambda) \cdot v(\lambda) d\lambda} \tag{1.42}$$

This analysis is tremendously enlightening for nanostructures and for silicon at high enough temperatures, the analysis shows that 90% of the heat is carried by phonons that have $\lambda < \left(2.94\lambda_0 \approx 1.61 nm\right)$ [26]. At lower temperatures, the spectrum of wavelengths contributing to thermal transport broadens, with 90% of heat being carried by phonons with wavelengths less than $11.3 nm$ in Silicon at 10K. Esfarjani et. al took this analysis further for bulk Silicon where the mean free paths can be spectrally dependent and used first-principles calculations to show that phonons with wavelengths less than $6 nm$ carry all the heat in Silicon at 277K as shown in Figure (1.11) below [11].
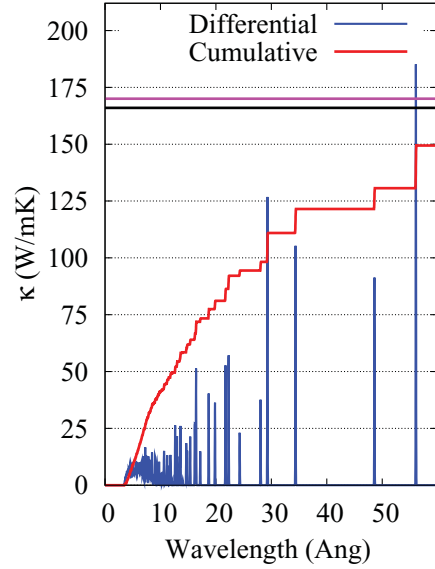
Figure 1.11 Reproduced from Esfargani et. al., the accumulation of thermal conductivity in Silicon at 277K as a function of phonon wavelength is shown by the red curve [11].

In the strictest sense, if one is able to design nanostructures that have dimensions of the order of the 'thermal wavelength', then phonon wave effects can dominate particle based transport and many interesting wave phenomena could be observed. One such experiment that stood out was the measurement of the quantum of thermal conductance by Schwab et. al. using 60nm thick and 200nm wide Silicon Nitride membranes. These dimensions were close to the dominant phonon wavelength, λ_d below 0.8K, where these measurements were performed [27].

Thus, the phonon wavelength is the second important length-scale that needs to be considered while studying heat transport. Apart from the thermal de Broglie Wavelength at any temperature (as discussed in the previous paragraph), scattering of phonons with different wavelengths can also be non-diffusive. In Ziman's treatment of boundary scattering, he determined an expression for the spectral specularity parameter [9]:

$$p(\lambda) = \exp\left(\frac{-16\pi^2\eta^2}{\lambda^2}\right) \tag{1.43}$$

(note extra factor of π has been removed as pointed out by Zhang [28] and Yang et. al. [29]) where η is the root mean square amplitude of the roughness of the boundary. Thus, the same surface can appear rough for smaller wavelength phonons, but smooth for long wavelength phonons. However, this definition of the specularity parameter needs to be addressed carefully as it assumes that the surface roughness, given by $f(x)$ is approximated by an auto-correlation function that is Gaussian. In detail, the auto-correlation for the roughness can be defined as:

$$\rho_f(\xi) = \int_{-\infty}^{\infty} f(x) f(x+\xi) d\xi \qquad (1.44)$$

In Ziman's derivation of Equation (1.40), the auto-correlation is assumed to take the form:

$$\rho_f(\xi) = \exp\left(-\xi^2 \big/ L^2\right) \qquad (1.45)$$

where L is the correlation length that is a measure of the width of the bumps on the surface. In order for the simplified Equation (1.43) to be valid, the roughness has to obey the relation $L << 4\pi\eta$. This would mean that the boundary of the system must have sufficient areas of steeply sloping facets and is one major assumption of the analysis. Further, the analysis treats incoming and scattered waves as if normal to the surface. Hence, if the angles of incidence were changed, the specularity parameter would be larger. Chapter 3 looks at boundary scattering from a rough surface in more detail, both from the theoretical and experimental perspective.

1.2.8 Phonon Coherence Length

The third important length-scale that is less talked about in the phonon physics community is the coherence length of phonons. Let us consider any plane wave with a frequency ω. Now consider the superposition of this wave with other planes waves near in frequency, with a bandwidth $\Delta\omega$. Depending on the number of plane waves interacting with each other, the resultant waves start having a beating frequency and eventually collapse into a wavepacket. The coherence length defined for a wavepacket is typically considered to be the spread of the wavepacket itself, which is true when the superposition consists of waves that are coherent with each other to begin with as shown in Figure (1.12a). In the case of phonons, within the energy bandwidth defined by the thermal energy $\sim k_B T$, the phonons are uncorrelated. Hence, a superposition of these can lead to less-localized wavepackets as is illustrated by Figure (1.12b). If we choose to be completely rigorous, the phonon thermal wavelength defined as $\lambda_T \approx 2\pi v_s \hbar / k_B T$ is the best indicator for the width of a phonon wavepacket, assuming it is non-dispersive. At room temperature, for most solids, considering $v_g \sim 5000\ m/s$, $\lambda_T \sim 1nm$.
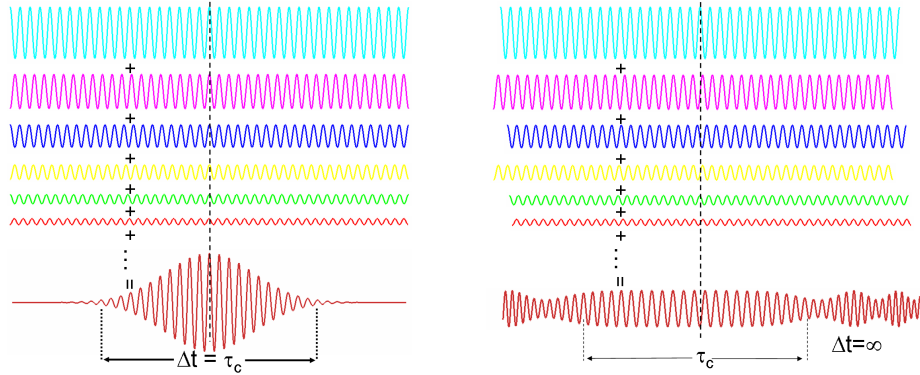
Figure 1.12 (a) When the source waves are coherent and there exists a fixed phase relationship between them, the superposition is a wavepacket with a finite coherence length (b) When the source waves are incoherent, the superposition is a wavepacket with a larger coherence length. [Wikimedia commons]

In order to observe any wave effects in phonons, the scattering has to be elastic and preserve phase. Phonon-Phonon scattering as described above is inelastic in nature, since the resultant phonon after scattering can have no phase-relationship to the incoming phonons. In general, any anharmonicity in the crystal would break the phase of two interacting phonons and hence not allow the scattering to preserve coherence. Therefore, for bulk silicon at room temperature, or any temperature higher than ~ 20K, where scattering is dominated by umklapp resistance, the coherence length of phonons is actually equal to the particle-based mean free path, larger than the phonon wavelength. However, at low temperatures where either boundary or impurity scattering dominates, the coherence is preserved and hence the coherence length of the phonons is longer than the scattering mean free path. In the case of nanostructures, the boundary scattering regime can dominate up to much higher temperatures. Hence, the scenario wherein the phonons can scatter as waves from boundaries or impurities are interesting and can lead to coherent effects such as phonon localization.

1.3 EXPERIMENTS PROBING PHONON LENGTH SCALES

Phonons can therefore behave as particles, while in reality they are lattice vibrational waves with a wavelength spectrum as well as coherence length. For bulk solids at room temperature, typically the particle mean free path, $\ell \sim O(10^2 \, nm)$; here $O(x)$ stands for order of x. The dominant wavelength, $\lambda_T \sim O(1 \, nm)$ and the strictest coherence length, ℓ_c $\sim O(1 \, nm)$ defined as the expanse of a phonon wavepacket with a thermal broadening of $\sim k_B T$ around λ_T. In the case of phonons behaving as dispersive wavepackets, it is possible that $\ell_c > \lambda_T$. When the dominant scattering mode of phonons is umklapp, $\ell_c = \ell$. However, when the dominant scattering of phonons is due to impurities or the system boundary, $\ell_c > \ell$ allowing for the possibility of wave behavior of phonons being observed in thermal transport. Typically, in bulk crystals, this condition is satisfied in very low temperatures. In nanostructures, the boundary scattering regime is extended to higher temperatures, thus opening up the possibility of observing wave effects such as localization.

The huge body of literature with the thermal conductivity of bulk solids is impossible to review in this short treatise. It suffices to say that the major physics as described in the earlier sections has been observed experimentally from measurements of specific heat, the phonon dispersions as well as the thermal conductivity under a variety of conditions. A few key experiments that present the importance of the length scales listed above will be discussed here as a precedent to the experiments attempted in this work.

Holland's review in 1964 [30] provides a comprehensive overview of boundary, impurity and umklapp scattering times for bulk samples of Silicon, Germanium, Gallium Arsenide, Gallium Antimonide, Cadmium Telluride, and Cadmium Sulfide in the wide temperature range from 1.7 to 300K. Silicon is a material of choice for many experimental studies due to a variety of reasons. It is easy to manufacture and has wide applications in the electronics industry. From a physical perspective, it has very harmonic bonds and is easy to manipulate by introducing doping impurities and/or etching to define the system size. Thermal conductivity of bulk crystalline-silicon as a function of temperature is given below in Figure 1.13.
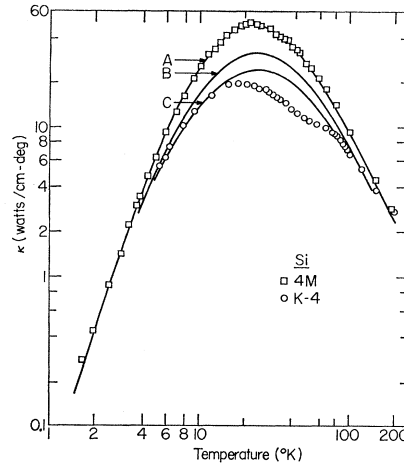
Figure 1.13 Thermal Conductivity of Bulk Silicon as a function of temperature. The variation in data in the intermediate temperature regime is mainly due to different impurity concentrations, while the umklapp (high temperature) and boundary (low temperature) dominated regions match up well. Figure from [30].

Klitsner and Pohl [31] performed a series of careful thermal conductivity measurements to gauge the effect of surface roughness and films (either deposited metal or grown silicon oxide) on the surface of a clean Silicon crystal in 1987. All of these measurements were performed in the temperature range from 0.1-10K, where the dominant phonon wavelength ranged from 6.5-650 nm. They found that for rough surfaces, as well as thick films on top of Silicon, the surface scattering was diffusive in nature and reduced the thermal conductivity substantially as is seen in Figure 1.14 below.
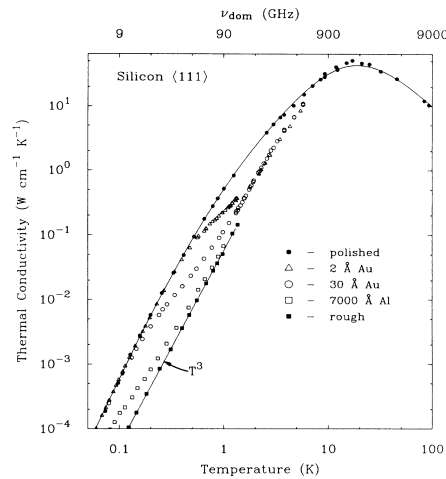
Figure 1.14 Thermal conductivity of bulk Silicon for two extreme cases from polished, clean surface to a sandblasted rough surface. The intermediate curves are for different thicknesses of gold films deposited insitu on a clean Silicon surface. Figure from [31].

While the surface roughness was not characterized, one can imagine that as long as the sand blasted roughness did not have a rms height, $\delta < 6.5nm$, Ziman's specularity rule given in Equation (1.43) would result in diffuse surface scattering with $p\sim0$. The thin films of gold played the role of scrambling the phonons diffusively due to a large acoustic mismatch as well as surface disorder generated during film creation. Thus, they noticed that while surface morphology can affect thermal transport, scattering was diffusive and closely matched what was predicted by Casimir's theory like in Equation (1.39).

In the 1990s, thin film Silicon-On-Insulator technology allowed preparation of two-dimensional films of high quality silicon and Ju et. al and Asheghi et. al. measured the thermal properties in 1997-99 [32], [33]. They beautifully illustrated how the mean free path of phonons in Silicon at room temperature is around 300 nm, an order of magnitude larger than what is predicted by kinetic theory of gases. This was the first foray of the thermal community into nanostructures that were close to the important length-scales defining transport. The films were designed to be of a thickness close to the mean free path, ℓ and the authors observed a 50% reduction in thermal conductivity due to boundary scattering. Further, Fuchs-Sondheimer theory was used to correctly predict the reduction in the diffusive mean free path [34] that scaled with the thin film thickness.

In 2003, Li et. al. [35] studied thermal transport in quasi one-dimensional Silicon Nanowires. The scattering mean free path was found to scale with the diameter, and followed the Casimir Limit as seen in Figure 1.15 below, except for the smallest 22nm diameter nanowire. They achieved an order of magnitude reduction in thermal conductivity at room temperature.
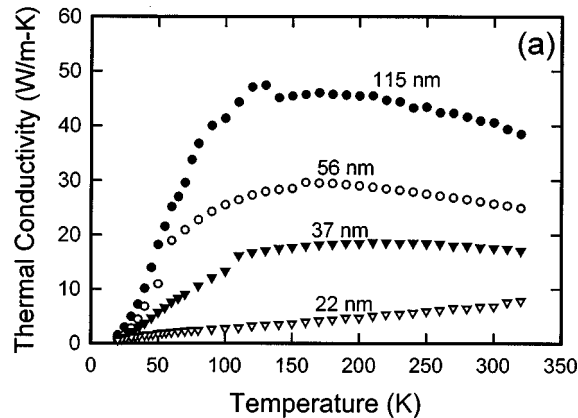
Figure 1.15 Thermal Conductivity of Smooth Silicon Nanowires exhibiting diffusive boundary scattering following the Casimir theory. Figure from [35].

A more interesting discovery was made in 2008 when Hochbaum et. al. found that nanowires with rough surfaces had an additional reduction in thermal conductivity by a factor of 5-10 for the same diameter wires [36]. In particular, the 56 nm diameter nanowire showed a thermal conductivity of 1.6 W/m-K at 300K, which is ~100 times smaller than the thermal conductivity of bulk Silicon at the same temperature.
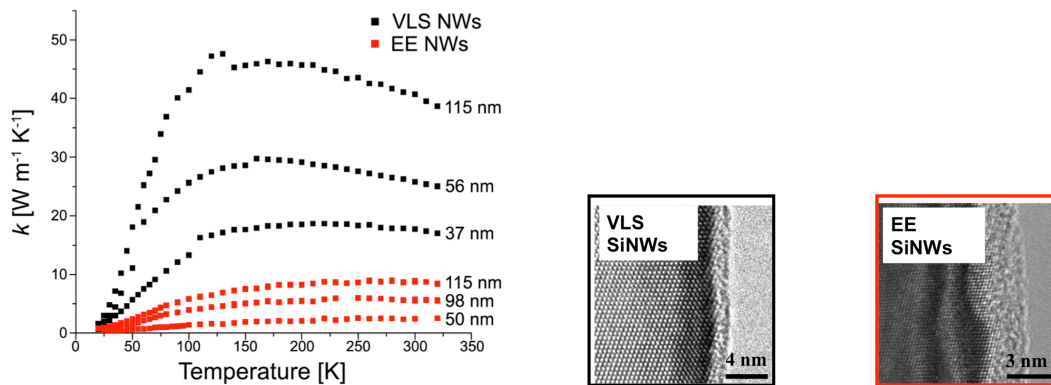
Figure 1.16 (a) Comparison of thermal conductivity of rough EE Silicon Nanowires [36] and smooth VLS Silicon Nanowires [35] (b) TEM picture of smooth VLS NWs (c) TEM picture of rough EE NWs

The roughness of the nanowires was not characterized and no systematic study was done on the morphology of the nanowires to understand the origin of this reduction below the Casimir Limit. One possibility that allows this reduction in thermal conductivity is when phonons behave as waves instead of particles, thus deviating from the well-accepted Casimir theory. If true, the surface allows for coherent scattering of the phonon waves, thus localizing the phonons and impeding their transport. In this thesis an attempt has been made to characterize carefully nanowires with rough surfaces and understand the effect this has on measured thermal conductivity and will be dealt with in detail in Chapter 3.

An interesting phenomenon that was pioneered by Humphrey Maris [37–39] was the effect of crystal direction on the thermal conductivity. They measured Silicon and Calcium Flouride in the temperature range 3-40K and found that in the boundary scattering regime, crystal orientation could account for upto 50% difference in the measured thermal conductivity. What resulted was a seminal understanding that in anisotropic crystals, the phonon phase and group velocities were not the same and resulted in an effect called phonon focusing due to elastic anisotropy. In this case, the energy flow was directed along certain crystallographic directions, which were experimentally matched up with the rod axes. The authors also provided a correction to the Casimir Limit as a function of the rod geometry in the diffusive regime. Interestingly, they also observed a deviation towards specular scattering from the surface at lower temperatures. Inspired from these studies, in Chapter 4 we explore the directional dependence of thermal conductivity in nanowires of semi-metallic Bismuth.
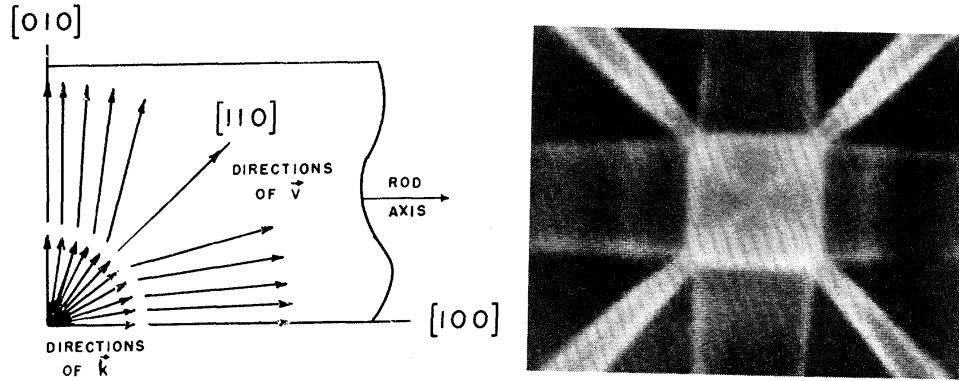
Figure 1.17 (a) Phonon focusing as illustrated by McCurdy, Taylor et. al. [39] A deviation of the group velocity directions given by $\vec{v}$ from the phonon wavevectors $\vec{k}$ allows focusing of energy flow in directions perpendicular to the rod axis compared to an isotropic solid. (b) Phonon Imaging showing different intensities of energy flux in different directions in a Germanium crystal at ~2K. Image adapted from Northrop and Wolfe [40]

These experiments mostly alluded to phonon transport in the diffusive regime. At the other end of the spectrum, many novel experiments have been devised that strive to achieve coherent generation of phonons in order to study their scattering behavior. Thermal phonons typically lie in the 1-10 THz (10^{12} Hz) frequency bandwidth in most solids. Such frequencies are difficult to access for actuators of phonons. In the subsequent section, we will briefly review methods that have been established to generate coherent non-equilibrium phonons. These phonons are non-equilibrium since they do not relax to their equilibrium state due to scattering inside the material like thermal phonons do. However, they provide a powerful tool towards understanding spectral scattering when wave nature of phonons is dominant, especially in nanostructures as is the focus of this work.

The first experiments on generation of coherent phonons were done in the microwave frequency range [41] by using piezoelectric thin film transducers. The conversion of electric pulses to mechanical vibrations mainly functioned in the GHz (10^9 Hz) frequency range, with wavelengths typically in the sub-micrometers. Such ultrasonic tools were mainly used in the 1960s to probe how matter and light scattered differently in materials. Maintaining coherent transport of these piezoelectric driven waves was very difficult however, since their interaction with thermal phonons of much shorter wavelengths randomized their phase.

Van Gutfeld and Nethercot in 1964 [42] pioneered the use of thin metal films as a source of incoherent phonons based on their temperature. They deposited a thin film of metal on the material and activated it electrically or optically. The heating of the film (Au or Cu) resulted in the emission of a broadband radiation based on Planck's blackbody frequency spectrum. The experiments were performed at ~10K, which based on Wien's Displacement law gave peak values of frequency at ~0.6 THz. Such metals are very efficient sources of high frequency phonons, which are however not monochromatic. The phonons are detected on the other side using a thin film bolometer, which has a small

specific heat and thus heats up very rapidly. The resistance of this bolometer can be calibrated and is a strong function of its temperature. The measurements were done at very low temperatures ~1.6K [43]. Interestingly, the pulses traveled through the samples at velocities equal to the speed of sound. The reason behind the high pulse velocities is that not enough equilibrium phonons are present in the sample at low temperatures to scatter the non-equilibrium phonons, thus travel of these pulses was ballistic, while they coupled to the compression and shear waves inside the crystal. Further, these experiments allowed isolation and identification of different phonon modes inside the crystal (Transverse and Longitudinal) as a function of their differing velocities. Following the experiment on bulk Silicon rods performed by Taylor et. al. in 1969, phonon optics were extremely useful in showing phonon focusing effects. Northrop and Wolfe used an extremely thin Aluminum film bolometer as a phonon detector coupled with a *xy* raster scanned laser beam and were able to provide a two-dimensional map of phonons focusing in different crystallographic directions as shown in Figure 1.17 (b) [40].

The drawback of using thin film metal transducers was the broadband phonon wavelengths at the source. This problem was circumvented by using Superconducting Tunnel Junctions (STJs) developed in the 1970s by sandwiching an extremely thin insulating layer (~2 *nm*) in between two thin superconducting films (~100 *nm*) [44]. In brief, when a voltage is applied across the sandwich, $eV > 2\Delta$ - where 2Δ is the superconducting gap - the electrons injected across the STJ transfer their energy to phonons in the lattice. This energy bandwidth is extremely narrow, thus producing a monochromatic source of phonons that deviates strongly from the Bose-Einstein Distribution. These phonons were generally in the 10^{11} Hz regime. These systems opened up a whole range of possibilities to study phonon optics, ranging from the design of phonon filters [45], second sound in Bismuth and NaF [46], as well as studies on resonant phonon absorption [47] to name a few.

One of the more interesting works that has inspired study of coherent thermal transport and is a subject of intense scrutiny in the thermal transport community was the prediction and observation of phononic mini-bands in AlAs-AlGaAs MBE-grown superlattices [45]. The artificial periodicity of ~12 *nm* is less than the phonon mean free path, ℓ and comparable to the dominant phonon wavelength, λ_D. This causes a change in the acoustic phonon-dispersion relations. In the cross-plane direction in real space, the unit cell is now larger and hence the reciprocal space Brillouin Zone is smaller thus causing zone folding and hence a decrease in the group velocity of acoustic phonons due to flattening of the high-frequency phonon modes. Hence, when the phonon wavelengths are close to the superlattice spacing, given by $\lambda_0 = 2d$, the phonons behave as Bragg reflectors. Thus, the superlattice structure was shown to behave as a phonon cavity, establishing the methodology for future studies of phonon-based optics.
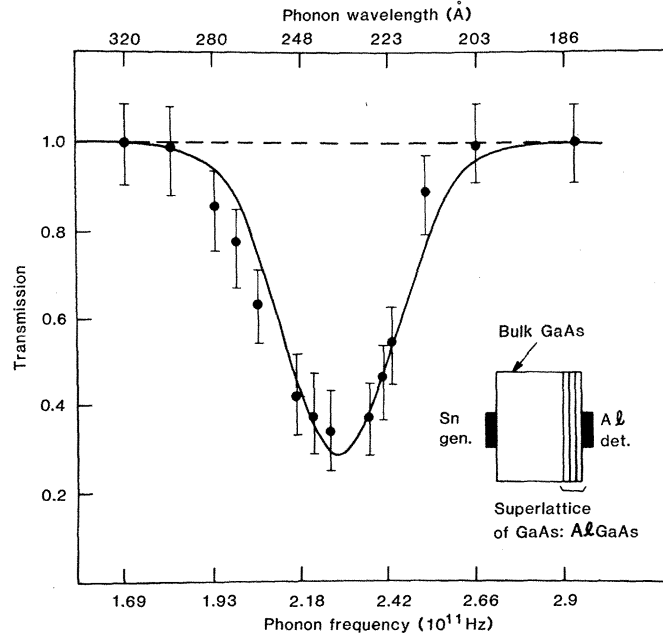
Figure 1.18 For frequencies of the STJ phonons corresponding to $\lambda = 2d$, the transmission drops by ~80%. The device structure is shown in the inset. Figure adapted from [45]

In the recent two decades, much progress has been made in utilizing this understanding of phonon length-scales learnt from coherent generation and control of phonons and applying them directly to heat transport measurements of nanostructures. For example, the measurement of the cross-plane thermal conductivity of Bi_2Te_3/Sb_2Te_3 superlattices by Venkatasubramanian [48] showed a minimum in thermal conductivity at superlattice spacing d~6.5-7.5 *nm* at 300K, which can be compared to the decrease in transmission as observed in Figure 1.18. The mechanism and repeatability of this measurement is debatable, especially since chalcogenides have been known to have a mean free path of the order of ~1 *nm*. The theory proposed indicates coherent correlated scattering from the interfaces and indicates wave-like behavior of acoustic phonons, either due to phonon localization or due to the formation of phononic mini-bands.

A controlled study of spectrally dependent scattering was performed by Kim et. al. [49] where ErAs nanoparticles embedded in InGaAs alloy showed a decrease of thermal conductivity below the alloy limit. The mechanism that explained this behavior was that the short wavelength phonons in the alloy are scattered effectively by impurities and defects, whereas the long wavelength phonons are transparent to these. This stems from the Rayleigh approximation as discussed in Equation (1.38) where the scattering cross-section is given by: $\sigma \sim b^6/\lambda^4$ where b is the typical size of the scattering center, ~1Å for particles. Since the small wavelength phonons are scattered well in alloys, the major contribution to thermal conductivity comes from mid- and long-wavelength phonons. These longer wavelength phonons were effectively scattered by embedded nanoparticles with a few nanometers in diameter and reduced the thermal conductivity even below the alloy limit.

In summary, early studies on thermal conductivity typically proved that the Casimir Limit of diffusive scattering was mostly valid for boundary scattering from bulk samples at high temperatures. At very low temperatures, some signatures of specular wave-like scattering were observed. Phonon optics provided a valuable tool to study different properties of how phonons traveled as waves in solids at very low temperatures. The advent of nanotechnology allowed design and creation of novel structures with characteristic lengths of the order of the mean free path of phonon scattering. However, the ultimate limit of nanostructure sizes close to dominant phonon wavelengths has seldom been reached. The next wave of discovery in phonon physics surely lies in pushing the limits of transport beyond the particle picture and observing and manipulating phonons as waves. This could come from spectral coherent scattering from the surface, an approach that is explored in Chapter 3 of this thesis. Further, studying crystal direction-dependent heat transport in nanostructures pushes the envelope further, as shown in Chapter 4. Finally, the role of electron-phonon coupling has not been touched in this introduction, as the focus has remained on dielectric solids. In Chapter 5, we will briefly look at the basics of electron-phonon interactions and how that might lead to interesting effects and the creation of solid-state thermal devices. But first, we will look at the measurement platforms, their design and implementation in Chapter 2.

CHAPTER 2

THERMAL MEASUREMENT TECHNIQUE

In this chapter, we will look at the thermal measurement technique for single nanowires. After describing the basic principle of measurement, we will then study the limits and major sources of error in the measurement, namely contact resistance and sensitivity. Finally, we will address the contact resistance problem in a novel fashion by showing that monolithic contact between the nanostructure and the measurement system can eliminate this problem altogether.

Section 2.2.4 of this chapter first appeared in *Nano Letters, Vol. 10, No. 11, 4341-4348 (2010)* [50]. (Note, the whole paper has not been reproduced, only certain relevant sections have been included)

Title: Fabrication of Microdevices with Integrated Nanowires for Investigating Low-Dimensional Phonon Transport

Authors: Kedar Hippalgaonkar*, Baoling Huang*, Renkun Chen*, Karma Sawyer, Peter Ercius, and Arun Majumdar.
*equal contribution

2.1 THERMAL MEASUREMENT OF ONE-DIMENSIONAL STRUCTURES

The technique to measure thermal properties of nanostructures has been pioneered by Prof. Arun Majumdar's group since 2003. The design and fabrication of these novel devices was made in 2001 by Prof. Philip Kim and Prof. Li Shi, used for measuring the thermal conductivity of carbon nanotube bundles [51]. Subsequently, the measurement has been refined and improved with different measurement schemes serving different purposes. While the first few attempts were made in order to make the system adaptable to different materials [35], [52], [53], progress was also made in measuring the electrical and thermal properties of nanowires simultaneously [54].

Measuring the thermal conductivity of nanostructures is a challenging task that entails the use of microfabrication techniques to create a measurement platform that interfaces with the nanostructure. For one-dimensional nanowires, a direct technique is employed where a temperature gradient ($T_{hot} - T_{cold}$) is maintained across the nanowire and the heat flow through the nanostructure ($Q_{nanowire}$) is measured accurately. A Scanning Electron Micrograph of a measurement device is shown below:
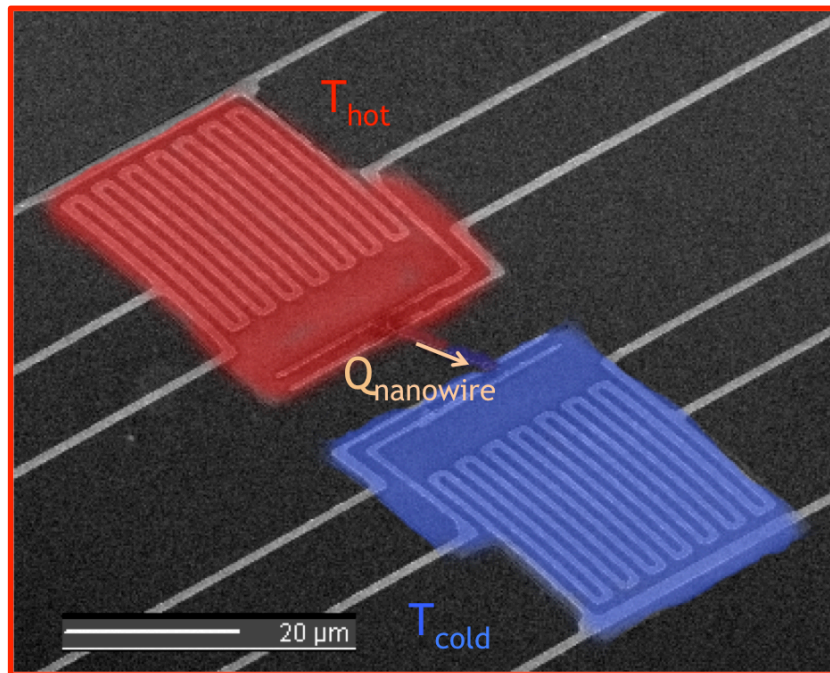
Figure 2.1 Microfabricated Thermal Measurement Platform with nanowire suspended between the membranes.

Two suspended platforms are micro-fabricated and released from the supporting substrate via chemical etching. The detailed micro-fabrication steps can be found elsewhere [50], [55]. The suspended legs act as a connection to the silicon chip and are treated as heat

leakage paths from the suspended platforms. An individual nanowire is then transferred to a silicon micro-device so as to form a bridge between the two parallel, suspended SiN_X membranes, each consisting of micro-fabricated symmetric resistive Pt coils, for thermal and electrical transport measurements (Fig. 2.1). The Pt coils are used as both heaters and resistive thermometers. A resistive heater is used to heat the whole Si chip uniformly inside a cryostat to control the global device temperature. For thermal conductance measurements, a small DC current (~6 µA) is passed through the Pt coil on one of the membranes to heat it to a temperature, T_{hot}, above T_0, thus inducing a heat flow $Q_{nanowire}$ through the nanowire to heat up the other membrane to T_{cold}. An AC current of 500 nA is passed through the Pt coils on both membranes to determine its electrical resistance through a 4-point technique, which is then used to estimate the temperatures T_{hot} and T_{cold}. Using two SRS 850 lock-in amplifiers for the AC signals, signals from the sensing side were measured using a frequency of 199 Hz whereas that for the heating side utilized 1.11 kHz. The resistance of the patterned coils, R_{hot} and R_{cold} vary between 3 and 5 kΩ at room temperature for different devices and are linearly proportional to the temperature on the pads. Following the analysis of Shi et. al. [52] the thermal conductance of the Platinum beams that suspended each platform can be described as follows:

$$G_l = P \Big/ \left(\Delta T_h + \Delta T_s \right)$$
(2.1)

Here, a known power P was supplied to the Pt coil heater on one SiN_x membrane which also takes into account heat losses through the supporting legs, while resistance changes of the heater and sensor were used to determine the resulting temperature changes of the heater ($\Delta T_{hot} = T_{hot} - T_0$) and sensor ($\Delta T_{cold} = T_{cold} - T_0$) pads. Utilizing the diffusive heat transfer equation while accounting for uniform joule heating in the SiN_x legs that suspended the platforms, it can be shown that

$$P = I_h^2 \left(R_{hot} + R_{leg} \right)$$
(2.2)

Here I_h is DC current supplied, $R_{hot} \sim 3k\Omega$ is the resistance of the Platinum coil on the heating side and $R_{leg} \sim 3k\Omega$ is the electrical resistance of one out of six SiN_x legs that help suspend each platform. Note that the power P only shows the resistance of one suspended leg carrying the heating current, while the Joule heat from the other heating leg is utilized in maintaining temperature equilibrium. A detailed fin analysis can be performed with isothermal boundary conditions at the ends of each heating leg to observe this At 300K, we can estimate that the heat loss through the SiN_x legs using Equation (2.1) is $G_l \sim 100 \, nW/K$.

As an illustration, for an actual thermal device where the heating current is 6 µA, $R_h = 3.336k\Omega$, $R_l = 3.340k\Omega$, with a nanowire placed across the heating and sensing pads, we obtain $\Delta T_h = 2.49K$ and $\Delta T_s = 0.96K$, which results in a leg conductance of $G_l \sim 69.5 \, nW/K$. Note here that using a 500 nA rms AC current on the heating and sensing

pads to measure the resistances thus only gives a temperature rise on either membrane of $\Delta T_{h,AC} = \Delta T_{s,AC} \sim 10mK$, which is below the temperature fluctuations in the cryostat and only causes an additional increase in temperature excursion of $\Delta T_{AC}/\Delta T_s \sim 10mK/1K \sim 1\%$.

Further, the heat flow through the nanowire, Q can be determined as a function of $\Delta T = T_h - T_s$, which is typically maintained within a few Kelvin. The thermal conductance G_w of the nanowire can hence be determined from ΔT_h and ΔT_s with the use of the relation

$$G_w = \frac{P}{\Delta T_h - \Delta T_s} \left(\frac{\Delta T_s}{\Delta T_h + \Delta T_s} \right) \tag{2.2}$$

The DC power input, P is known to a very high accuracy (<0.5%), while the temperature measurement uses the temperature coefficient of resistivity (TCR) of the Platinum thin film on either membrane(<2%) (see Appendix 2A for error analysis).

In the thermal measurement scheme, the conductance of the beam is determined by ramping up the temperature in a stepwise (50 steps) fashion by passing a DC current (0-8μA) through the PRT on the heating membrane. The rise in temperature on either side is monitored by measuring the resistances, R_s and R_h on both platforms, as seen in Fig 2.1 below. For a Platinum Resistance Thermometer (PRT) in the temperature range of our measurement (50K-300K), the resistance changes linearly with temperature:

$$\Delta R_s = \left(R_s - R_{s,G} \right) \propto \left(T_s - T_G \right) = \Delta T_s \tag{2.3}$$
$$\text{and}$$
$$\Delta R_h = \left(R_h - R_{h,G} \right) \propto \left(T_h - T_G \right) = \Delta T_h$$

Since the rise in temperature is proportional to the supplied power through I_h, $\Delta T_h \propto I_h^2 R_{h,G}$ and $\Delta T_s \propto I_h^2 R_{h,G}$.
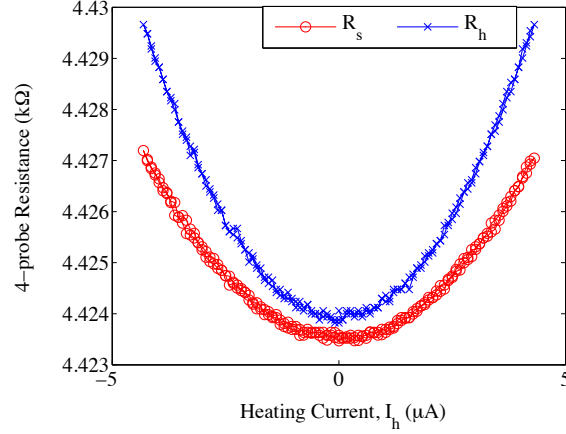
Figure 2.2 R_s and R_h as a function of the heating current, I_h. Resistance is proportional to temperature, which in turn is proportional to the power supplied by joule heating. Thus, the resistance has a quadratic dependence on I_h

Following the analysis of Equation (2.2), the heat flow in the nanowire can be estimated as: $Q = \gamma \cdot \dfrac{I_h^2 R_h}{\left(\Delta T_h + \Delta T_s\right)} \cdot \Delta T_s$, where γ is a non-dimensional ratio of the resistance of the PRT and the resistance of the suspended legs. γ is a constant at all temperatures. The nanowire conductance can hence also be written as

.

$$G_w = \frac{Q}{\Delta T_h - \Delta T_s} \tag{2.3}$$

Further, the thermal measurement technique only measures a two-probe conductance, which includes thermal contact resistance between the beams and the membrane.

2.2   IMPACT OF THERMAL CONTACT RESISTANCE

2.2.1 Thermal Contact Resistance

Since we measure the two-probe thermal conductance of the nanowire, it is impossible to eliminate the effect of thermal contact resistance. In the measurement scheme described above the heat transfer through the nanowire can be described by a thermal circuit as drawn below:
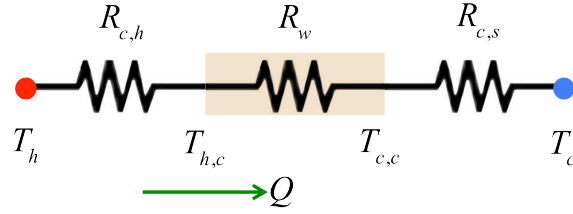
Figure 2.3 Thermal Contact Resistance Network

Here, $R_{c,h}$ and $R_{c,s}$ represent the thermal contact resistances on the heating and sensing sides respectively, while $R_w = L/k.A$ represents the thermal resistance of the nanowire suspended in between the membranes. While T_h and T_c are measured accurately using the patterend Platinum Resistance Thermometers, the intermediate temperatures given by $T_{h,c}$ and $T_{c,c}$ are unknown. Hence, in reality,

$$Q_w = \frac{T_h - T_c}{\left(R_{c,h} + R_w + R_{c,s}\right)} \tag{2.4}$$

which results in a non-ideal value for the measured resistance, $R'_w = Q_w / \left(T_h - T_c\right)$.

It is important to realize that the contribution of contact resistance between the nanowire and the suspended membrane to the total measured thermal resistance can vary depending on not only the quality of the contact, but also the temperature drop across the nanowire itself [56]. Consider the following two extreme scenarios:

(1) $R_c \gg R_w$: This can happen in two cases:

1a. If the contact between the nanowire and the membrane is not of a good quality, then the maximum temperature drop will occur at the contacts and the measured thermal conductance is only that of the contacts and not the nanowire.

1b. If the intrinsic thermal conductance of the nanowire is very high, then the temperature drop across the nanowire, $\Delta T_w = T_{c,h} - T_{c,c}$ is much smaller than the temperature drop at the contacts, $T_h - T_{c,h}$ and/or $T_{c,c} - T_c$. This scenario is material-dependent, since the thermal drop across the nanowire is defined as $R_w = L/k.A$, where L is the length of the suspended part of the nanowire between the two membranes, k is the intrinsic thermal conductivity of the nanowire to be measured and A is the cross-sectional area of the nanowire in question.

(2) $R_w \gg R_c$: This is the ideal scenario where the contact resistance is negligible and most of the temperature drop occurs between the nanowire ends and almost none at the contacts. In reality, this situation can be achieved by carefully selecting the nanowire geometry (larger lengths and smaller cross-sectional area) in addition to ensuring good contact between the nanowire and the suspended membrane. Traditionally, the contact

resistance has been alleviated by using Focused Ion/Electron Beam Induced Deposition (F(I/E)BID) of a Pt/C composite, which (a) increases the contact area between the nanowire and the suspended membrane and (b) fills in any air gaps in the dry interface at the points of contact with the organometallic Pt/C substance. It has been shown previously that the total measured thermal resistance (including the contact) can be reduced by 10-15% by depositing this composite using the F(I/E)BID [35], [36], [53], [54], as is shown below in Fig. 2.4.
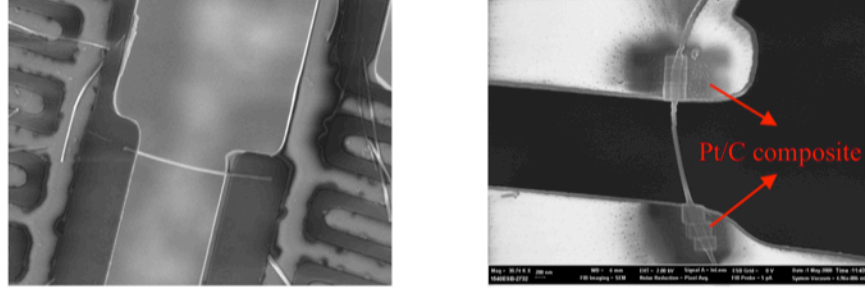
Figure 2.4 (a) Silicon Nanowire suspended between the heating and sensing membranes (b) Same Silicon Nanowire after Focused Electron Beam induced Pt/C deposition

2.2.2 Estimating Thermal Contact Resistance

In order to estimate the effect of contact resistance, we follow the analysis in Yu et al. [53] and approximate the contacts between the beam and the membrane as rectangular fins. The thermal contact resistance R_c can be approximated as [57]:

$$R_c = \frac{1}{4} \cdot \frac{1}{\sqrt{hPkA_c}\ \tanh\left(\sqrt{\dfrac{hP}{kA_c}}\ L_c\right)} \tag{2.5}$$

where h (W/m^{2}K) is the lateral heat transfer coefficient between the nanowire and Platinum contact on the pads, P is the effective perimeter of contacts performing as fins (the nanowire touches the membranes at the Platinum electrodes, each L_c in width as shown in Fig 2.5(b,c)), k is the thermal conductivity of the nanowire and A_c is the cross-sectional area of the nanowire. Note here that we have considered two different geometries for the nanowire: circular and rectangular. For the circular case, $A_c = \pi d^2/4$ and when rectangular, $A_c = w \cdot l$. Let us approximate $h \approx k_I / L_I$ [53], where k_I is the estimated thermal conductivity and L_I is the length of the ill-defined interface between the nanowire and the Pt electrodes on the suspended membrane, as illustrated by Fig 2.5(c) in black. In order to determine the maximum possible thermal contact resistance, R_c, let us consider the scenario where the interface is sandwiched between the nanowire and the Platinum electrode, as illustrated in Figure 2.5(c).
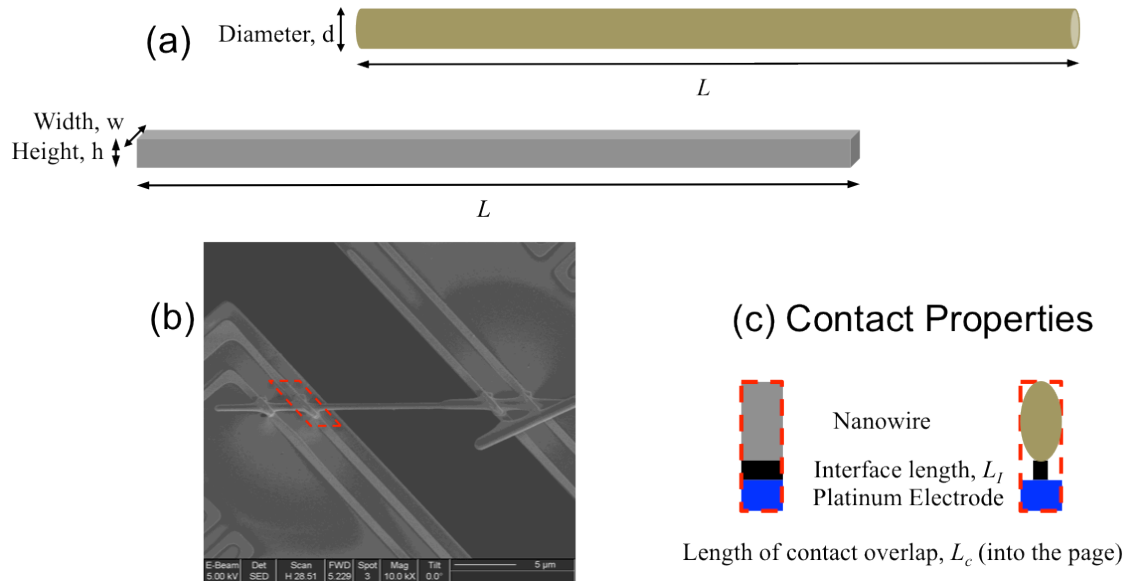
Figure 2.5 (a) A representation of the typical geometry of nanowires. (b) Top view Scanning Electron Micrograph of a rectangular cross-section nanowire geometry and Pt/C Focused Ion Beam Induced Deposits (FIBID) to improve thermal contact resistance and also provide electrical contact to the Platinum electrodes on the suspended membranes. (c) Cross-section diagram of each of four contacts between the nanowire (grey) and the Platinum Electrode (blue) on the suspended membrane, with the interface (black). The length of the interface is defined as L_I, and the overlap between the nanowire and the Platinum Electrode is defined as L_c. Both rectangular and circular cross-sections are illustrated.

In the circular case, one can approximate line contact with a length of L_c whereas when the nanowire cross-section is rectangular, the area of contact is given by $w*L_c$. The unknowns in Equation 2.5 are thus: k_I and L_I.

a) <u>Interface conductivity, k_I:</u> The worst scenario is all-vacuum contact, which is avoided by doing a tilted SEM and ensuring that the contact between the nanowire and Pt electrode is good. Especially once the FIBID based Pt/C composite is placed on the electrode, the area is observed with with tilted SEM to be filled. Hence, the realistic lower limit is Pt/C composite with 30% Pt. This is an organometallic, with Pt particles joined by an organic substance [58] and is known to resemble metal powders with 30% porosity (air gaps), which has a lower limit of thermal conductivity of k_I =1 W/m-K at room temperature [59]. In the other extreme, the best-case scenario in the limit of perfect contact, is the Pt thermal conductivity itself, which is 20-30 W/m-K depending on the grain sizes for thin film Platinum.

b) <u>Length of the interface, L_I:</u> The length of the contact can be approximated to span values from 1 nm to 10 nm as an extreme case.

This calculation has been performed for the case of a circular carbon nanofiber by Yu et. al. [53] and is reproduced below in Fig 2.6.
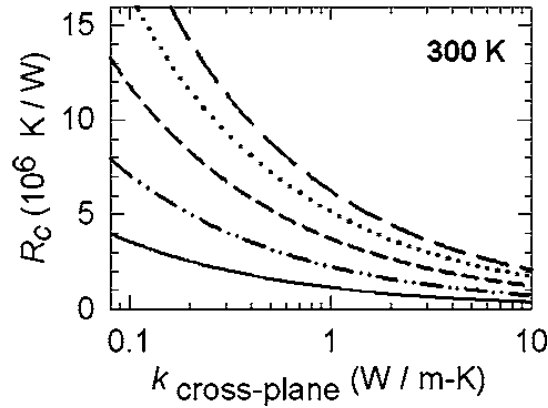
Figure 2.6. Thermal Contact Resistance, R_c estimated for a carbon nanofiber using Equation 2.5 for L_I varying from 0.1nm (large dashed line) upto 100nm (solid line) for different values of k_I (shown here as $k_{cross-plane}$) reproduced from Yu et. al. [53]

As an illustration of the rectangular nanowire cross-section, let us consider measurement of the thermal conductivity of Vanadium Dioxide (VO_2) beams, which have a rectangular cross-section, the results are shared in Chapter 4 of this thesis. The expected thermal conductivity of VO_2 is ~4-6 W/m-K in the insulating phase at 300K [60–62]. The typical cross-section of the beams is rectangular with the width, w and height, h around 500nm to 1.5μm. Using an average cross-sectional area based on these dimensions, and approximating k = 5 W/m-K for the VO_2 beam, we expect the beam conductance to be 58.6 nW/K. The actual measured conductance is 56 nW/K, which is agreeably close to the expected value. For other geometries of nanowires measured in this study, the range of measured thermal conductances is between 50 to 200 nW/K. This translates to the measured thermal resistance, R_{th} = 1/G between the two pads of between 5 and 20 K/μW.

Again, considering k_I and L_I as the two important length scales for the contact, and considering a range of values in Equation 2.5, Fig 2.7 shows the values of the thermal contact resistance (R_c) for different values of the unknown parameters:
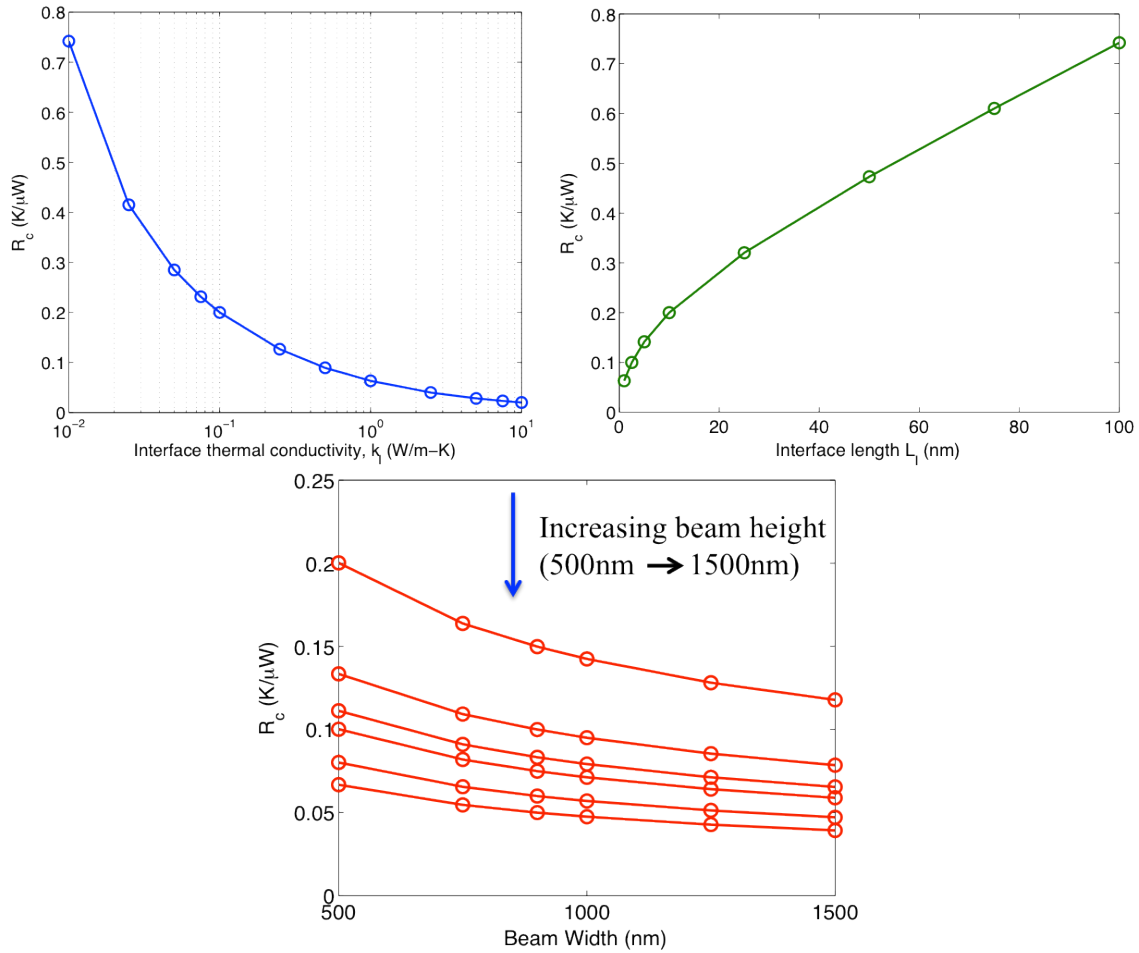
Figure 2.7 (a) The thermal contact resistance, R_c as a function of the interface thermal conductivity, k_I approximating the contact area as a fin with adiabatic ends and a contact length of 1μm. The maximum $R_c \sim 0.75$ K/μW is when $k_I = 0.01$ W/m-K. For this graph, $L_I = 10$ nm, $w = 500$ nm and $h = 500$ nm. (b) Predicted thermal contact resistance, R_c as a function of expected values of the interface length, L_I ranging from 1 to 100 nm where $k_I = 0.1$ W/m-K, $w = 500$ nm and $h = 500$nm. (c) Predicted thermal contact resistance, R_c as a function of beam widths and heights ranging from 500 nm to 1.5 μm when $k_I = 0.1$ W/m-K and $L_I = 10$ nm.

For the circular nanowire cross-section, as seen in Fig 2.6 the maximum value of the contact resistance is given by $R_c < 15$ K/μW, while realistically, we can expect $k_I \sim 1$ W/m-K, resulting in $R_c \sim 5$ K/μW, which was shown to be about 10% of the measured thermal resistance.

On the other hand, in Fig. 2.7(a) for the rectangular cross-section, we have plotted R_c as a function of different k_I ranging from 0.01 W/m-K to 10 W/m-K. As can be seen from this figure, R_c is expected to be < 0.75 K/μW for a large area of contact, which is at most 15% of our measured resistance. Note that we have used a beam width and height of 500 nm

and L_I = 10 nm. Fig. 2.7(b) shows the effect that the interface length, L_I has on R_c. Even in the extreme case of L_I = 100 nm, assuming k_I = 0.1 W/m-K, we only get R_c ~ 0.75 K/μW. Finally, as expected, the contact resistance decreases as we increase the beam width upto 1.5 μm, as the area of contact increases as illustrated in Fig. 2.7(c). Here, we assume k_I = 0.1 W/m-K and L_I = 10 nm.

Another way of estimating the contact resistance is by considering the thermal interface resistance reported in literature for highly dissimilar materials. Even in this limit, the smallest thermal interface conductance between two solids is given by G_c' ~ 10 MW/m²-K [63]. Considering this value for the contact area in our rectangular beam system given by w = 500 nm, L_c = 1 μm, we obtain

$$R_c = 2 \cdot \frac{1}{G_c'A} < \frac{2}{\left(10\,MW\,m^{-2}\,K^{-1} \cdot 500\,nm \cdot 1\,\mu m\right)} = 0.4\,K\!\big/\!\mu W$$

which is at most 8% of our measured thermal resistance.

In summary, by approximating the contact area between the nanowire and the electrodes on the membranes as fins, we can expect that the thermal contact resistance is only about 10% of the measured thermal resistance.

2.2.3 Experimentally determining thermal contact resistance in Silicon Nanowires

Theoretical estimation of the contact resistance as done in the previous section suffers from many inadequacies. In particular, the thermal interface resistance between the nanowire and the membranes is unknown. Experimentally, the contact resistance can be determined by plotting the measured thermal resistance as a function of different lengths of the nanowires. Of course, since the thermal conductivity is diameter-dependent, the measurement was done with nanowires of the same diameter. Results of this measurement are shown below:
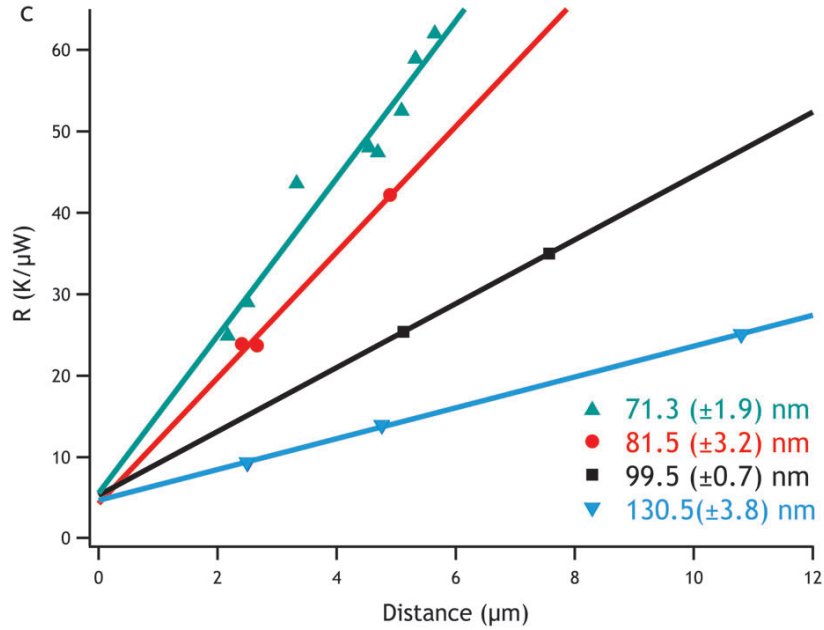
Figure 2.8 Thermal resistance of VLS Si nanowires with various lengths and diameters. The intercept on Y axis indicates the average contact resistance ~ 4.5 K/μW, which is less than 10% of VLS nanowires with 71.3 nm diameter and 5 μm length. Reproduced from J. Lim et. al. [64]

Here, we have plotted the measured overall thermal resistance as a function of the distance between the two membranes. The residual thermal resistance at zero length gives us the thermal contact resistance. The slope is linear since transport through the nanowires is diffusive. The slopes are different since the thermal conductivity of different diameter nanowires is different. Interestingly, as is seen in Fig 2.8, the residual resistance is not diameter-dependent. This is expected, as the area enhancement from the Pt/C composite envelope will dominate the reduction in the residual resistance. Hence, once the Focused Electron Beam Induced Deposition (FEBID) is performed on the nanowires whose thermal conductivity needs to be ascertained, the residual thermal contact resistance in these samples is ~4.5 K/μW. In principle, if the geometry of the nanowires can be controlled, thermal devices with different gaps (lengths between membranes) can be used to perform a length series and the y-asymptote of the linear curve gives the contact resistance. Since we perform the same operation on all our nanowires, for the rest of our studies, we've used this number as a reference for the thermal contact resistance.

2.2.4 Eliminating thermal contact resistance with integrated nanowires

In order to experimentally probe the phonon transport in SiNWs in a systematic manner, it is necessary to measure the thermal conductivity of samples with precisely controlled dimensions. Several groups, including ours, have experimentally investigated phonon transport in nanowires [16], [35], [36], [65]. Generally, a single nanowire is placed on the micro-fabricated thermal measurement device by either drop-casting or micromanipulation. There is limited control over how the nanowire is positioned and which nanowire from a solution bridges the measurement device. Thus, it is challenging to systematically measure nanowires with desired dimensions. Furthermore, the nanowires are anchored on the measurement device using the FEBID as described in the previous section, which inevitably introduces an unknown thermal contact resistance. Although it has been shown that the thermal contact resistance has minor effects [51–53], it can vary from sample-to-sample and is hard to control. Our new approach reduces these uncertainties and allows us to better understand phonon transport in low-dimensional structures.

We designed and fabricated suspended micro-devices with integrated SiNWs with rectangular cross sections for direct thermal transport measurement. This design eliminates contact resistance and the fabrication, which is based on high-resolution electron beam lithography (EBL), offers precise control of key variables such as the thickness, width and length of SiNWs. The thermal transport in the SiNWs was systematically investigated using these novel micro-devices. The reported design and fabrication process can be extended for the investigation of thermal transport in a wide range of materials and structures, including grids, ribbons and thin films.

A scanning electron micrograph (SEM) of a micro-device is shown in Figure 2.9. The suspended device consists of two 25×40 μm pads that are suspended by six 2-μm-wide, 0.3-μm-thick and 450-μm-long low-stress silicon nitride (LSN) beams. The pads contain two layers; the top layer is a 0.3-μm-thick LSN membrane and the bottom layer is a single-crystalline silicon membrane with variable thickness. One or more single crystalline silicon nanowires with the same thickness as the silicon membranes have monolithic contact with the two pads. A 30-nm-thick, 1-μm-wide platinum resistance coil, which can work as a heater and a thermometer, is on top of each LSN membrane. The platinum resistance coils are connected to 200×200 μm platinum bonding pads on the substrate via four 200-nm-thick and 2-μm-wide platinum leads deposited on the long silicon nitride beams. Two of the leads supply electrical current to the coil, and the other two are used to measure the voltage drop across the coil. Two 60-nm-thick and 2-μm-wide platinum electrodes are on the exposed top surface of the silicon membrane to provide electrical contacts for the SiNWs.
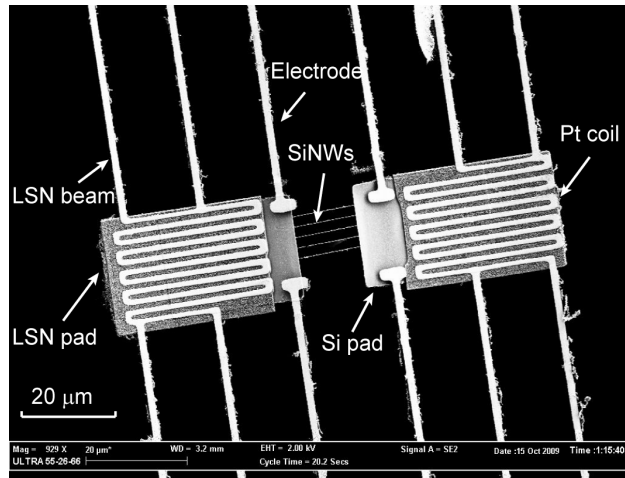
Figure 2.9 SEM image of the suspended microdevice with integrated SiNWs.

The device is batch fabricated using a single silicon-on-insulator (SOI) wafer and micro-fabrication technology. The fabrication process is shown in Figure 2.10. The device layer of a 4-inch SOI wafer (340 nm Si/ 400 nm buffered SiO_2/ 500 μm Si) is thermally oxidized with careful control over final thickness. The resulting silicon oxide layer is etched using a 10:1 buffered HF solution (10-100 nm) (Figure 2.10(a)). The thickness of the device layer at several spots was initially measured using a small spot spectroscopic reflectometer. A 60-nm-thick layer of PMMA (polym(methyl methacrylate), a positive photoresist) is then spun on the silicon surface. The SiNWs are patterned onto the PMMA layer by electron beam lithography (EBL) (Figure 2.10(b)) and a 20-nm thick film of Cr is thermally evaporated. A PMMA liftoff process is used to define the SiNWs. The Si pads that connect to SiNWs are defined by photolithography and 20-nm-thick Cr deposition (Figure 2.10(c)). Using the Cr pattern as a mask, the unprotected Si layer is etched away by reactive ion etching (RIE), and a Cr-7 solution is used to remove the Cr (Figure 2.10(d)). The thicknesses of the SiNWs are then measured by a surface profiler. The results of the surface profiler measurement are in good agreement with thickness measurements performed using spectroscopic reflectometer. To protect the SiNWs, a 300 nm thick low-temperature oxide (LTO) film is deposited by low-pressure chemical vapor deposition (LPCVD). A small window covering the SiNWs are defined by photolithography, and a 10:1 buffered HF solution is used to remove the exposed LTO layer. The small LTO window serves as a buffer layer during the subsequent silicon nitride etching and is removed in the final release step. A 200 nm-thick low stress silicon nitride (LSN) is then deposited on the substrate using LPCVD at 700 K (Figure 2.10(e)). The platinum coil, leads and electrodes are defined by photolithography. A 10-nm-thick Cr layer and then a 200 nm-thick platinum layer are deposited in sequence on the top of the photoresist using direct current (DC) and radio-frequency (RF) sputtering, respectively. Acetone is used to remove the photoresist in a liftoff process, which transfers the photoresist pattern to the Cr/ Pt layer. Reactive ion etching (RIE) is used to etch the Pt layer to increase the resistance of the Pt heater coils (Figure 2.10(f)). A 1-μm-thick I-line photoresist is spun on the substrate, patterned with

47

photolithography and hard-baked. The exposed portions of the nitride film is etched away by nitride RIE, and the wafer is immersed in acetone to remove the photoresist (Figure 2.10(g)). Photolithography and 10:1 buffered HF wet etching are used to open small windows on the exposed LTO layer. This shortens the subsequent oxide etching time and avoids the damage to SiNWs. To release the device, the thick silicon substrate below the device is removed from the backside. 8-10 µm thick I-line photoresist is spun on the backside of the wafer, and backside alignment and photolithography are used to open windows on the backside of the wafer that correspond to the patterned devices on the SOI device layer. The wafer is then attached to a 6 inch dummy wafer coated with 8-um-thick I-line photoresist. The wafers are baked together at 120 ℃ for 3 hours and deep silicon etching is performed on the backside of the wafer to etch the silicon under the opened backside windows until the buffered oxide layer of the SOI wafer is exposed (Figure 2.10(h)). After immersing the wafer into acetone for 12 hours to remove the thick photoresist layer, critical point drying (CPD) is used to dry the wafer to avoid the possible damage to the SiNWs caused by surface tension (not shown). The dried wafer is then cut into small chips (8 x 8 mm). HF vapor etching at 50℃ is performed from the front side to etch both the protective LTO on the top of the SiNWs and the exposed buffer oxide layer beneath the devices. The HF vapor etching releases the SiNWs so that the entire structure is suspended (Figure 2.10(k)). The released SiNWs are inspected using optical and scanning electron microscopy (SEM) to ensure that the wires are clean and intact. SEM is also used to determine the width and the length of individual SiNWs.
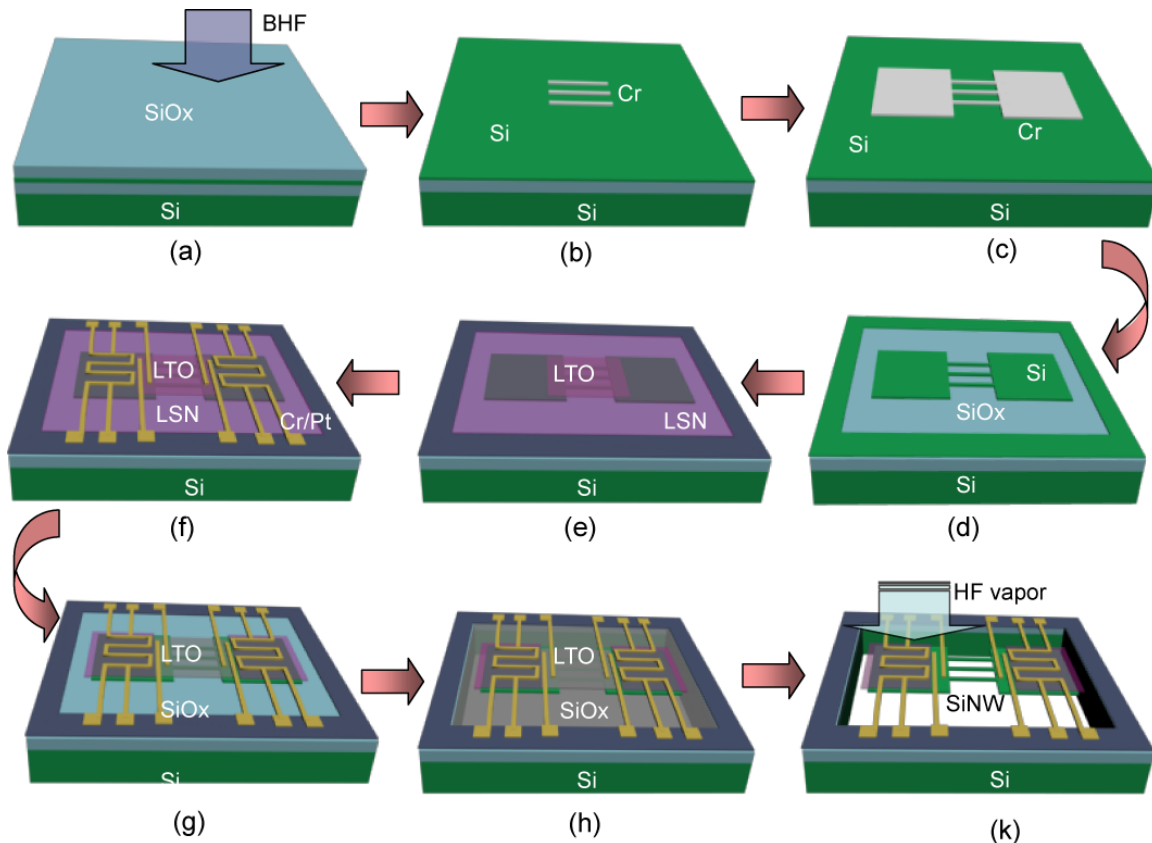
Figure 2.10 Fabrication sequence for the microdevices with integrated SiNWs: (a) thermal oxidization and HF wet etching to thin the SOI device layer, (b) SiNWs patterning by EBL and Cr deposition, (c) Si pads patterning by photolithography, (d) RIE of Si to define SiNWs and Si pads. (e) Patterning of protective LTO windows and LSN Deposition, (f) Patterning of heater coils and beams by photolithography and Cr/Pt deposition. (g) RIE for LSN. (h) Backside alignment and deep silicon etching, (k) Release of final suspended structure by HF vapor etching.

Up to ~2000 suspended devices with SiNWs of varying widths and lengths can be fabricated on a 4-inch SOI wafer using the fabrication method described above. There is some non-uniformity in the thickness and width of SiNWs across the entire wafer due process variation. For the small chips, which are 8 x 8 mm and consist of 64 devices, the non-uniformity is less than 5%. The thicknesses, widths and lengths of the fabricated SiNWs are controllable, e.g., deviation in width from the design is less than 20% for 50 nm-wide wires. Figure 2.11 shows that SiNWs with thickness of 20-100 nm, width of 40-150 nm and length of 4-100 μm have been fabricated. SiNWs with an extremely high aspect (length/width or thickness > 1000) have been attained (refer to Figure 2.11(d)), which is difficult to achieve by traditional nanowire measurement techniques. Figure 2.11(b) illustrates that the technique can also be used to fabricate suspended structure with an integrated thin silicon ribbon or film.
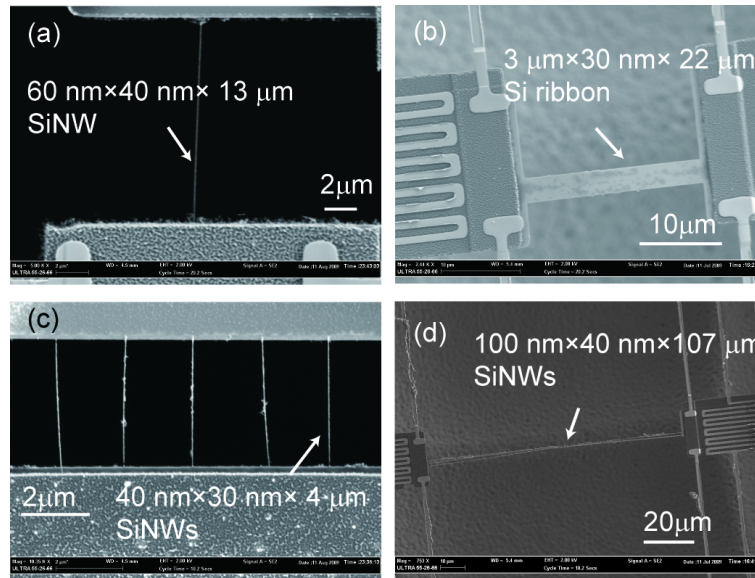
Figure 2.11 SEM images of (a) 60-nm-wide, 40-nm-thick and 13-μm-long SiNW, (b) 3-μm-wide, 30-nm-thick and 22-μm-long Si ribbon, (c) five 40-nm-wide, 30-nm-thick and 5-μm-long SiNWs (Note that there is some residual oxide on the 3 wires in the center), (d) three 100-nm-wide, 40-nm-thick and 107-μm-long SiNWs.

Figure 2.12 shows the TEM pictures of the fabricated SiNWs. The fabricated SiNWs still remain single crystalline structure and no defects such as pores or constrictions have been detected on the wires.
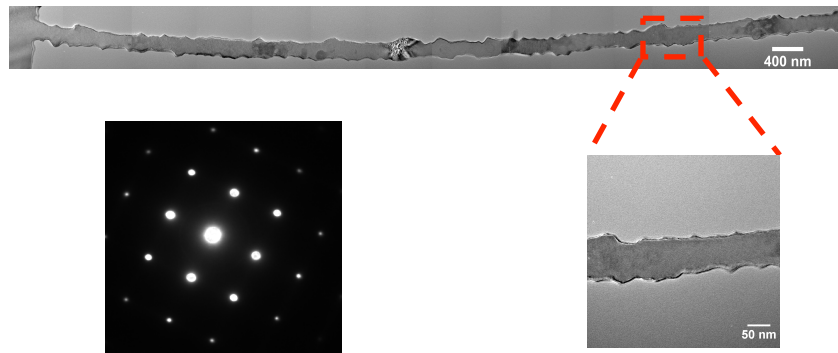
Figure 2.12 TEM image of an EBL Si nanowire (a) Multiple Bright Field TEM pictures taken along the length of the wire have been put together as a series to view the surface morphology of the whole wire. A typical low resolution TEM picture more clearly shows the surface profile. The defect areas were formed as a result of performing Convergent Beam Electron Diffraction (CBED) at 300kV. (b) Multiple Selected Area Electron Diffraction (SAED) images taken along different points on the wire show the same single-crystalline orientation. The representative SAED image shown here is the zone axis orientation, the axial crystalline direction was not determined.

Fabricated wires with identical cross-sections and different lengths were measured at room temperature (300K) to determine the contact resistance between the SiNWs and the measurement device. Two batches of SiNWs with different cross-sections were analyzed. The nanowires in batch 1 have widths of 100 +/- 5 nm and approximate device layer thicknesses of 20 nm. Because the thicknesses of the nanowires in batch 1 were not measured with a surface profiler before release, the samples were not used for thermal conductivity measurements. Instead, the thickness was determined by measuring the SOI device layer thickness before EBL pattering at several sites on the wafer using a small spot spectroscopic reflectometer. The nanowires in batch 2 have widths of 120 +/- 5 nm and device layer thicknesses of 40 +/- 1 nm. The device layer thickness for the second batch of SiNWs was measured using a surface profiler with ±1 nm uncertainty. Within each batch, the nanowires are expected to have a similar thickness (batch 1 < 10 % deviation; batch 2 < 5% deviation). The widths of all the SiNWs were measured using a SEM.

In the diffusive regime of phonon transport where the thermal conductivity is independent of nanowire length, the conductance, $G_W = kA/L$, is expected to scale inversely with the nanowire length, L. Figure 2.13 shows the measured wire thermal resistance R_W ($R_W = 1/G_W$) as a function of nanowire length for batches 1 and 2. A linear fit through the data points shows that the residual conductance at $L = 0$ μm is negligible, indicating that the monolithic contact within the device layer eliminates the contact resistance between the nanowires and the measurement device. This is an ideal scenario for accurate measurement of thermal conductivity and controlled investigation of fundamental phonon transport of quasi one-dimensional nanowires. Comparing this with the nanowire results for silicon nanowires shown in Figure 2.8, with residual thermal contact resistance of ~4.5 K/μW, shows the significant improvement we've achieved in eliminating contact resistance completely.
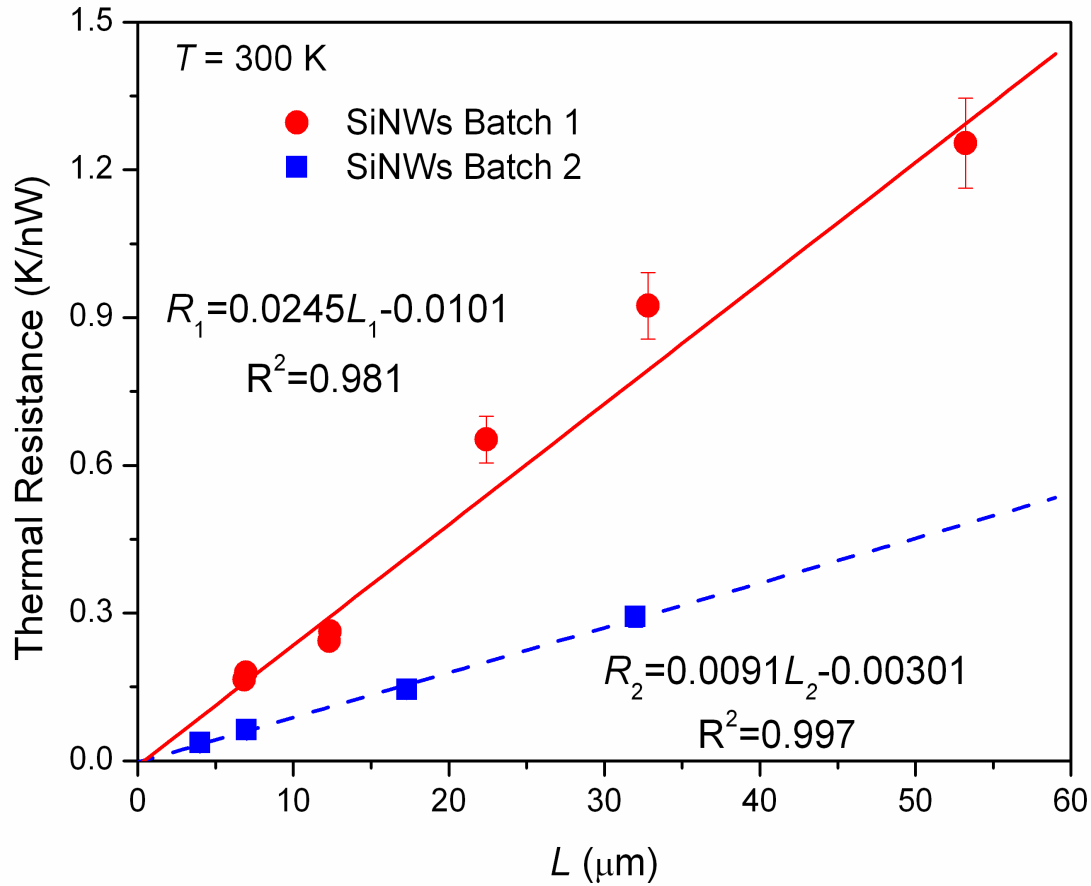
Figure 2.13 Plot of the thermal Resistance (K/nW) as a function of nanowire length (3μm up to 50 μm) for Batch 1 (circles) and Batch 2 (triangles). The linear fit passes very close to the origin indicating nearly zero contact resistance. Error bars are included for all points.

2.3 NOISE EQUIVALENT THERMAL CONDUCTANCE

From Section 2.2, it is obvious that the contact problem can be solved simply by making the suspended part of the nanowire as long as experimentally possible. This is of course difficult since designing and making quasi-1D materials with very large aspect ratios can be challenging. On the measurement side, there is a limit to the length of the samples that stems from the sensitivity of the measurement scheme. We have used the measurement scheme well described in Li Shi et. al. and by Deyu Li [52], [55] and have no further modifications to this scheme. However an understanding of the lowest measurable thermal conductance is necessary to get an idea about the limits of the system.

Following Prof. Deyu Li's analysis of the noise floor of the measurement, the noise equivalent conductance (NEG) can be defined as:

$$NEG = G_b \frac{NET}{\Delta T_h - \Delta T_s} \tag{2.6}$$

where NET is the noise equivalent thermal change that can be accurately estimated from the change in resistance of the Platinum Resistance Thermometer (PRT). Now, this is given by:

$$NET = \frac{NER_s / R_s}{TCR} = \frac{\left(\frac{\delta v}{v} + \frac{\delta i}{i}\right)}{TCR} \tag{2.7}$$

where NER_s is the noise equivalent sensing resistance (in other words what is the smallest change in the sensing resistance as a function of temperature change that can be measured by the electronics). TCR is the Temperature Coefficient of Resistivity, which is a material property for a thin film of Platinum. Therefore, the dominant noise source is the AC current supplied by the lockin amplifier on the sensing side. Deyu Li [55] showed that $NER_s / R_s \approx 5 \times 10^{-5}$ for Johnson noise limited voltage measurement using a precision 1MΩ resistor, and we verify this same electrical noise floor in our measurement at a bandwidth, Δf=0.3Hz. For a Platinum thin film of ~50 nm, TCR at 300K is ~1.5x10^{-3} K^{-1} and ~3.0x10^{-3} K^{-1} at 100K. Using this number, the noise equivalent temperature is then ~33 mK at 300 K and ~17 mK at 100K. This noise from the AC resistance measurement of the PRT on the sensing side is similar to the temperature oscillations of the cryostat, which is ~30 mK at 300K and ~10 mK at 100K.

In our micro-fabricated structures, the beam conductance, G_b is about 60-100 nW/K and the largest temperature excursion across the nanowire is given by: $(\Delta T_h - \Delta T_s) \sim 5K$. We can obtain an estimate for the NEG based on Equation 2.6. At 300K, NEG ~ 400 pW/K, hence, our platform is a nano-watt resolution calorimeter (~2 nW). Below 100K, this improves by a factor of two, giving a NEG ~ 200 pW/K, such that we can perform calorimetry with ~1 nW resolution.

It is worth noting that significant progress has been made in recent years in the sensitivity of resistance based thermometry. In 2011, Wingert et. al. [66] employed a Wheatstone Bridge circuit with another resistor, R_s' inside the cryostat next to the sensing membrane resistor, R_s, forming a pair. The first advantage gained was that the temperature fluctuations in the cryostat were cancelled out as they were seen equally by the paired resistors. Secondly, the non-linear bridge circuit improved the accuracy of the resistance measurement, improving NER_s significantly. Wingert et. al. were able to measure NET_s ~1 mK at room temperature, which is ~30 times improvement compared to the traditional

setup, as shown in Fig 2.14 below. Using Equation 2.6, they were thus able to obtain a noise equivalent thermal conductance, NEG_s of ~10 pW/K, which is about 40 times better than the current setup.
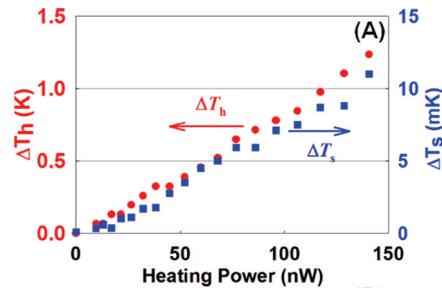
Figure 2.14 Measured ΔT_s and ΔT_h as a function of heating power. NET_s ~1 mK, leading to NEG_s ~10 pW/K. Adapted from Wingert et. al. [66]

Sadat et. al. improved the temperature resolution of the suspended platform further by incorporating a bi-material cantilever sensor that has a sensitivity of ~4 μK in vacuum [67] as seen below in Fig 2.15. With beam conductance, G_b of ~600 nW/K, they could perform calorimetry down to the level of ~4 pW, which is a subsequent improvement of a factor of 2 compared to Wingert et. al. [66] albeit with an additional geometry due to the suspended cantilever.
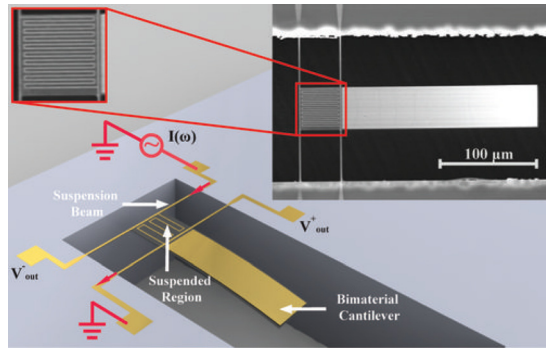
Figure 2.15 Bi-material Cantilever based calorimeter with ~4pW resolution with NET_s ~4μK. Adapted from Sadat et. al. [67]

Sadat et. al. [68] also used AC heating coupled with AC sensing to improve the temperature resolution purely for patterned PRTs upto ~30 μK, which was then incorporated into the bridge design pioneered by Wingert et. al. to achieve a NEG_s of 5 pW/K [69]. These improvements in the measurement scheme can potentially be used to measure the thermal conductance of DNA, single polymer chains and other dielectric nanotubes with extremely small dimensions.

2.4 MEASUREMENT PRACTICE

In order to minimize the effect of thermal contact resistance and ensure accurate measurement of thermal conductivity of single nanowires the measurements have to be iterative. The two limits of the measurement stem from:

(1) Contact resistance when the suspended section of the nanowire is short. For illustrative purposes, we'll use the value of 5 K/μW as the contact resistance for circular cross-section nanowires (with line contact and Pt/C FEB). Similarly, thermal contact resistance for a rectangular beam has an upper limit of ~1 K/μW. Hence, for 10% contribution from contact resistance, the measured thermal resistance of the system (including the contacts) needs to be higher than 50 K/μW (20 nW/K) for a nanowire with circular cross-section and 10 K/μW (100 nW/K) for a rectangular beam. In an ideal scenario where different nanowires with the exact same cross-section can be manufactured (which depends on the expertise of the materials growers!) a length series can be performed similar to Fig 2.8 and 2.13 to extract the exact contact resistance.

(2) Sensitivity of the sensing side when the suspended section of the nanowire is long. This is a function of the design of the measurement scheme and for our measurement system with no additional bridge circuit or improved temperature resolution, $NEG_s \sim 400$ pW/K, hence maximum possible measurable thermal resistance is 2500 K/μW. Thus, for a signal-to-noise ratio of 10:1, the limit of measurement would be ~250 K/μW.

Thus, a measurable range of nanowire thermal resistances with <10% error would be between 50 and 250 K/μW for a circular cross-section and between 10 and 250 K/μW for a rectangular cross-section.

In summary, the following steps must be followed in order to obtain accurate estimation of the thermal properties of the nanowires:

a. Place the single nanowires of material X on the measurement platform with good contact between the nanowire edge and the electrodes on the membranes.
b. Depending on the properties of material X, improve the contact area between the nanowire and the Platinum electrodes using either a Focused Ion or an Electron Beam (FIB or FEB) induced deposition. FIB uses Ga^+ ions to dissociate the Pt/C precursor gas which subsequently deposits around the nanowire. FEB uses the secondary electrons in a Scanning Electron Microscope (typically at lower energies ~5keV) to achieve deposition around the selected patterned area.
c. Measure the thermal conductance of the nanowire including the contacts. Ensure that the measured conductance is significantly larger than the NEG_s, and the temperature drop occurs mainly in the nanowire and negligibly at the contacts (small contact resistance). This can be achieved by selecting the correct geometry and length of the nanowire, as $G_w = {k_w A}/{L}$. Repeat the measurement with the correct length to obtain an accurate estimate of the nanowire conductance.

d. Measure the cross-sectional geometry and the suspended length of the nanowire and extract the thermal conductivity from the measured conductance.

The error analysis of the measurement scheme is addressed in Appendix 2A below. Another important consideration while performing measurements of thermal conductivity of nanowires using this platform is the problem of platinum migration during the FIB/FEB process and this is addressed in Appendix 2B.

Appendix 2A: Error Analysis for Thermal Conductance Measurements

Following Equation (2.2), the heat flow through the nanowire can be written as:

$$Q = \gamma \cdot \frac{I_h^2 R_h}{\left(\Delta T_h + \Delta T_s\right)} \cdot \Delta T_s \qquad (2A.1)$$

where γ is a non-dimensional ratio of the resistance of the PRT and the resistance of the suspended legs. γ is a constant at all temperatures. To determine the nanowire conductance, Equation (2.3) gives us:

$$G_w = \frac{Q}{\Delta T_h - \Delta T_s} \qquad (2A.2)$$

Then, error propagation rules determine that:

$$\left(\frac{\delta Q}{Q}\right)^2 = 2 \cdot \left(\frac{\delta I_h}{I_h}\right)^2 + \left(\frac{\delta R_h}{R_h}\right)^2 + \left(\frac{\delta\left(\Delta T_s\right)}{\Delta T_s}\right)^2 + \left(\frac{\delta\left(\Delta T_h + \Delta T_s\right)}{\Delta T_h + \Delta T_s}\right)^2 \qquad (2A.3)$$

and,

$$\left(\frac{\delta G}{G}\right)^2 = \left(\frac{\delta Q}{Q}\right)^2 + \left(\frac{\delta\left(\Delta T_h - \Delta T_s\right)}{\Delta T_h - \Delta T_s}\right)^2 \qquad (2A.4)$$

Hence, the following error terms need to be determined:

(1) $\dfrac{\delta R_h}{R_h}$, (2) $\dfrac{\delta\left(\Delta T_s\right)}{\Delta T_s}$, (3) $\dfrac{\delta\left(\Delta T_h + \Delta T_s\right)}{\Delta T_h + \Delta T_s}$ and (4) $\dfrac{\delta\left(\Delta T_h - \Delta T_s\right)}{\Delta T_h - \Delta T_s}$

The linear dependence of the PRT resistance with respect to temperature allows us to define ΔT_s and ΔT_h. One cycle of measurement constitutes gathering this raw data at 5 different local temperature points around T_G. Let's consider obtaining $\partial R_{h/s} \big/ \partial T_{h/s} \approx \Delta R_{h/s} \big/ \Delta T_{h/s}$ at T_G = 300K. Then, we measure the resistances $R_{s,G}$ and $R_{h,G}$ at 295K, 298K, 300K, 302K and 305K. The plot of resistance as a function of global stage temperature is typically linear as below:
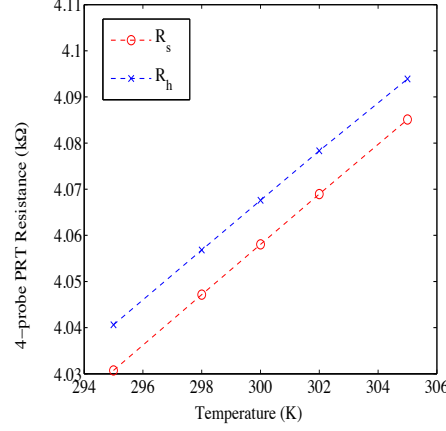
Figure 2A.1 Measured R_s and R_h around T_G=300K used for calibration of TCR.

If we define $\alpha_s \equiv dR_s/dT_G \sim \Delta R_s/\Delta T_G$ and $\alpha_h \equiv dR_h/dT_G \sim \Delta R_h/\Delta T_G$ then these slopes can be determined to very high accuracy. In general, $\delta\alpha_s/\alpha_s$ and $\delta\alpha_h/\alpha_h \leq 4\times10^{-2}$ when $R^2 >$ 0.9999 for the least squares fitting shown in Fig 2A.1 above. To understand where this error comes from, consider the following error propagation (where *i = h or s)*:

$$\left(\frac{\delta\alpha_i}{\alpha_i}\right)^2 = \left(\frac{\delta(\Delta R_i)}{\Delta R_i}\right)^2 + \left(\frac{\delta(\Delta T_i)}{\Delta T_i}\right)^2 \tag{2A.5}$$

Following the analysis of Shi [55], we have verified that $\frac{\delta R_i}{R_i} = \sqrt{\left(\frac{\delta v_{out}}{v_{out}}\right)^2 + \left(\frac{\delta i_{ac}}{i_{ac}}\right)^2} \approx 5\times10^{-5}$

from the AC measurements of the 4-probe resistance using a lock-in amplifier on both the heating and sensing sides. We haven't described the detailed error contributions for this term, but these are similar to those calculated in Shi [52] and Li [55] and as is seen later in this analysis, two orders of magnitude smaller in comparison to other sources of error in the measurement.

To determine the slope α_i, we use a temperature excursion of $\Delta T = 10K$. Then, $\delta(\Delta T_i) = \sqrt{2} \cdot \delta T_i \approx \sqrt{2} \cdot 40mK = 57mK$. Hence, $\frac{\delta(\Delta T_i)}{\Delta T_i} \approx \frac{57mK}{10K} \approx 5.7\times10^{-3}$. Therefore, we should expect $\left(\frac{\delta\alpha_i}{\alpha_i}\right) \approx 6\times10^{-3}$ at most from direct measurement of the 4-probe resistance

and the cryostat temperature. However, this analysis doesn't account for temperature fluctuations of the cryostat ~30-40 mK (at room temperature) which are unavoidable. We wait for up to 60 minutes at each gate temperature for the cryostat head temperature to stabilize. Hence, the maximum possible error in estimation of slope is given by

58

$\delta\alpha_i\!\Big/\!\alpha_i = 4\%$ (obtained from the Root Mean Squared Error of the linear fit to the Resistance, R_i vs Temperature, T_i curve) where i represents either the heating or the sensing side.

Now, the error in ΔT_s and ΔT_h can be determined from the relation:

$$\frac{\delta(\Delta T_i)}{\Delta T_i} = \sqrt{\left(\frac{\delta(\Delta R_i)}{R_i}\right)^2 + \left(\frac{\delta\alpha_i}{\alpha_i}\right)^2} \approx \sqrt{\left(5\times10^{-5}\right)^2 + \left(4\times10^{-2}\right)^2} \approx 4\times10^{-2} = 4\% \qquad (2A.6)$$

In order to determine the errors in (3) and (4) above, let us consider typical values of ΔT_s and ΔT_h. For the VO$_2$ beams, in general, we observe that $\Delta T_s \geq 1K$ for $\Delta T_h \leq 2.5K$. Hence, we can approximate $\Delta T_h - \Delta T_s \approx 1.5K$ and $\Delta T_h + \Delta T_s \approx 3.5K$. Then,

$$\frac{\delta(\Delta T_h + \Delta T_s)}{\Delta T_h + \Delta T_s} = \frac{\sqrt{2}\cdot\delta(\Delta T_s)}{\Delta T_h + \Delta T_s} \approx \frac{\sqrt{2}\cdot 4\% \cdot 1K}{3.5K} \approx 1.6\%$$

Similarly, we can obtain

$$\frac{\delta(\Delta T_h - \Delta T_s)}{\Delta T_h - \Delta T_s} = \frac{\sqrt{2}\cdot\delta(\Delta T_s)}{\Delta T_h - \Delta T_s} \approx \frac{\sqrt{2}\cdot(4\%)\cdot 1K}{1.5K} \approx 3.8\%$$

Going back to Equation (2A.3) above, we can thus estimate the error in Q (heat flux) to be:

$$\frac{\delta Q}{Q} = \sqrt{2\cdot\left(4.2\times10^{-5}\right)^2 + \left(5\times10^{-5}\right)^2 + \left(4\times10^{-2}\right)^2 + \left(1.6\times10^{-2}\right)^2} \approx 4.3\%$$

Then, the error in conductance, G if defined as $Q\!\Big/\!\Delta T$ is given by Equation (2A.4):

$$\frac{\delta G}{G} = \sqrt{\left(4.3\times10^{-2}\right)^2 + \left(3.8\times10^{-2}\right)^2} \approx 5.74\%$$

However, this is the error obtained for a single data-point for the case $G \equiv \dfrac{Q}{\Delta T}$.
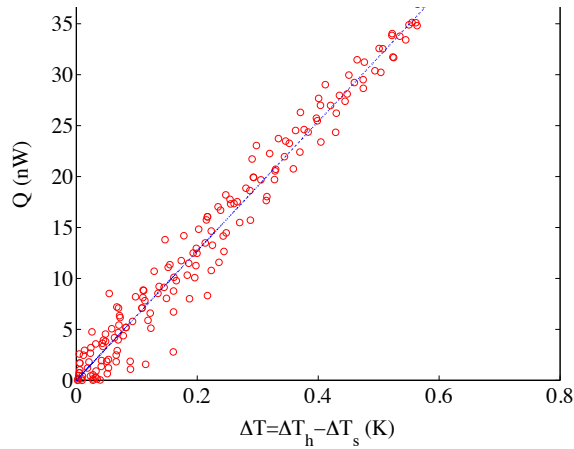
Figure 2A.2 Heat flow through the tapered VO$_2$ beam I, Q in nW/K as a function of the temperature difference across the beam, ΔT in K at T$_G$ = 300K.

In practice, we obtain 200 such points during each measurement cycle as shown in Fig 2A.2 above. Further, we repeat each measurement cycle 2-3 times to ensure repeatability of the data. Hence, a more accurate estimation of the beam conductance is given by the linear slope of the Q vs ΔT curve as the current, I_h, is ramped up. The difference is illustrated in the cartoon below:
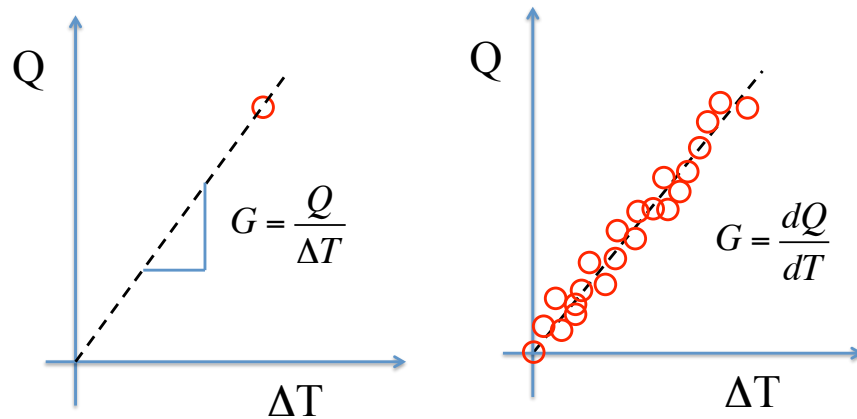
Figure 2A.3 Illustration of the difference in definition of the conductance either by considering (a) a single data-point with a large enough ΔT, or (b) taking the local slope of the heat flux for a variety of temperature gradients across the suspended beam.

Thus, the error bar can be defined by the Root-Mean Squared Error (RMSE) with a 95% confidence interval by fitting the Q vs ΔT curve with a linear plot.

60

As an example, we report the conductance as 60±2.7 nW/K with a 95% confidence interval (R^2 value 0.974), which is an error of 4.5%. For all beams measured, repeated measurements (2-3 times at each gate temperature) account for the error in Temperature Coefficient of Resistivity (TCR) of the Platinum Resistance Thermometers (PRTs), thus reducing the error in measured α_h and α_s down to 4%. Secondly, slowly ramping up the heating current to get ~50 data points per temperature excursion allows for accurate estimation of the beam thermal conductance within 4-5%.

Appendix 2B: Problem of Platinum Surface Diffusion

I've emphasized the importance of increasing the suspended length of the nanowire for thermal measurement in Chapter 2. Another important consideration during the experimental improvement of contact resistance is the diffusion of Platinum during the Pt/C Electron or Ion induced deposition stage. The Focused Electron Beam (henceforth referred to as the FEB) is used predominantly in scenarios where electrical contact to the nanowire is not sought. Typically, a 5kV FEB with beam diameter <10nm is used so that the electrons don't penetrate too deep into the substrate. The surface adsorbed precursor Pt/C composite gas provided by a Gas Injection System (GIS) is dissociated on the surface by the incident primary beam or the secondary or backscattered electrons emitted by the surface. An illustration of the process is shown below:
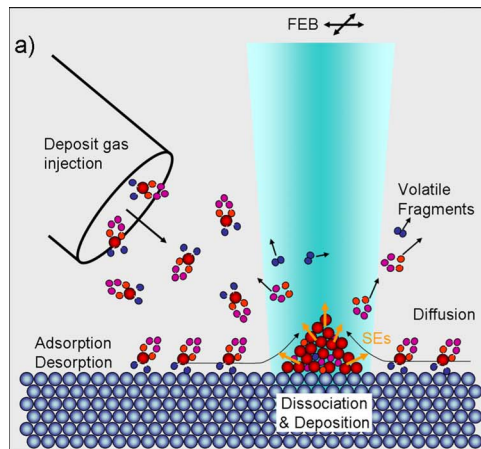
Figure 2B.1 Dissociation of Pt/C precursor on the surface by the incident primary beam as well as emitted secondary and backscattered electrons (Adapted from Utke et. al. [58])

The mechanism of dissociation and deposition using the Focused Ion Beam (henceforth referred to as FIB) is identical, although the electron trajectories are significantly different. Two primary differences are:

(1) Typically the ions in commercial FIBs are Ga^+, which are heavy can easily displace substrate atoms, especially if the substrate atoms are made up of lighter elements. State of the art machines use lighter atoms such as He^+, which potentially can prevent this problem.
(2) Typical energy of the Ion Beam is ~30kV which is larger than that of an electron beam.

Using a FIB always constitutes some degree of etching and amorphization, which is of course material dependent. For example, for our studies of Silicon (Chapter 3) and Bismuth (Chapter 4) nanowires, we used a FEB, which caused negligible damage to the nanowires. However, for our studies of Vanadium Dioxide (Chapter 5) beams, using the FIB allowed us to make electrical contact to the beams and hence measure the electrical

and thermal properties simultaneously. In order to prevent damage to the beams, we used a lower emission current, ~10pA during the patterning of the contacts.

Now, since the precursor gas results from sublimation of the precursor gas, typically upto ~55°C [58], the local temperature at the deposition site can be higher than the nanowire and cause migration of the Pt/C along the nanowire length. Fig 2B.2 illustrates this problem on a Silicon nanowire. Note, the second image in Fig 2B.2(b) was taken after the nanowire broke in the center of the device.
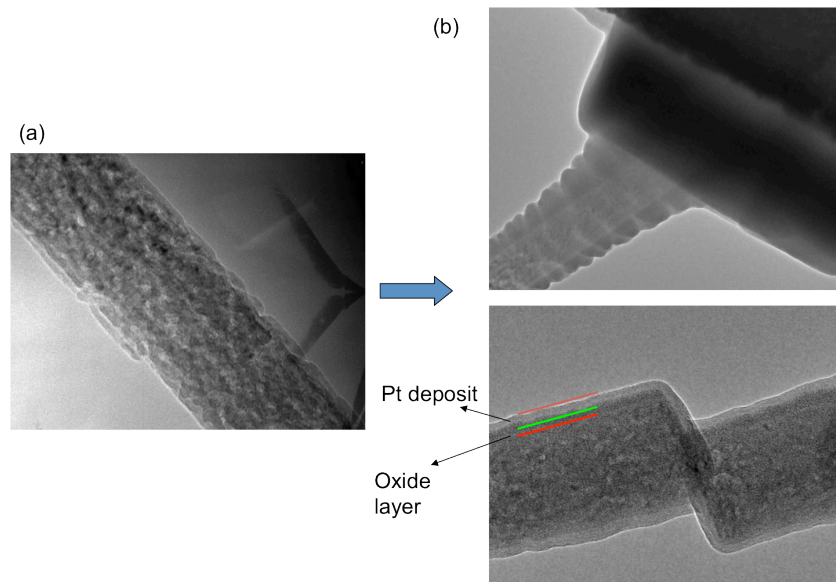
Figure 2B.2 (a) TEM image of the rough SiNW before placing on microfabricated device (b) Platinum deposit imaged with low energy Scanning Transmission Electron Microscopy (STEM @30kV) showing surface diffusion of Platinum along the nanowire length.

This migration of the Platinum depends on two parameters: (1) time of patterning and (2) distance between electrodes on the microfabricated device. A detailed summary is provided by excellent work by Gopal et. al. [70], and we have used a modified bridging technique to make the electrical/thermal contacts. Briefly, patterns were made on either side of the nanowire/nanobeam, which equaled the height of the nanostructure. Then, the two patterns on either side were bridged on top of the nanostructure that was sandwiched in between. The pattern size was chosen carefully such that each patterning time took less than 30 seconds, which minimized the migration along the nanostructure. And most importantly, all the measurements in our work were performed on suspended gaps that were >5μm long. This ensured no thermal/electrical leakage path between the heating and sensing membranes. In summary, by ensuring that

   (1) the suspended portion of the nanowire/nanobeam is 5μm or longer, and
   (2) patterning time is less than 30 seconds for each of the contact pads

we were able to avoid thermal and/or electrical leakage with both the FEB and FIB bonds. This is a crucial step necessary to prevent another source of error in the thermal measurements of nanostructures with our platform.

CHAPTER 3

EFFECT OF MORPHOLOGY ON THE THERMAL CONDUCTIVITY OF SILICON NANOWIRES

Although it has been qualitatively demonstrated that surface roughness can reduce the thermal conductivity of crystalline Si nanowires (SiNWs), the underlying reasons remain unknown and warrant quantitative studies and analysis. In this chapter, we compare the thermal conductivity of vapor-liquid-solid (VLS) grown SiNWs that were controllably roughened to that of Electrolessly Etched (EE) SiNWs. Both sets of nanowires were thoroughly characterized with transmission electron microscopy (TEM) to obtain detailed surface profiles. Once the roughness information (root mean square (rms), σ, correlation length, L and power spectra) was extracted from the surface profile of a specific SiNW, the thermal conductivity of the same SiNW was measured. The thermal conductivity correlated well with the power spectra of surface roughness, which varies as a power law in the 1-100 nm length scale range. These results suggest a new realm of phonon scattering from rough interfaces, which restricts phonon transport below the Casimir limit. Insights gained from this study can help develop a more concrete theoretical understanding of phonon – surface roughness interactions, as well as aid the design of next generation thermoelectric devices.

Authors: Jongwoo Lim*, Kedar Hippalgaonkar*, Sean C. Andrews, Arun Majumdar, Peidong Yang
*equal contribution

3.1 INTRODUCTION

As discussed in Chapter 1, heat transfer in insulators and undoped semiconductors is dominated by phonons, which are quantized lattice vibrations. Phonon occupation follows Bose-Einstein statistics, and they can be treated as particles, especially when using the Boltzmann transport equation to describe phonon scattering and thermal conductivity [25]. In reality, phonons are lattice waves with wave vectors spanning the Brillouin zone, and at any given temperature a broad spectrum of phonon modes is occupied. Planck's law of black body radiation can be used to find the dominant phonon wavelength carrying the heat, $\lambda_d \cong 2\pi\hbar v_s / k_B T$ at a particular temperature using Wien's displacement law $\lambda_d \sim 1nm$ at 300K [9], [25]. The phonon wavelength is an important lengthscale and it has been shown that wavelengths less than 10 nm contribute to 80% of thermal conductivity at room temperature in silicon [71]. The other important length scale is the scattering mean free path, with as much as 35% contribution arising from phonons with mean free paths larger than 1μm [11], [21], [71]. An effective mean free path can be defined for dominant phonons carrying the heat, and is predicted to be ~300 nm at room temperature [33]. Nanostructures smaller than this average mean free path have been shown to limit thermal transport [35], [72].

Recent studies have employed various methods to suppress phonon propagation as a strategy towards realizing efficient and cost-effective thermoelectric devices [36], [49], [65], [73–75]. Chiritescu and Cahill et. al. demonstrated that disordered layers of WSe₂ exhibited dramatically low thermal conductivity due to interface phonon scattering from random stacks of adjacent layers [74], while Kim et. al. [49] were able to reach a thermal conductivity below the 'alloy limit' by embedding ErAs nanoparticles in crystalline In₀.₅₃Ga₀.₄₇As to efficiently scatter a broad range of phonons at the heterogeneous interfaces. While those studies used relatively exotic materials, Joshi et al. showed that even nanostructured bulk (nano–bulk) Si/Ge alloys exhibit reduced thermal conductivity via increased phonon scattering at grain boundaries [75].

Similar to nano-bulk Si/Ge alloys, single-crystalline Si nanowires (SiNWs) have also shown depressed thermal conductivity due to phonon scattering from the nanowire surface. However, unlike previously mentioned systems, all of the factors that can influence phonon propagation have not been quantitatively studied. It has previously been reported by Li et. al. that when the diameter of smooth single-crystal SiNWs that are grown by the vapor-liquid-solid (VLS) process reduces below 150 nm, the thermal conductivity is significantly lower than the bulk value, and can closely follow predictions based by Boltzmann transport theory assuming diffuse boundary scattering as the dominant phonon scattering mechanism [35]. Specifically, the thermal conductivity at 300 K ranges from 40 to 9 W/m-K for SiNWs with diameters of 115 nm to 22 nm, respectively (see Figure 1.15). To help explain this dependence, Mingo et. al. proposed

that despite the smooth surface nature of VLS SiNWs, phonon-surface boundary scattering is diffusive rather than specular [76]. This diameter-limited thermal conductivity based on diffuse phonon scattering at surfaces follows what has been described as the Casimir limit. Although the smooth VLS SiNWs show thermal conductivity reduction, roughened SiNWs produced by electroless etching of Si wafers (EE-SiNWs) were found to produce even lower thermal conductivity, as low as 1.6 W/m-K for a SiNW of 56 nm diameter at 300K (see Figure 1.16) [36]. This surprising result of thermal conductivity below the Casimir limit cannot be explained and warrants more quantitative study.

While the exact mechanism of phonon-roughness scattering is not clearly understood, there have been various attempts at developing theories behind such interactions. One such study by Martin et al. employed the Born approximation toward phonon scattering to explain the large suppression in thermal conductivity [77]. They proposed that the roughness causes an alteration in the phonon dispersion and used perturbation theory to explain the enhanced scattering. Carrete and Mingo et al, however, believe the Born Approximation is invalid at phonon wavelengths similar to the size of the scatterer [78]. Instead, they used an atomic level investigation for 2.2 nm diameter SiNWs with surface disorder to conclude that reducing the thermal conductivity by one order of magnitude is difficult. Using another approach, Moore et al. proposed a backscattering mechanism by using Monte Carlo (MC) simulations of SiNWs with sawtooth structures, but could still not fully explain the large decrease in thermal conductivity [79]. More recent indirect MC simulations by Wang et al. proposed multiple scattering of phonons at the rough surface, while also accounting for impurity scattering, in order to fit their simulation to the experimental data of Hochbaum et. al. [80] However, the random nature of roughness on the EE-SiNWs was not taken into account, which presumably could lead to frequency-dependent scattering from the surface. While these theoretical works shed some light on the dependence of thermal conductivity on rough surfaces, experimental determination of the dependence of thermal conductivity on surface roughness of SiNWs is still lacking [50], [81], [82].

In our work, we introduce a quantitative correlation between thermal conductivity and surface roughness by considering the full length of SiNWs under measurement. Rough silicon nanowires were prepared in three different ways. Firstly, intrinsic VLS-grown SiNWs were etched in a controlled manner to create roughened surfaces. We then characterize the roughness on the roughened SiNWs by Transmission Electron Microscopy (TEM) and statistically extract parameters to quantify the roughness on the surface. We find that root mean square (σ) and correlation length (L) of surface roughness does not individually correlate that well with the thermal conductivity. We introduce in this work a coefficient obtained from power law behavior of the roughness power spectrum at higher frequencies (α_p), which seems to correlate well with thermal conductivity reduction in single crystalline SiNWs.

3.2   NANOWIRE SYNTHESIS AND ROUGHENING

SiNWs having smooth surfaces were grown via the vapor-liquid-solid (VLS) growth mechanism using Au nanoparticles. Briefly, mono-dispersed Au nanoparticles were used as catalysts on a Si(111) wafer. The wafer was heated to 850 ℃ while a mixture of SiCl$_4$ and H$_2$/Ar (1:9) was flown into the system. This synthesis process produced single-crystal Si nanowires with smooth surfaces grown along the <111> direction. More details about SiNW growth and conditions can be found elsewhere [83–86]. After growth, the Si die was immersed in Buffered Hydrofluoric Acid (BHF, Ammonium Fluoride: Hydrofluoric Acid = 5:1), rinsed in Deionized (DI) water, then immersed in KI/I$_2$ solution to remove the Au residue. To induce roughness, two different processes were employed, each showing distinctly unique roughness features, shown in Fig 3.1, which enabled us to study a variety of rough surfaces of SiNWs.
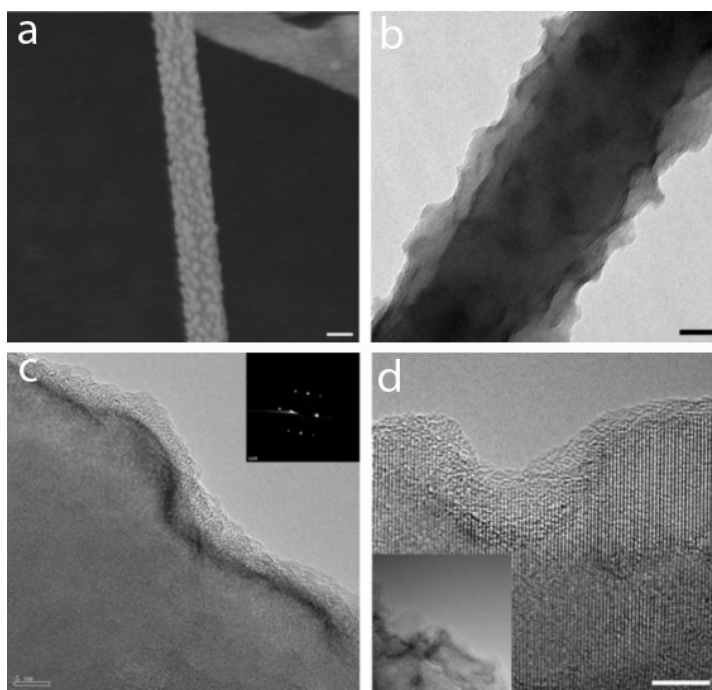
Figure 3.1 (a) SEM image of Si nanowires with Ag nanoparticles on the surface (b) TEM image of Si nanowires after Ag removal in the etching method #1. (c,d) HRTEM image of Si nanowires from etching method #1 and #2, respectively. The inset of (c) is the selective area electron diffraction pattern (SAED). Scale bars for Figure S1 a, b, c, d, are 1μm, 20nm, 1nm, 2nm, respectively. Adapted from Lim et. al. [64]

3.2.1 Surface Roughening Process 1 (VLS nanowires)

Prior to the surface roughening steps, the native oxide on the SiNWs was etched in HF vapor, and the collection of SiNWs was sonicated with DI water. When added to a mixture of AgNO$_3$ (1.74 x10^{-3} M) and HF (3.53 M), the following reactions took place:

The SiNW surface becomes oxidized as a result of a galvanic displacement reaction between Ag^+ ions and Si, which is then subsequently etched by HF. Metallic Ag nanoclusters grow on the surface where the initial reduction of Ag^+ ions took place thereby indicating where Si was etched [85], [86].

$$4Ag^+_{(aq)} + Si_{(s)} + 6F^-_{(aq)} \longrightarrow 4Ag_{(s)} + SiF_6^{2-}_{(aq)} \tag{3.1}$$
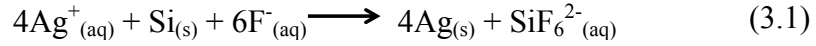
After 2 minutes, the reaction was quenched with excessive amounts of DI water, and then the solution was centrifuged to separate the SiNWs. Once isolated, they were immersed in concentric nitric acid for 30 minutes to remove residual Ag nanoclusters. Suspended SiNWs were retrieved after repeating the centrifuge and rinsing process as seen in Fig 3.1(b) and 3.1(c).

3.2.2 Surface Roughening Process 2 (VLS nanowires)

SiNWs were immersed in a mixture of $AgNO_3$ (1.74 10^{-3} M), HF (3.53 M) and H_2O_2 (5.57 M) solution for 3 minutes. The reaction was followed with a DI water rinse and immersion into concentric nitric acid for residual Ag nanoparticle removal. Since the Ag nanoparticles are abundant and etching occurs only locally around them, the surface of SiNWs in both etching conditions showed a random, rough morphology, as seen in Fig 3.1(d). After treatment, roughened SiNWs were transferred to a TEM grid for surface analysis and physical manipulation.

3.2.3 Surface Roughening Process 3 (Electrolessly Etched nanowires)

The EE wires were made by a similar process used in Hochbaum et. al. [36] and described in detail in Peng et. al. [86] Briefly, (100) oriented silicon wafers with varying starting resistivity levels (0.04 – 10 Ω-cm) were dipped in an aqueous solution of $AgNO_3$ and HF acid. The Ag^+ ions are reduced on the surface forming Ag nanoparticles, while the silicon is oxidized along the edges of the subsequently formed nanowires. This SiO_2 is etched away by the HF acid present in solution, while additional reduction occurs on the top of Ag nanoparticles producing Ag dendrites. The nanowires produced for this study can be up to 100μm long, and the resulting Ag dendritic 'cloud' formed in solution is etched away using a HNO_3 solution for more than a couple of hours.

The roughness along the length of the nanowires was found to be uniform by TEM observation. After the Ag removal step, Ag nanoparticles were found on the edges of some nanowires. Such nanowires were not used for thermal conductivity measurement in case this induced local stresses or additional reduction on the surface, which might result in defected nanowires. The roughness of nanowires from the same wafer undergoing the same etching process was not uniform. Also, the diameter of the nanowires varied from 30–200 nm across the wafer. While selecting the starting wafer resistivity provided some level of control over porosity and RMS roughness, it was found that the roughness of two different wires from the same batch of nanowires could be very different. Tapering along ~10μm of a wire is not significant, but can be a few nanometers at most. Energy

dispersive X-ray spectroscopy (EDS) experiments with a transmission electron microscope (TEM) did not show the existence of residual Ag in the nanowires.

3.3 MORPHOLOGY CHARACTERIZATION

The surface roughness of roughened VLS SiNWs was characterized by Transmission Electron Microscopy (TEM). A series of images at 80,000x magnification were taken along the length of each SiNW and then stitched together, which enabled us to obtain information about the surface roughness along the entire length, as seen in Fig 3.2(a). The diameter is obtained from the TEM images and defined by assuming a circular cross section at each point along the SiNW. Therefore, the average diameter of the entire SiNW is obtained from the average of all the individual cross sections. After TEM characterization, those specific individual SiNWs were manipulated onto pre-fabricated microdevices to measure the thermal transport properties, shown in Fig 3.2(b). As described in detail in Chapter 2, in order to reduce the thermal contact resistance, a Pt/C composite was deposited on both ends of the nanowire using Electron Beam Induced Deposition (EBID) inside a FEI-Strauss Dual Beam FIB. Since only a 2-6 μm long section of the wire bridges the thermal device, only the roughness of that specific active segment between the contacts was considered in all calculations. Additionally, since curvature of even a 2-6 μm segment can affect the roughness measurement, surface profiles were sequentially analyzed along the length in 1 μm segments at a time; see Fig 3.2(c). To remove any marginal curvature effects, a fifth-order polynomial was used to subtract any background curvature. This procedure was insensitive to the order of polynomial chosen, as any polynomial higher than 5 produced the same quantitative result. After background subtraction, the rms and the power spectrum of each 1 μm section was averaged to generate the entire nanowire's rms, σ and power spectrum, *S(q)* respectively, shown below in Fig 3.2(d).
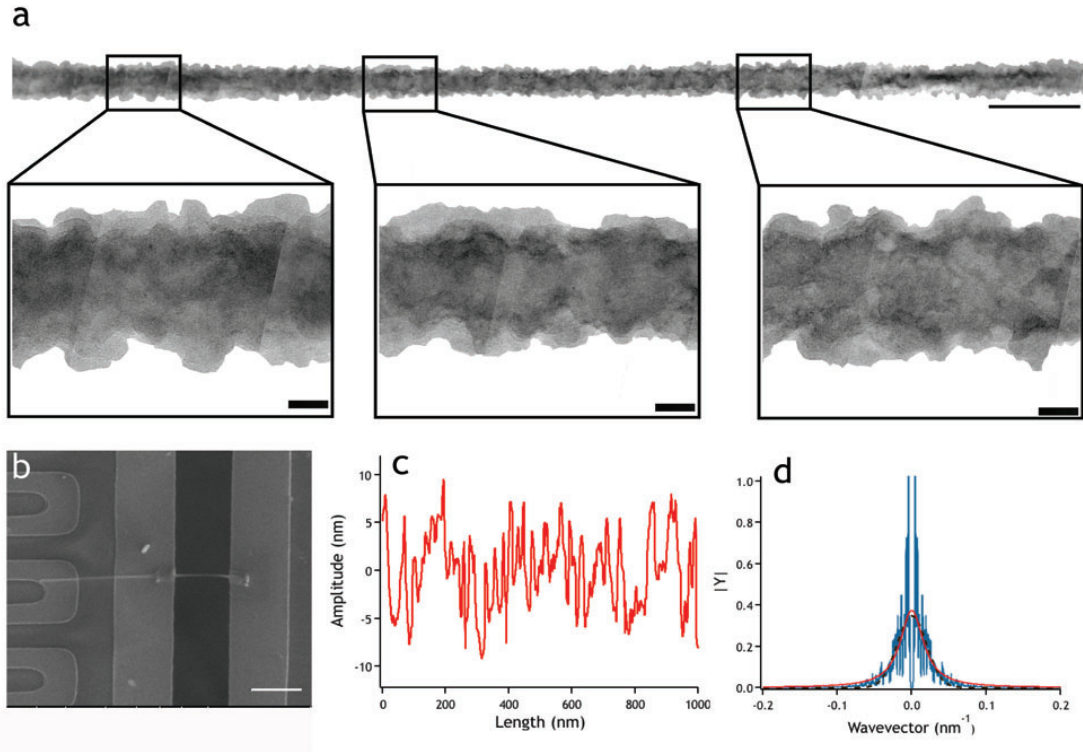
Figure 3.2 Surface roughness characterization. (a) Serial TEM images of Si nanowires along the length with zoom-in images at different position. (b) SEM image of the identical nanowires from (a) on thermal measurement device. The inset is anchored Pt/C composite. (c) Surface profiles from serial TEM images. The length is 1um. (d) Averaged power spectrum from sectioned surface profiles. Red line and dotted line is exponential curve fit and Gaussian curve fit, respectively. Scale bars for panel (a) are 200 nm and 20 nm, panel (b) is 2 μm.

The procedure for the Electrolessly Etched (EE) nanowires is slightly different. While the roughness profiling technique is the same as described above and illustrated in Fig 3.2 (c) and (d), the EE nanowires have other interesting morphology that affects phononic transport. For example, it has previously been shown by selected area electron diffraction (SAED) in a TEM that the EE technique can be used to produce mesoporous silicon nanowires that have a crystalline silicon scaffolding [84]. The porosity for a single step EE procedure can be controlled by the doping level of the original silicon wafer and concentration of the AgNO3 etchant to produce pore sizes varying between 4-16 nm [87]. Such pores are clearly visible by bright field TEM. However, one can imagine that wires with a discontinuous core have a phonon mean free path that is limited not by the diameter of the wire, but the pore-to-pore distance instead. Hence, the diffusive mean free path is less than the overall wire diameter, $\ell_{effective,boundary} < D$. We have established two levels of control to ensure that the nanowires studied in this work are continuous and without pores. Firstly, we grew the nanowires from high resistivity (>4 mΩ-cm) silicon wafers using a mild AgNO3 concentration of 0.0235M, mixed in with 5.39M HF in DI

water solution which is previously known to produce non-porous wires [84], [87]. Secondly, we directly imaged the nanowires before thermal transport with a 200kV FEI Tecnai F20 operated in scanning transmission electron microscopy (STEM) mode and equipped with a high angle annular dark field detector (HAADF). In this mode, a highly convergent electron probe focused to 1-2Å is rastered across the sample, and only the highly scattered transmitted electrons are collected. Image contrast is based on incoherent elastic scattering and varies approximately linearly with thickness and with the atomic number squared (Z^2) of the constituent material [88], [89]. STEM contrast of the single phase Si nanowires is thus capable of estimating the projected thickness of the nanowires, and pores (if they exist) are clearly seen as shown in Fig 3.3(a). Also, highly scattering Ag atoms ($Z = 47$) will appear much brighter compared to the Si ($Z = 14$) nanowires in STEM images providing easy identification of Ag impurities.

We initially measure the cross-sectional area of a non-porous Si nanowire using three-dimensional electron tomography, where the nanoscale 3D shape and surface roughness of the nanowire can be reconstructed from a series of projection images at different viewing angles (see Figure 3.3(b)) [90–92]. The tomogram clearly shows that the wires are non-circular, which reduces the effective phonon mean free path compared to wires with a circular cross-section. A single measurement from the projection image of the same wire shown in the 3D tomogram is shown in Fig 3.3(c) gives a lateral width w of 65 nm. Assuming the wire exhibits a circular cross-section with this diameter, as most other experiments have done previously, the nanowire has an apparent cross-sectional area that is on average 30% larger than the actual average cross-section as measured along 200 nm of the 3D tomogram. Unfortunately, electron tomography is difficult and time consuming to apply to numerous wires, and we instead apply a simpler technique assuming a linear relationship between thickness and STEM intensity normalized by the incident beam current. A comparison between this technique and the tomography results yields a similar cross-sectional area, and is much easier to apply on many wires. Estimations of the cross-sectional area from STEM projection images are generated by integrating the intensity under a line profile across the lateral width of a nanowire. The integrated area is normalized with respect to the total current of the incident electron beam to allow for variations of alignment and instrument performance on different days. Fig 3.3(d) shows the cross-sectional area of a smooth vapor-liquid-solid (VLS) nanowire, which should be nearly circular, used to test our simpler method, and the error was found to be <5%. Further, STEM can be used to identify defects such as necks and junctions, and reject such nanowires from thermal measurements. Finally, the cross-section for measured wires is checked at different points along the length of the suspended nanowire to confirm uniformity along its length.
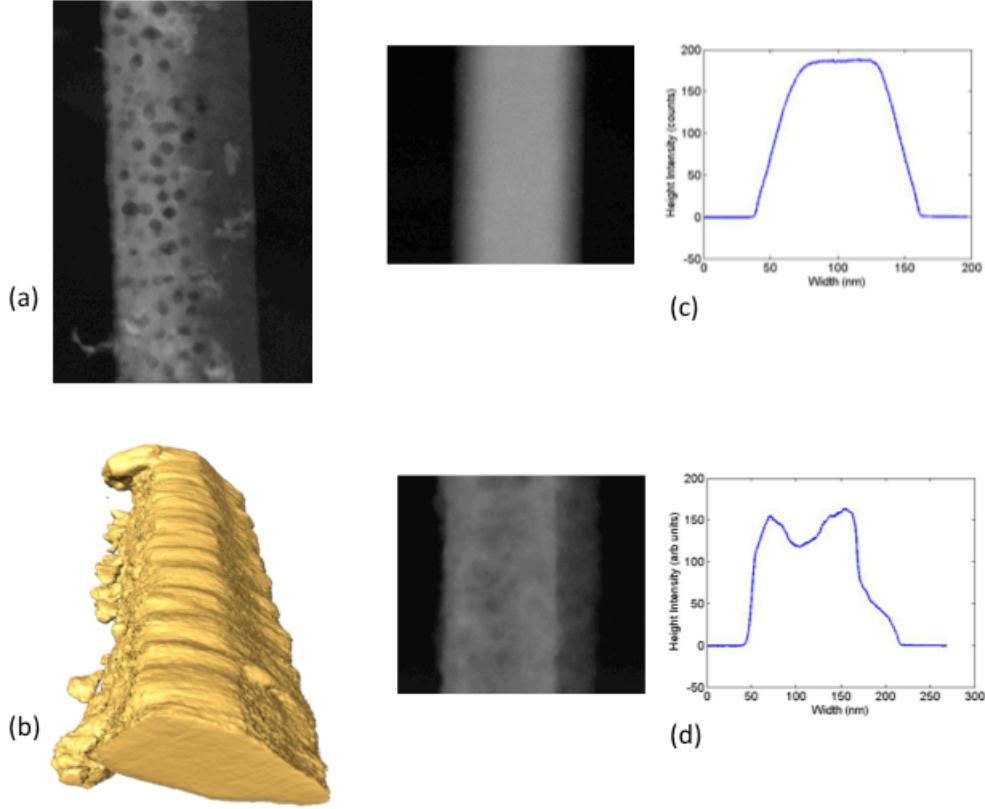
Figure 3.3 Morphology of EE SiNWs (a) Porous nanowire imaged with STEM from a wafer with starting resistivity ρ < 0.03 Ω-cm (b) Three dimensional tomogram showing a non-circular cross-section and roughness along the edges of the nanowire (c) STEM profile for a circular cross-section smooth VLS nanowire (d) STEM profile for a non-circular cross-section EE nanowire.

Martin et. al. postulated based on the Born Approximation [77] that the frequency dependent boundary scattering rate $\tau_{i,j}^{-1}(E)$ can be represented by a surface integral in energy, $S(E')$ where the integral is taken over the area of the surface of constant energy, E' as:

$$\tau_{i,j}^{-1}(E) \propto \int_{E'=E_i} \frac{S(q)}{\nabla_{k'}E'(k')} dS_i(E'), \quad q = k'-k \tag{3.2}$$

Here they considered a phonon with wavevector k from branch i scattering to a phonon with wavevector k' from branch j. Also, $S(q)$ is the Fourier transform of the spatial autocorrelation function, or in other words, the power spectrum, the dilated rough surface that scatters the phonons, which constitutes the perturbed Hamiltonian H' allowing for the transition from the incoming wavevector, k to the scattered wavevector k'. Sadhu and

Sinha, using a wavelike phonon transport approach, considered coherent scattering of phonons from a rough surface, and presented that for modes at frequency ω [93]:

$$\ell_{mn}^{-1}(\omega) \propto \sum_{pq} S(q), q = k_{mn} - k_{pq} \tag{3.3}$$

Where $\ell_{mn}(\omega)$ is the mean attenuation length for those phonons scattering from incident direction k_{mn} to a scattered direction k_{pq} and $S(q)$ is the power spectrum. Thus, in order to understand scattering of phonons from a rough surface, experimental determination of $S(q)$ is crucial . It is common to assume that the autocovariance function of a random rough surface to follow an exponential curve given by $C_E(r)$ as also evidenced in literature shown in Equation (3.4) below [77], [94–97]

$$C_E(r) = \sigma^2 e^{-r/L} \tag{3.4}$$

where $C_E(r)$ is the autocovariance function of the Si surface roughness, $\Delta(r)$ is the extracted surface profile, and σ is the rms value of $\Delta(r)$, L is the correlation length, which is a statistical parameter that determines the decay of the autocovariance and is related to the lateral length scale of the roughness. By convolution theorem, the power spectrum is the Fourier transform of the autocovariance function, yielding a Lorentzian form given by:

$$S_E(q) = 2L\Delta^2 \frac{1}{\left[1 + (2\pi Lq)^2\right]} \tag{3.5}$$

In this study, 1-D power spectrum derived from the Fast Fourier Transform (FFT) was calculated for the surface profile with ordinary wavevectors given by q in units of nm^{-1}. As a first approximation, since previous theoretical work has assumed an exponential autocovariance fit for calculating surface roughness, the Lorentzian defined in Equation (5) is used to extract L from the total power spectrum, $S(q)$ [54], [77], [98].

3.4 THERMAL CONDUCTIVITY

In the first part of this section, we'll focus on individual TEM characterization of the roughness and corresponding thermal conductivity measurements of roughened Vapor Liquid Solid (VLS) nanowires (processes 1 and 2 above). Using the roughness characterization technique shown above, σ and L values from TEM images of four different, individual roughened VLS SiNWs are shown in Fig 3.4 below. Two SiNWs with comparable L (8.9 nm and 8.4 nm) and similar D (77.5 nm and 69.7 nm) are shown in Figures 3.4(a) and 3.4(b), respectively. The TEM images clearly depict the significantly different rms values of the two SiNWs ($\sigma = 2.3$ nm and 4.3 nm), which lead to their correspondingly different thermal conductivities (10.68 W/m-K and 5.09 W/m-K, respectively). In Figures 3.4(c) and 3.4(d), on the other hand, the nanowires have comparable diameters D (78 nm and 70 nm) and σ values (~ 3.3 nm and ~ 2.8 nm) respectively. However, the SiNW in Fig 3.4(d) has roughness with $L \sim 6.4$ nm, which is half the value of that for the SiNW in Fig 3.4(c) ($L \sim 13.1$ nm). A smaller value of L corresponds to roughness features occuring at a shorter length scale, which scatter broadband phonons more effectively [77], [93], [99]. The resulting thermal conductivity at 300 K of the SiNW in Fig 3.4(d) (7.78 W/m-K) is lower than that of the nanowire in Fig 3.4(c) (17.16 W/m-K). This provides evidence towards enhanced phonon-surface scattering in SiNWs with shorter L, as is also evidence in the recent paper by Ghossoub et. al. [100].
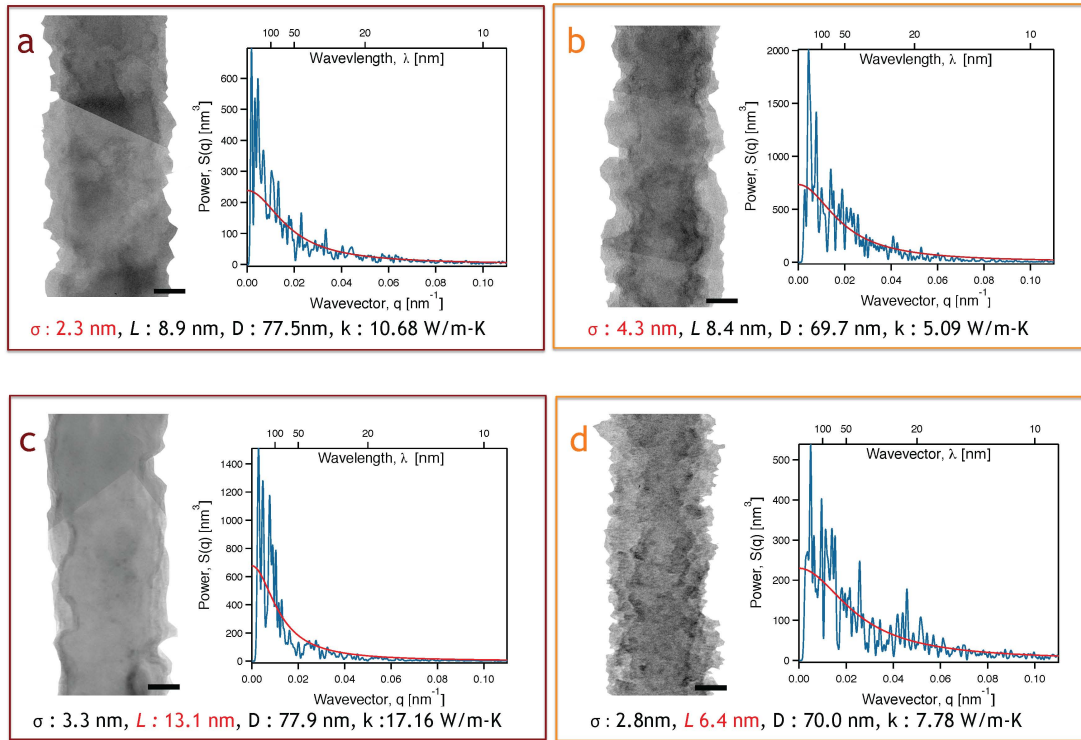
Figure 3.4 Extraction of rms, σ and L from TEM images and their effect on thermal conductivity. (a-b) rms, σ effect on thermal conductivity, (c-d) Correlation length (L) effect on thermal conductivity. All scale bars are 1μm.

The thermal conductivities of these and other roughened VLS SiNWs are plotted as a function of temperature in Fig 3.5. Nanowires with comparable L (8.4 – 8.9 nm) and D (67.9 – 79.8 nm) were selected in Fig 3.5(a), while nanowires with comparable rms (σ = 2.8 – 3.3 nm) and D (70 – 77.9 nm) were chosen in Fig 3.5(b). Clearly, the increase in rms from $\sigma \sim 0$ (as-grown) to 4.3 nm drops the thermal conductivity from 25 W/m-K to 5.09 W/m-K at 300K. Similarly in Fig 3.5(b), as σ remained comparable and L decreased (down to 6.4 nm), a drop in thermal conductivity from 24.63 W/m-K to 7.78 W/m-K was observed. Thus, utilizing the full power spectrum of the roughness profile and looking at the σ and L values, we can predict that rougher wires with higher σ and lower L tend to have a lower thermal conductivity.
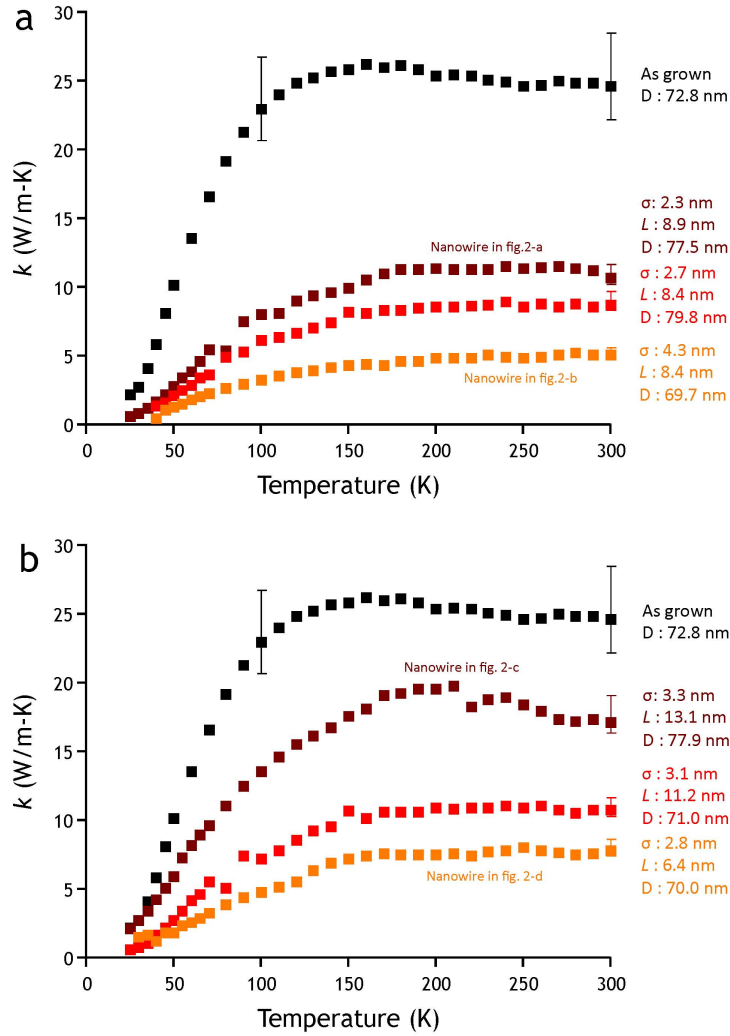
Figure 3.5 Thermal conductivity with temperature as a function of *L* and rms, σ. (a) Thermal conductivity dependence on correlation length *L* with controlled rms, σ and diameter. (b) Thermal conductivity dependence on σ with controlled L and diameter.

However, in order to understand the nature of scattering from the surface of the nanowires, we need to consider phonon wavelengths as well, which previous studies have lacked. In using the kinetic theory for phonons, we can consider that at any temperature, the order of magnitude estimate for a dominant wavelength carrying the heat is given by $\lambda_d \sim 2.9 k_B T / v_g$, where v_g is the average group velocity of the phonons at thermodynamic temperature *T*. At 300K, $\lambda_{dom} \sim 1nm$. However, in reality, there is a large spectrum of phonon wavelengths that contribute to the thermal conductivity. As shown in Figure 3.6(a) [71], a strong spectral dependence of the contribution of phonons to thermal conductivity exists and up to 80% of the thermal conductivity at 300K in bulk Si can arise from phonon wavelengths ranging from 1-100 nm. Using this as a starting point for

analysis and taking a careful look at this wavelength bandwidth of the roughness power spectrum, *S(q)*, it is found that a power law fit captures the power spectrum more accurately (with a least squares fit of >0.9 for all nanowires measured) than a Lorentzian, as shown in Figure 3.6(b). The fit used to then define the roughness is given by:

$$S(q)_{10^{-2} \to 10^0} = \alpha_p \left(\frac{q_0}{q} \right)^n \tag{3.6}$$

where only wavevectors, q of the roughness from 10^{-2} to 10^0 nm^{-1} (1-100 nm) are considered. α_p and n are parameters derived from the fit, and $q_0 = 1/0.313$ nm is the inverse of the lattice constant of Si in the <111> direction. The exponent n is related to the nature of the roughness and is roughly the same for all nanowires measured in this study, and was determined to be $n_{rms} = 2.77$ and $n_{standard\ deviation} = 0.075$. This indicates that the intentional etching of the VLS nanowires described in the earlier section produces a certain type of roughness where the relative amplitudes at different wavelengths or the ratio of amplitudes at different wavelengths, represented by the exponent n, remain roughly the same. On the other hand, α_p is related to the broadband roughness amplitude parameter of the nanowire surface at these relevant wavelengths. We expect a larger α_p for a rougher nanowire. Thus, the thermal conductivity is anticipated to be lower when the value of α_p is higher, while the exact functional dependence is difficult to ascertain.
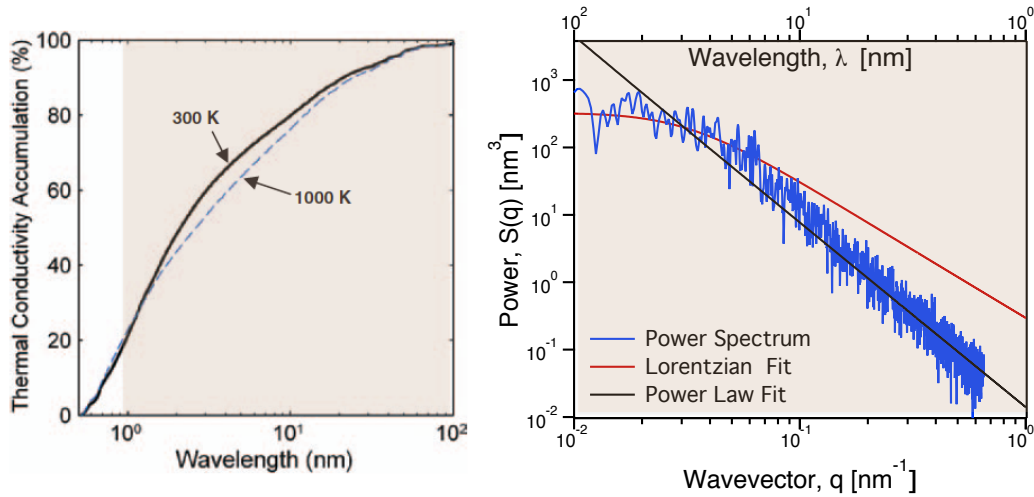
Figure 3.6 (a) Thermal conductivity accumulation as a function of wavelength at 300K and 1000K [71]. Roughly 80% of contribution to thermal conductivity at room temperature comes from phonons with wavelength between 1 and 100nm. (b) Roughness Power Spectrum at the selected length scales (1-100nm). While the actual Power Spectrum is shown in blue, the Lorentzian fit used to extract σ and L is shown in red to be a poor fit at the relevant length scales. The Power Law Fit shown in black captures the roughness better.

In order to better understand the individual roles played by rms, diameter, correlation length, and the high frequency amplitude term, α_p, towards reducing phonon propagation, the room temperature thermal conductivity of SiNWs as a function of different parameters are plotted in Fig 3.7(a-f). Comparing Figures 3.7(a) and 3.7(b), it can clearly be seen that rms exhibits a more pronounced impact on the thermal conductivity than the diameter. This clearly indicates that for rough nanowires rms, rather than diameter (within the range measured), is the major limiter of phonon propagation. Further, as illustrated in Figure 3.7(c), there is no clear dependence of thermal conductivity purely on the correlation length L, which indicates that L by itself doesn't capture the surface roughness accurately. The fact that the rms rather than the diameter has more influence on phonon transport is qualitatively different from the trend observed with smooth SiNWs, where boundary scattering occurs in the diffusive regime [35], [76]. In this diffusive picture, the nanowire surface absorbs all phonons impinging upon it and thermalizes it; then, behaving as a blackbody (to ensure elastic scattering), re-emits the phonons at a rate proportional to the local temperature of the surface. In this new sub-diffusive regime, where the thermal conductivity, k is lower than the Casimir Limit, we first propose a dimensionless roughness correlation factor to define the total roughness, σ/L, which is based upon the following physical intuition: the magnitude of the roughness is (1) proportional to L and (2) inversely proportional to rms at 300K (Fig 3.7(d)). While it is clear that rms and L are the important parameters that define the roughness of the surface, they do not directly represent the roughness parameter that is relevant for phonon

scattering. Therefore, it is not surprising that although there seems to be a better trend of thermal conductivity with σ/L as opposed to that with σ or L individually, the correlation is not very strong and shows scatter.
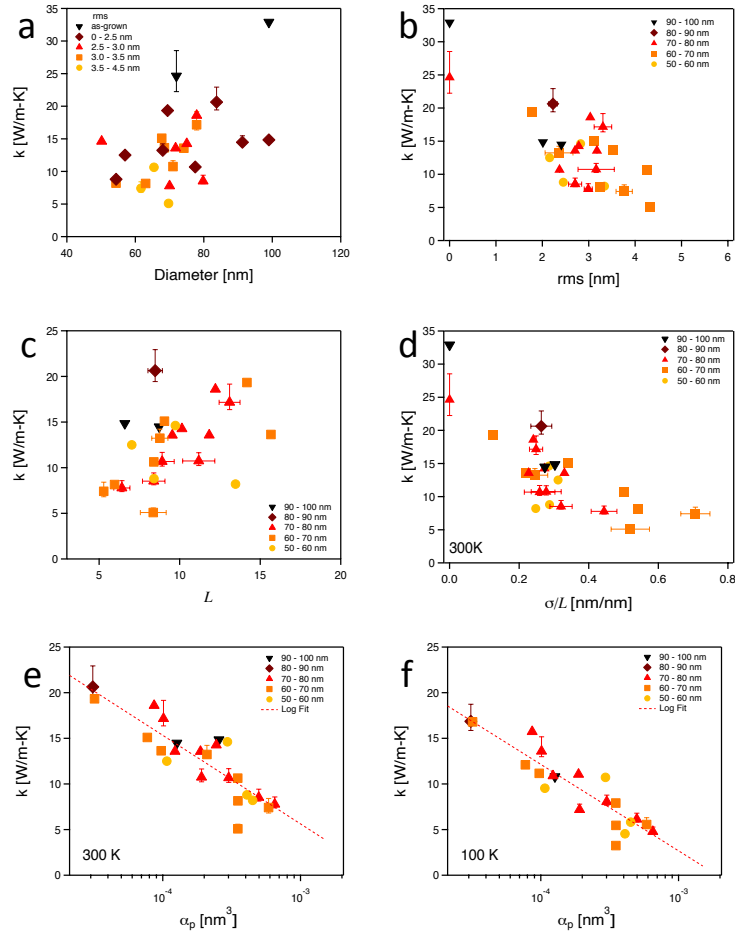
Figure 3.7 Thermal conductivity as a function of three roughness factors (σ, D and L).(a) Thermal conductivity at 300 K as a function of rms with different range of diameter. (b)Thermal conductivity as a function of diameter with different range of rms. (c)Thermal conductivity as a function of diameter with different range of L. (d) Thermal conductivity as a function of σ/L for 300K.Correlation between thermal conductivity and σ/L gets stronger than rms or D only. (d) has a trend similar to REF 8 figure 3a except the discrepancy in L. (e,f) Thermal Conductivity as a function of α_p (plotted on a log scale) at 300 K and 100 K, respectively. As α_p increases, the wires are rougher, with wavelengths in the 1-100nm range and the thermal conductivity drops significantly.

Looking back at Figure 3.6(b) in detail, the Lorentzian fit doesn't capture roughness spectrum at the relevant wavelengths (1-100nm) very well. Also, the roughness length scales that are relevant for phonon scattering are better captured in the power spectrum,

which is represented by two parameters α_p and n. Since n is a constant across all the etched wires, what captures the roughness structure over the relevant phonon scattering band is the parameter α_p. Figure 3.7(e) plots the thermal conductivity as a function of α_p for various wires at 300K, and what is observed is a much better fit. This indicates that directly relating the lateral length scale of the roughness to the wavelength bandwidth of phonons contributing to thermal conductivity is key to understanding the physics of roughness boundary scattering. Figure 3.7(f) plots the thermal conductivity as a function of α_p for the same wires at 100 K, which is a marginally better fit.

Now, we look at the thermal conductivity of rough EE wires. We avoid those that demonstrate porosity, silver particles, defects, and/or necks as characterized with TEM/STEM which might impede phonon transport in a non-controllable fashion. We have plotted the thermal conductivity of 7 different wires as a function of diameter, d, rms, σ and power spectra, α_p in Figures 3.8(a), (b) and (c) respectively. While the rms roughness, σ is sensitive to roughness from the total spectral range of the surface profile, the power spectra is only for a spectral range q=0.01 to 1 nm^{-1}. In order to drive home the observation that phonon scattering physics depends on the roughness, we have also provided a direct comparison with roughened Vapor-Liquid-Solid (VLS) Silicon Nanowires in the figures [64]. As seen in Figure 3.8(a), the thermal conductivity does not depend strongly on the diameter, a trend that was also observed in the roughened VLS NWs. This is the first indication of a possible deviation from diffusive transport of phonons, since the mean free path is not limited by the diameter, but something lesser. While there is a weak dependence of the thermal conductivity on rms roughness for the roughened-VLS wires, the dependence disappears for the EE wires (see Figure 3.8(b)). On the other hand, the dependence of measured thermal conductivity on α_p follows the same trend as that observed for the roughened-VLS nanowires (Figure 3.8(c)). We expect a rougher wire to have a larger value of α_p, and an enhanced rate of scattering of the phonons and hence a lower thermal conductivity.
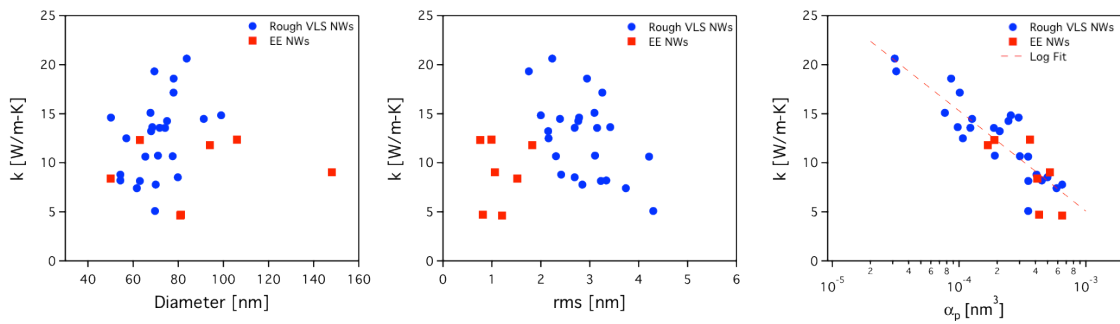
Figure 3.8 Comparison of thermal conductivity of EE SiNWs with rough VLS SiNWs (a) Thermal conductivity as a function of diameter (b) Thermal conductivity as a function of rms roughness (c) Thermal conductivity as a function of α_p, spectral roughness. The EE wires have low rms roughness yet still exhibit low thermal conductivity, demonstrating the importance of the spectral characterization of roughness.

The enhanced scattering of phonons from rough surfaces observed in this study qualitatively follows predictions from earlier theoretical work. Separately, both Alvarez et. al. and Moore et. al. predicted stronger backscattering of phonons at periodically rough surfaces with longer σ and shorter L by using phonon hydrodynamics and Monte Carlo simulations, respectively [79], [101]. However, direct application of this analysis is hindered by the non-uniform roughness profile obtained from the electrochemical etching technique, which may behave differently than the periodic structure. A possibly more applicable theory by Wang et. al. [80] suggested that phonons are localized at the rough surface due to multiple boundary scattering occurrences within a single roughness feature on the surface. They pointed out that thermal conductivity decreases as features becomes sharper, which can be interpreted as a shorter L and higher σ. However, they did not look at the effect of high frequency roughness that may selectively scatters phonons more effectively than the low-frequency ones [80]. Martin et. al. [77]and Santamore et. al. [97] use a perturbative approach due to the change in potential at the surface resulting in enhanced boundary scattering, however it remains to be seen if these claims are valid given the range of correlation lengths and rms we have observed in our work. While their study used a correlation length, L = 6 nm, our observed L varies from 8.6–22.3 nm with rms values range from σ = 1.8 nm to 4.3 nm. Sadhu et. al. and Ghossoub et. al. used a broader range of correlation lengths that fit the power spectrum and used a Green Kubo analysis coupled with the Landauer Formalism to extract attenuation lengths for all phonon modes [93], [100]. Some modes had reduced phonon group velocity in their analysis, which they postulated resulted in a lower thermal conductivity.

However, none of these theoretical studies looked at the wavelength dependent conductivity with scattering from the surface for a selective range of roughness wavelengths. To our best knowledge, our experimental work provides first evidence for frequency dependent phonon scattering from rough surfaces at room temperature. We hypothesize that as high-frequency roughness of the nanowire surface increases, there is enhanced boundary scattering, thus reducing the thermal conductivity significantly. This experimental study warrants further theoretical exploration of scattering of phonons from a rough boundary at specific relevant wavelengths in order to understand the exact correlation between the statistically defined α_p parameter and the thermal conductivity.

Every attempt was made at obtaining the most accurate and certain data possible, but there are, however, limitations to our method of characterizing roughness. First, TEM images are 2-dimensional projections of a 3-dimensional material. Therefore, roughness profiles from the projected surface images neglect hidden roughness features not occurring at the respective edge of the sample. But due to the isotropic nature of the etching process and the large number of samples measured, the determined relations found here are statistically meaningful. Second, the fitting curve to power spectrum is strongly sensitive to low frequency peaks which account for not only rough surface but also the curvature of the SiNWs. Hence, the choice was made to fit a power law to the high frequency section of the Power Spectrum only. Third, since L is calculated using the assumption that the autocovariance of the surface profile is an exponential, the uncertainty of L can be estimated based on the coefficient of determination from a least-squared fit, R^2 when Equation (3.6) is used to fit the original power spectra. Hence, only

the Lorentzian fitting functions where R^2 is larger than a certain value (0.63) are strictly chosen. Despite the relatively large uncertainty in L, as can be seen in Figure 3.7(d), trends of the dependence of thermal conductivity, k with σ/L are clearer than that of thermal conductivity purely with rms. In terms of the power law fit, the choice of frequency limits was informed from A. Henry et. al. [71] and can be significantly temperature dependent [11], [26]. The thermal conductivity strongly correlates with the parameter, α_p, extracted from a power law fit of the roughness power spectrum, which opens up a new way of not only characterizing rough surfaces but also shed some light on the possible physics at work.

In conclusion, we are able to derive three primary results from our careful study of the effect of morphology on the thermal conductivity of silicon nanowires: (1) Irrespective of the roughening chemistry, phonon scattering from rough interfaces to reduce thermal conductivity remains robust. (2) Characterizing the roughness requires paying attention to the dominant wavelength of phonons carrying heat at any particular temperature. Using a power law to characterize the roughness captures roughness at the particular frequencies of interest, indicating a relationship between the wavelength of phonons and the wavelength of the roughness. (3) For EE wires with a lower rms roughness than roughened-VLS wires, the spectral roughness at the range of 1-100nm is critically defined as a power spectra amplitude. As this parameter, α_p is increased for rougher wires, we can see a substantial decrease in thermal conductivity down to 5 W/m-K.

CHAPTER 4

OBSERVATION OF ANISOTROPY IN THERMAL CONDUCTIVITY OF INDIVIDUAL SINGLE-CRYSTALLINE BI NANOWIRES

The thermal conductivity of individual single crystalline Bi nanowires grown by the on-film formation of nanowires (ON-OFF) has been investigated. We observed that the thermal conductivity of single-crystalline Bi nanowires is highly anisotropic. Thermal conductivity of nanowires (diameter ~ 100nm) in the off-axis [$\bar{1}$02] and [110] directions exhibit a difference of ~ 7.0 W/m·K. The thermal conductivity in both growth directions is diameter-dependent which indicates that thermal transport through the individual Bi nanowires is limited by boundary scattering of both electrons and phonons. This huge anisotropy in thermal conductivities of Bi nanowires suggests importance of direction-dependent characterization of charge, thermal transport and thermoelectric properties of Bi nanowire.

Title: Observation of Anisotropy in Thermal Conductivity of Individual Single-Crystalline Bismuth Nanowires

Authors: Jong Wook Roh*, Kedar Hippalgaonkar*, Jin Hee Ham, Renkun Chen, Ming Zhi Li, Peter Ercius, Arun Majumdar, Woochul Kim, and Wooyoung Lee
*equal contribution

4.1 INTRODUCTION

Bismuth (Bi), which is a semimetal with a rhombohedral crystal structure and highly anisotropic Fermi surface [103–105], has attracted great attention due to its unique transport properties such as anisotropic carrier transport [103], bipolar electrical resistivity [106] and low carrier effective masses [107], revealed by earlier research on Seebeck coefficient [108], galvanomagnetic effects [106], de Haas-Van Alphen effects [109], and cyclotron resonance [107], [110]. Furthermore, the electrical measurements on Bi nanowires have thrown light on the semimetal-to-semiconductor transition below a diameter of the Bohr radius of Bi (~50 nm) [111], [112]. However, few direct measurements of thermal conductivity of Bi have been performed illustrating a strong interplay between electrons, holes and phonons as heat carriers. In semimetallic Bi, the electronic contribution was significant to thermal conductance from 100 to 300 K while the phonons contributed almost exclusively to thermal conductance below 50 K [103], [113]. Also, most electrical and thermal transport properties of bulk Bi have been understood in terms of the trigonal (parallel) and three equivalent binary (perpendicular) crystal orientations. This directional dependent behavior not only gives the electrons and holes different effective masses, but also results in a distinction in the speed of sound [114]. Fundamental understanding of the carrier scattering in Bi can be furthered by tailoring the geometries of Bi to impede phonon and electronic carriers, as well as tune the band structure based on quantum confinement effect [111], [112], [115]. In particular, these would be very useful to enhance the power factor ($S^2\sigma$) where S is the Seebeck coefficient and σ is the electrical conductivity and/or decrease the thermal conductivity, κ for thermoelectric applications [115], [116].

The efficiency of thermoelectric devices is quantified by the thermoelectric figure of merit (ZT) of a given material, which is defined as $ZT=S^2\sigma T/\kappa$. Single crystalline Bi nanowires have been of great importance due to the expected quantum confinement effect, which should enhance the power factor without significantly affecting κ [117], [118]. In prior work, it was shown that high-quality single crystalline Bi nanowires grown by the on-film formation of nanowires (OFF-ON) [119] have very large electronic mean free paths ($\lambda_e \sim 1.35$ µm) which are about an order of magnitude higher than bulk [103]. This arises due to a reduction of the Fermi Energy, E_F with diameter of nanowires (d_w) [119]. The mean free path of phonons at 300K is estimated to be about 11−14 nm based on the Dulong-Petit limit and $\ell \sim 3\kappa/(C_v \times v)$, [113] where κ is the measured thermal conductivity of bulk Bi (about 8 − 10 W/m·K), C_v is the volumetric specific heat of bismuth (about 1.2 J/cm^3·K) and v is the speed of sound (~ 1790 m/s). Thus, nanowires of diameters close to the mean free path can effectively scatter both phonons and electrons. So far, only a few studies have been conducted on thermal transport in Bi nanowires. Heremans *et al.* [120] investigated the thermal conductance of Bi nanowires embedded in anodic alumina, e.g., Bi nanowire/alumina template composite. Moore *et al.* [121] studied thermal conductivity of individual Bi nanowires grown by the vapor deposition method. They demonstrated thermal conductivity suppression in Bi nanowires compared with bulk Bi, yet most of their study was performed on polycrystalline Bi

nanowires with the exception of one single crystalline Bi nanowire. Furthermore, it should be noted that the thermal conductivity of bulk Bi is highly anisotropic [103]. In this chapter, we show the first systematic study on the thermal conductivity of individual single crystalline Bi nanowires with various diameters and different crystal orientations, thus throwing some light on the transport mechanism in this prospective high efficiency thermoelectric material.

4.2 NANOWIRE GROWTH AND MEASUREMENT

The OFF-ON, a stress-induced method for growing high-quality single crystalline nanowires, was employed in this work to grow single-crystalline Bi nanowires [119]. Since detailed growth mechanisms are available in Refs. [119] and [122], only a brief explanation is provided here. A Bi thin film was deposited onto a thermally oxidized Si (100) substrate using an ultrahigh vacuum (UHV) radio frequency (RF) sputtering system with a base pressure of 4×10^{-8} Torr. After heat treatment of as-grown Bi thin film at 270 ℃ for 10 hours, Bi nanowires were extruded from the surface of the as-grown Bi film. This spontaneous growth of Bi nanowires is attributed to the substantial atomic diffusion to relax compressive stress on the as-grown Bi film. This originates from the mismatch of thermal expansion coefficient between Bi films and SiO_2/Si substrate during heat treatment as illustrated in Fig 4.1(a). As shown in Fig 4.1(b), Bi nanowires grown by OFF-ON were found to be uniform in diameter with aspect ratios exceeding 1000. A high-resolution transmission electron microscopy (HR-TEM) image and a corresponding selected area electron diffraction (SAED) pattern demonstrate that the Bi nanowires are single-crystalline with a growth direction of [110] and [$\bar{1}$02], as shown in Fig 4.1(c) and 4.1(d), respectively. Based on this method, thermoelectric materials, such as Bi [119], Bi_2Te_3 [122], BiSb, and Bi_2Se_3 nanowires could be produced in single crystalline phase.
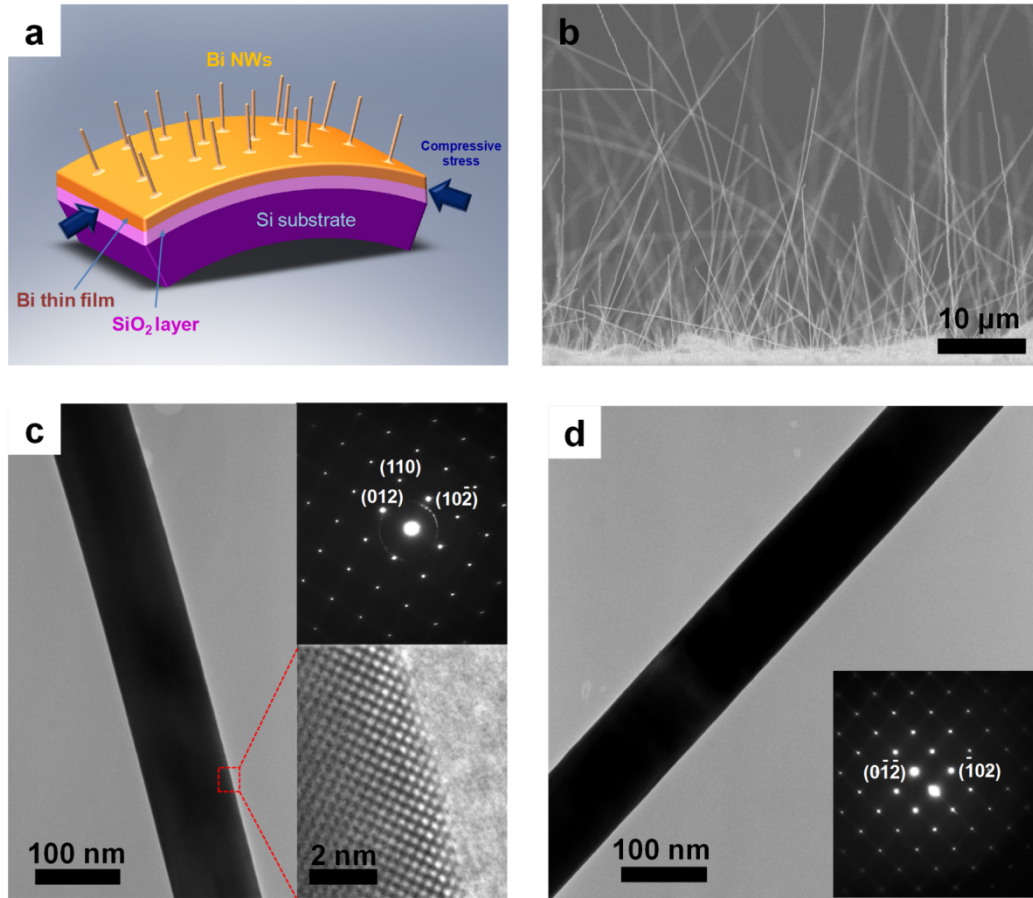
Figure 4.1 Illustration of growth mechanism and structural characteristic of the single-crystalline Bi nanowires. (a) An illustrated representation of the growth mechanism of Bi nanowires using OFF-ON method (b) A SEM image of a side view of as-grown Bi nanowires extruding from the surface of the Bi films. (c) A low-magnification TEM image of a single crystalline Bi nanowires: the SAED pattern (top right) of the nanowire along the [$2\bar{2}1$] zone axis indicates the growth direction of the nanowires is [110], and a high-resolution TEM image (bottom right) of the Bi nanowire shows a perfect single-crystalline material without defects. (d) A low-magnification TEM image of a single crystalline Bi nanowires: the SAED pattern (bottom right) of the nanowire along the [$2\bar{2}1$] zone axis indicates the growth direction of the nanowires is [$\bar{1}02$].

The same suspended platform was employed in measuring the thermal conductivity of individual Bi nanowires. Detailed description of thermal conductivity measurement based on these devices is in Chapter 2. Individual nanowires are placed on the membranes via either manipulation or wet transfer. Bismuth forms a stable oxide layer on exposure to air [105], [112], [121]. The presence of the native oxide layer on the surface of the nanowires and thermal contact resistance between the Bi nanowire and membrane causes an uncertainty in the thermal conductivity measurement. We observe the oxide thickness for the as-grown Bi nanowires as 2–7 nm [119], [123]. For a Bi nanowire with a 5 nm-

thick oxide layer, the thermal conductivity of the nanowire can be underestimated by 6 – 29 % depending on the diameter and length of the nanowires that bridge the membranes. The thermal conduction through the oxide layer was extracted by using similar calculation proposed by Moore *et al.* [121] Thermal contact resistance between the nanowire and the isothermal suspended membrane on either side is another source of error in thermal conductivity measurement. This error has been hypothesized to be as large as 15% in similar measurements on other nanowires [52], [124]. Considering the errors due to the native oxide layer from the outer surface of the nanowires and the thermal contact resistance, the measured thermal conductivity of Bi nanowires were corrected in this work. An illustration of the device after placement of a nanowire and Focused Electron Beam based Pt/C deposition is shown below in Fig 4.2.
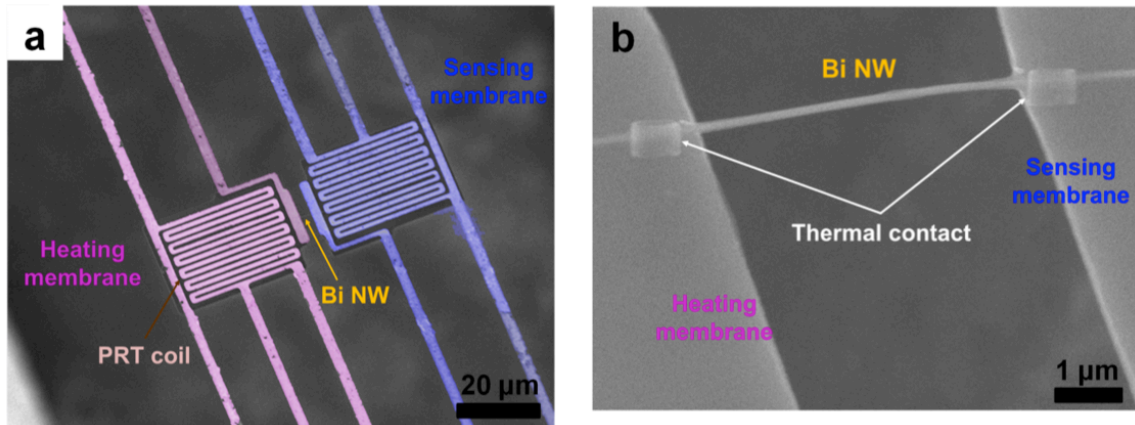
Figure 4.2 (a) A SEM image of the suspended micro-device for measuring the thermal conductivities of the individual Bi nanowires. (b) A SEM image of an individual Bi nanowire placed between the heating membrane and sensing membrane. Pt/C composite thermal contact was locally deposited to improve the thermal conduction between the Bi nanowire and membrane using the electron beam of a dual-beam FIB.

4.3 ANISOTROPIC AND DIAMETER-DEPENDENT THERMAL CONDUCTIVITY OF BISMUTH NANOWIRES

It has been reported that the thermal conductivity of bulk Bi depends highly on the crystal orientation [103]. In order to confirm the growth direction on the thermal-conductivity-measured nanowires, HR-TEM coupled with Selected Area Electron Diffraction (SAED) was employed after the thermal conductivity measurement was completed. Employing this technique, not only could we corroborate that the nanowires retained their high quality single-crystalline cores, but we also determined the growth direction of the nanowires post-measurement. The sample preparation for TEM investigation was performed using the dual-beam FIB system (FEI Quanta 3D FEG). The process for TEM sample preparation is introduced in Figure 4.3. Care was taken to ensure that only nanowires that survived on both the heating and sensing membranes after measurement were considered. However, the yield was low as the wires would break during transfer and/or measurement and hence TEM characterization could not be performed on every measured wire. Thermal conductivity values have only been reported for those wires that survived after measurement.
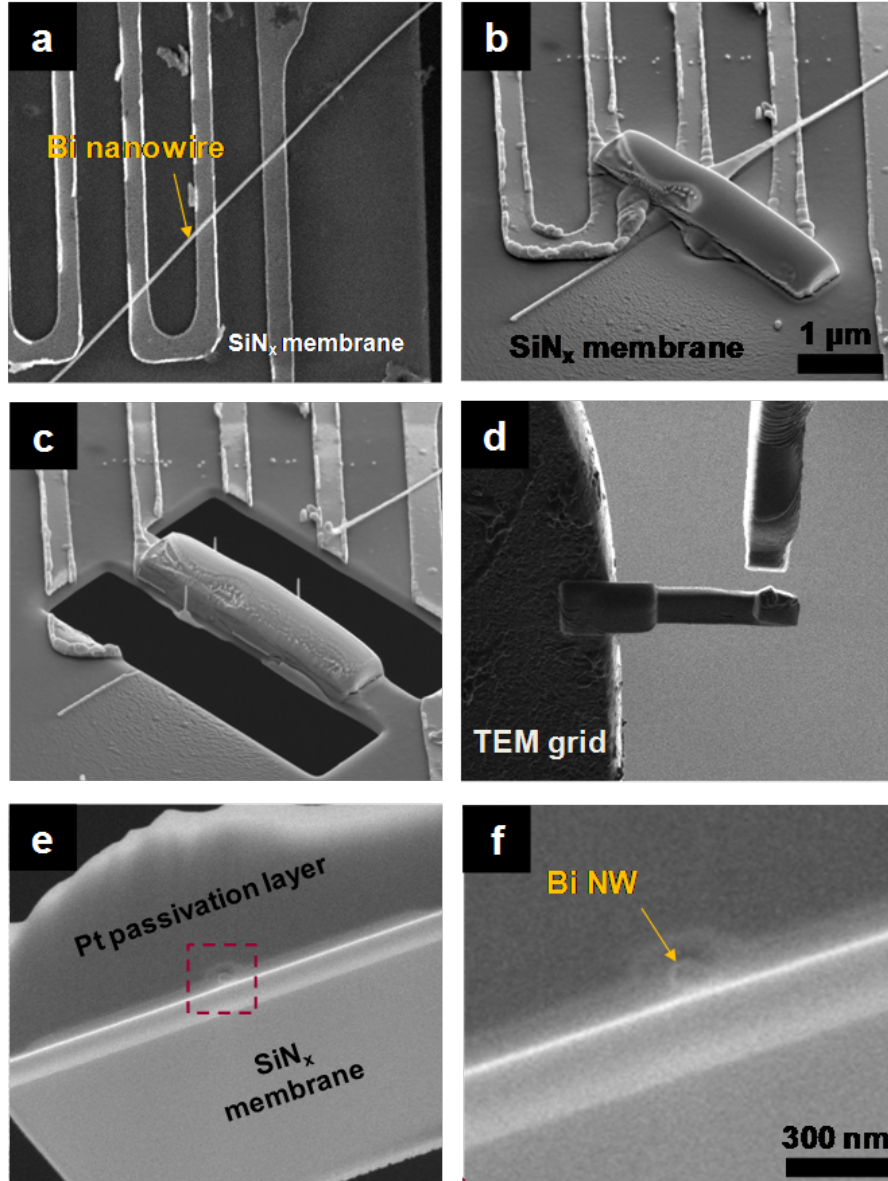
Figure 4.3 The SEM images of sample-preparation process for TEM investigation.
(a) Thermal conductivity-measured Bi nanowire (d_w = 98nm) on the SiN$_x$ membrane. (b)
Deposition of Pt passivation layer using electron beam. (c) Cutting the membrane around
the TEM sample contained κ-measured Bi nanowires. (d) Attachment of TEM sample to TEM
grid using nano-manipulator. (e) and (f) The fabricated TEM sample contains the thermal-
conductivity-measured Bi nanowire.

Figure 4.4(a) shows thermal conductivities of individual Bi nanowires at 300 K with
different diameters, revealing that the measured thermal conductivities have two separate
trends with the diameter of Bi nanowires. From the HR-TEM investigation and the SAED
patterns shown in Fig 4.4(c), the growth direction of NW 1 and NW 2 was found to be

[$\bar{1}$02] while that of NW 3, NW 4 and NW 5 was [110]. This is consistent with the result that as-grown Bi nanowires have two different growth directions of [110] and [$\bar{1}$02] , see reference [119]. The ring pattern in NW 1 and NW 2 could be attributed to the fact that Pt atoms go into surface of Bi nanowire during the process of TEM sample preparation. Gallo *et al*. [103] measured thermal conductivity of single crystal bulk Bi in directions parallel ($\kappa_\parallel$) and perpendicular ($\kappa_\perp$) to the trigonal axis and found anisotropy in the thermal conductivity. For example, at 300K the electronic part dominates thermal conductivity: in the trigonal direction, they measured $\kappa_{\parallel,\text{total}}$ to be 6 W/m·K, with $\kappa_{\parallel,E}$ about 5 W/m·K; in the perpendicular direction, $\kappa_{\perp,total}$ was 10 W/m·K, with $\kappa_{\perp,E}$ about 8 W/m·K. In our case, the nanowire growth directions of [110] and [$\bar{1}$02] are perpendicular and tilted by an angle of 10.85 degrees to the trigonal axis, respectively, as shown in Figure 4.4(b). As shown in the Figure 4a, we also observed the anisotropy in thermal conductivities; the thermal conductivities of Bi nanowires with growth direction of [110] are about four-fold lower than those of Bi nanowires with growth direction [$\bar{1}$02]. We also included in Fig 4.4(a), the thermal conductivity of single crystalline Bi nanowire measured by Moore *et al*. [121] for reference. The orientation of their Bi nanowire is ⟨1$\bar{2}$0⟩ which is also perpendicular to the trigonal axis, but is different from our growth direction. Further, it can be observed that for a particular growth direction, the thermal conductivity of Bi nanowires decreases with diameter at 300 K [125]. This diameter-dependent thermal conductivity of Bi nanowires suggests that there is enhanced boundary scattering of heat carriers, which are both electrons and phonons.
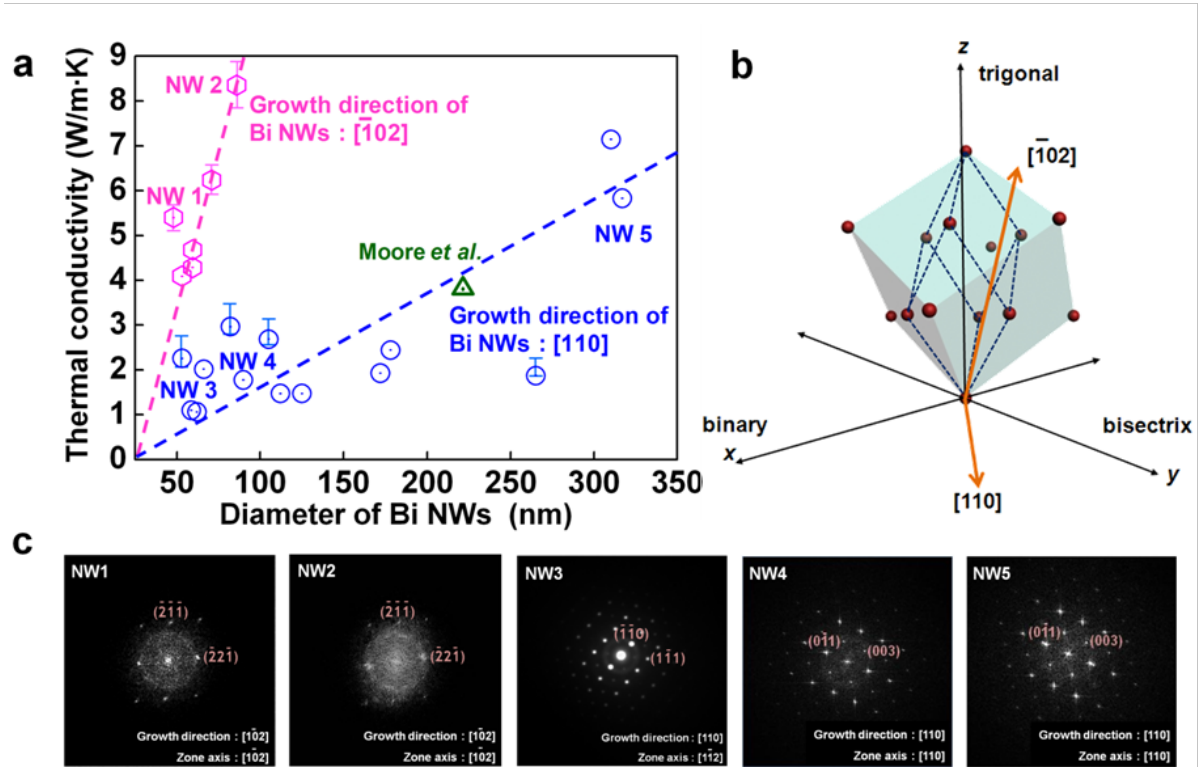
Figure 4.4 (a) Diameter-dependent thermal conductivity of Bi nanowires with different growth direction of [$\bar{1}$02] (pink hexagon) and [110] (blue circle), respectively, at 300 K. The dashed lines represent the linear fit of the measured thermal conductivity for each growth direction of Bi nanowires. The thermal conductivity (green triangle) of Bi nanowire perpendicular to the trigonal axis measured by Moore *et al.* is taken from Ref. [121]. (b)An illustrated representation of the growth direction of Bi nanowires grown by OFF-ON. (c)The SAED patterns of the thermal conductivity-measured Bi nanowires. While the ED pattern shows NW 1 and NW 2 was grown along the direction of is [$\bar{1}$02], NW 3, NW 4, and NW 5 was grown along the direction of [110].

In bulk Bi, the thermal conductivity along the trigonal direction is much lower than that perpendicular to the trigonal direction and deviation in thermal conductivities in the two direction is only around 2 W/m·K at 300 K. In contrast, the deviation between [$\bar{1}$02] and [110] directions is around 7.0 W/m·K at 300 K for 100 nm diameter nanowires. Also, the thermal conductivity in Bi nanowires showed opposite trend compared with that in bulk, such as the thermal conductivity along [$\bar{1}$02], *i.e.*, 10.85 degrees from the trigonal direction, is higher than that along [110], *i.e.*, perpendicular to trigonal direction. This may be due to either of the following reasons; (i) There is no report on any transport property, let alone thermal conductivity of Bi in this off-axis, *i.e.*, [$\bar{1}$02], direction. From the crystallographic point of view, a tilt of 10.85 degrees from the trigonal direction would cause a considerable difference in transport properties. For example, the nearest atom spacing in the [$\bar{1}$02] direction in Bismuth is ~ 24 Å, while that in the trigonal or [001] direction is ~ 5.7 Å. We speculate that this could result in a significant difference in

the mobility (due to band effective mass), Fermi vector, k_F and phonon group velocity. (ii) The electron mobility of Bi nanowires in the trigonal [001] direction was observed to be a factor of around four times higher than that in the bulk Bi [119]. This enhanced mobility may be caused by the variation in electronic band structure due to the interface between the surface oxide and the Bi cores [126–128] or the reduced Fermi wavevector [119]. Also, Huber *et al.* [129] studied contribution of surface states to electronic conductivity in sub-50nm single crystalline Bi nanowire array in the trigonal direction and they observed that the surface electrons possess high mobility. The enhanced mobility could result in the increased electronic thermal conductivity. However, there is no report on mobility of [$\bar{1}$02] or [110] wires. Detailed experimental study of thermal conductivity as a function of magnetic field would be an exciting direction of proposed research. Also, in terms of the lattice thermal conductivity, there is a theoretical report that [130] a good bulk thermal conductor may not necessarily be a good thermal conductor for nanowires due to alternate contributions to phonon scattering [110]. In any cases, more experimental data would resolve this issue.

For the Bi nanowires grown along the direction of [110] with d_w = 117 nm, the corrected thermal conductivity was 2.7 ± 0.1 W/m·K at room temperature, which is higher than the electronic thermal conductivity, κ_E of ~ 2.5 W/m·K calculated from the Wiedemann-Franz law using our recently reported electrical conductivity of Bi nanowires with similar diameters [111]. However, for the Bi nanowires grown along the direction of [110] with d_w = 69 nm, the thermal conductivity is as low as 1.1 ± 0.2 W/m·K, which is lower than the κ_E of 1.6 W/m·K estimated from the Wiedemann-Franz law and electrical conductivity of Bi nanowires with similar diameters. Including the inaccurate estimation of diameter due to the native oxide and inevitable thermal contact resistance, the lower values of thermal conductivity could have large errors associated with them. Hence, the variability in the diameter trend should be taken as an additional source of error due to these uncertainties in the thermal conductivity measurement. In spite of considering this uncertainty in the thermal conductivity measurement, our result clearly shows the anisotropy and diameter-dependence of thermal conductivity in Bi nanowires for the first time. Gallo *et. al.* [103] showed that the total electronic contribution of thermal conductivity, κ_E for a semi-metal such as Bi can be expressed as $\kappa_E = \kappa_e + \kappa_h + \kappa_{he}$ where (1) κ_e is the ordinary thermal conductivity due to electrons only, (2) κ_h is the ordinary thermal conductivity due to holes only and (3) κ_{he} is the thermal conductivity arising from bipolar diffusion due to the formation of electron-hole pairs. In this breakup, the electrons still dominate and the high electron mobility direction in bulk Bi corresponds to the low lattice thermal conductivity direction (both parallel to the trigonal axis). Using the electrical conductivity of a Bi nanowire with d_w= 127 nm [111], the electronic thermal conductivity at room temperature can be estimated to be ~ 1.9 – 2.5 W/m·K (assuming $L_{\parallel}$=2.3×10^{-8} W.Ω/K^2 and $L_{\perp}$=3.0×10^{-8} W·Ω/K^2), although the growth direction of the nanowire was not known. In both cases, electronic contribution to the total thermal conductivity can be as high as 70 % of the total measured thermal conductivity. Thus, both anisotropy and boundary scattering have significant effects on the transport of the heat carriers (electrons, holes as well as phonons) in the nanowires, but their exact

mechanism is not clear. This finding motivates further thermal and electrical study on Bi nanowires with different crystal orientation.

4.4 TEMPERATURE DEPENDENCE OF THERMAL CONDUCTIVITY FOR BISMUTH NANOWIRES

Fig 4.5 shows temperature dependence of thermal conductivity for NW 1, NW 4, NW 5 and a Bi nanowire with d_w = 115 nm in the temperature range 40 – 300 K. The growth direction was confirmed to be [$\bar{1}$02], [110], and [110] for NW 1, 4, and 5 respectively, and is hypothesized to be [110] for the Bi nanowire with d_w = 115 nm based on the anisotropic dependence of κ shown in Fig 4.4(a). The diameters of NW1, NW 4, and NW 5 were 58 nm, 98 nm, and 327 nm, respectively. As shown in Fig 4.5, the thermal conductivities of the Bi nanowires increase monotonically with increasing temperature, but the actual temperature dependent behaviors are quite different: NW1 shows a slight increase in κ for T < 200 K but a much sharper one for T > 200 K; NW 4, on the other hand, shows a fairly weak temperature dependence for the entire temperature range. For comparison, the thermal conductivity of bulk Bi (inset of Fig 4.5) has a sharp peak at the temperature of 4 K, [103] presumably where phonon-phonon *Umklapp* scattering takes over, because phonon is the dominant heat carrier at low temperatures (< 200 K) [120], and the Debye temperature of Bi (120 K) [131] is low. The fact that our measured κ monotonically increases with temperature from 40 – 300 K suggests that boundary scattering is significant for both electrons within the entire temperature range and phonons at lower temperature (T < ~ 200 K), as explained below. At higher temperature, electronic contribution dominates the total thermal conductivity and the lattice contribution is relatively small (< 30 %). Also, the estimated mean free path of phonons is about 11 – 15 nm at 300 K; the effect of the boundary on phonon conductivity at this temperature is not significant. However, at lower temperatures the lattice contribution is dominant and the mean free paths are longer, hence the boundary can scatter phonons more effectively. For instance, below 200 K, lattice contribution is larger than 50 % of overall conductivity in bulk Bi and the boundary could affect the phonon mean free path substantially. Thus, one would expect the lattice contribution of a nanowire with a particular diameter to be a constant with temperature due to the boundary scattering since the lattice specific heat above the Debye temperature and the speed of sound are constant.
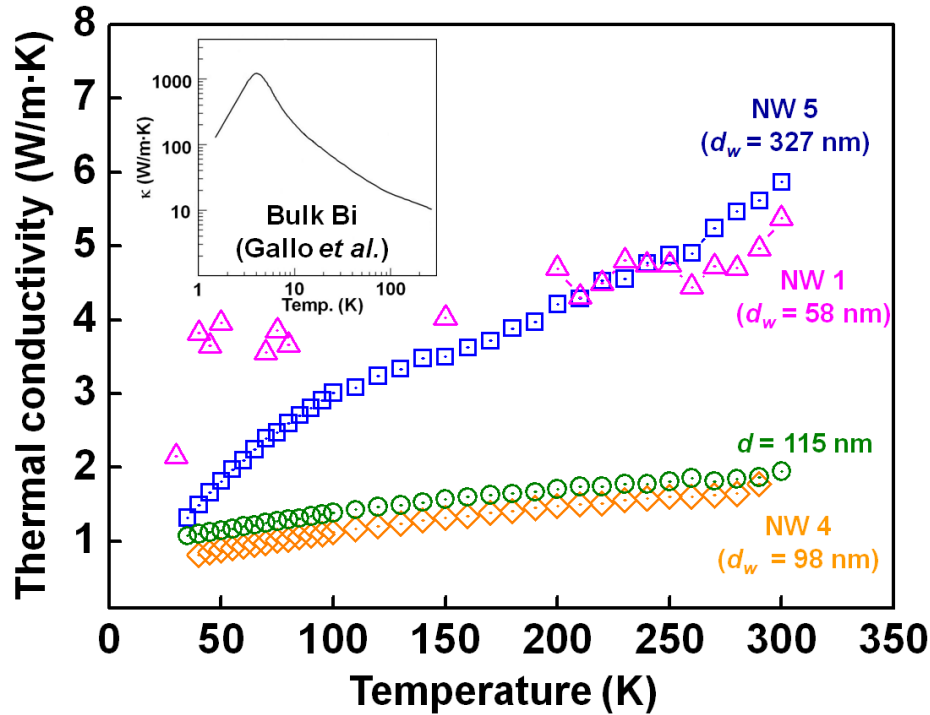
Figure 4.5 The temperature-dependent thermal conductivities of Bi nanowires with d_w = 58 nm, 98 nm, 115 nm, and 327 nm. The inset shows the temperature-dependent thermal conductivity of bulk Bi (Ref. [103]).

The electronic contribution to the total thermal conductivity can be estimated from the modified Wiedemann-Franz law as discussed earlier. However, as an additional variable in the case of Bi nanowires, it has been predicted and experimentally verified [105], [107], [118], [125] that there is a semi-metallic to semiconducting transition when the diameter of nanowire is smaller than a certain transitional diameter. According to our electrical measurements of Bi nanowires, the transitional diameter occurs near 63 nm [111], hence NW1 should be semiconducting. For semiconducting wires, electrical conductivity, σ, increases significantly with temperature at $T > 200$ K, while it is almost flat below 200 K. Thus, below 200K, the interplay between the almost constant phonon contribution and increasing electronic contribution gives weakly linear temperature dependence for NW1. Higher than 200 K, the electronic contribution takes over and the temperature dependence is stronger. For the nanowires on the semi-metallic side of the transition (NWs 4, 5 and the 115nm NW), there is an overall linear temperature dependence due to the constant lattice contribution and an increasing electronic contribution. Therefore, we can attribute the temperature dependence of thermal conductivity to the strong boundary scattering for both electrons and phonons, which is consistent with the observed trend of diameter-dependence for thermal conductivity. The details of the temperature dependence, however, can vary for wires with different diameters and crystallographic orientations, and merits further investigation, such as

concurrent electrical and thermal measurements with quantitative modeling coupled with similar anisotropic considerations as we have done in this work.

4.5 CONCLUSION

In summary, we observed the anisotropy in thermal conductivity of single crystal Bi nanowires grown by OFF-ON method. The orientation dependent thermal conductivity of Bi nanowires was analyzed by HR-TEM and SAED investigations for thermal conductivity-measured Bi nanowires. The thermal conductivity of the Bi nanowires with growth direction of [110], which is perpendicular to the trigonal axis, is about four-fold lower than that of the Bi nanowires with growth direction of [$\bar{1}$02], which is 10.85 degrees off to the trigonal axis. For a particular growth direction, the thermal conductivity of Bi nanowires scales down with diameter, which indicates the presence of strong boundary scattering of the heat carriers. Our results demonstrate that the growth direction plays a very significant role in charge and energy transport in Bi nanowires, which should be considered when designing thermoelectric devices based on Bi nanowires. Concurrent measurements of both thermal and electrical properties are required to further elucidate the behavior of heat carriers in these high quality single crystalline Bi nanowires.

CHAPTER 5

TEMPERATURE GATED THERMAL RECTIFIER

Heat flow control is essential for widespread applications of heating, cooling, energy conversion and utilization. Here we demonstrate the first observation of temperature-gated thermal rectification in vanadium dioxide beams, in which an environment temperature actively modulates asymmetric heat flow. In this three terminal device, there are two switchable states, which can be accessed by global heating: "Rectifier" state and "Resistor" state. In the "Rectifier" state, up to 22% thermal rectification is observed. In the "Resistor" state, the thermal rectification is significantly suppressed (below 4%). This temperature-gated rectifier can have substantial implications ranging from autonomous thermal management of micro/nanoscale devices to thermal energy conversion and storage.

5.1 INTRODUCTION

Heat and charge transport in condensed matter were first characterized about two centuries ago by the well-known Fourier's [132] and Ohm's [133] laws, respectively. The history of how the science of heat and charge transport has evolved, however, is very different. The discovery and purification of semiconductors, and the use of quantum mechanics to understand their electronic band structure led to the invention of many electronic devices such as diodes and transistors to control and manipulate charge transport. Such devices have been widely deployed, and have touched almost all aspects of modern life in what we now call the information revolution. Heat transport in condensed matter, in stark contrast, has remained in the realm of the Fourier law and its manipulation has been largely absent. Yet, about 90 percent of the world's energy utilization occurs through heating and cooling, making it one of the most critical aspects of any modern economy [134]. Hence, the ability to manipulate heat transport in ways akin to that for charge transport could potentially significantly impact utilization of energy resources.

In condensed matter, heat is usually carried either by phonons or electrons. Metals are generally good conductors of heat through electrons. Manipulating heat in non-metals requires tuning of quantized lattice vibrations or phonons. A few theoretical proposals have been made envisioning tunability of heat flow in solid-state devices [135], [136] and electrically tuned solid-state thermal memory has recently been experimentally realized [137]. Perhaps the simplest manipulation of heat conduction is using a thermal rectifier [138], [139], in which the system thermal conductance depends on the direction of thermal gradient. The level of thermal rectification is commonly [138] defined as the following:

$$R = \frac{G_H - G_L}{G_L} \tag{5.1}$$

Here G_H and G_L are the thermal conductances of the sample in the directions of higher and lower heat flows under the same temperature difference, respectively. Several approaches have been theorized for achieving thermal rectification, such as using materials with opposite trends in thermal conductivity as a function of temperature [140], or asymmetrical phonon density of states in graphene nanoribbons [141]. The interplay between electrons and phonons can potentially have an asymmetry when the direction of flow is reversed.

The rapid advancement of nanofabrication has enabled the synthesis of nanostructures with a variety of materials for both novel applications[36], [65], [142–144] and to explore condensed matter science [145]. Specifically, individual carbon or boron nitride nanotubes with asymmetric mass loading were reported to have thermal rectification of about 2-7% [138]. However, there has been no further experimental advancement since then.

Here we demonstrate the first temperature-gated thermal rectifier devices using VO_2 beams. Thermal rectification in the beams can be switched on and off by changing the device temperature. Unprecedented thermal rectification up to 22% is observed below 340 K. Once the devices are heated above 340 K, they can be switched off, where thermal rectification is greatly suppressed (<4%). A visual representation of the device functionality is shown below in Fig 5.1.
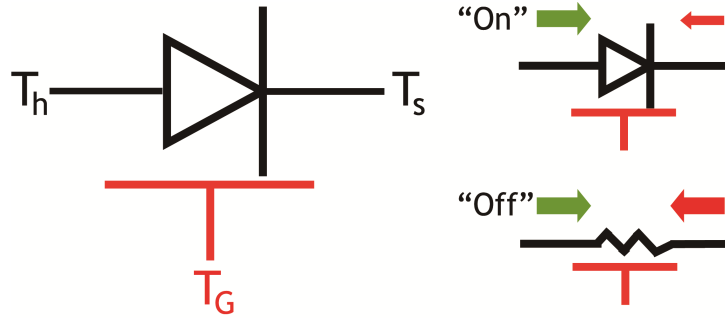
Figure 5.1 Symbolic diagram of temperature-gated thermal rectifier. In the "Rectification" or "on" state, thermal flow depends on the direction of applied thermal gradient, representing strong thermal rectification. In the "Resistor" or "off" state, thermal flow does not depend on the sign of thermal gradient, essentially the behavior of a resistor. The on/off state can be controlled by a global temperature (T_G)

5.2   MATERIAL CHOICE AND CHARACTERIZATION

Vanadium Dioxide is a correlated electron material system that undergoes an insulator-metal phase transition at ~68°C. This is coupled with a structural phase transition at the same temperature, where the insulating monoclinic phase gives way to a metallic rutile phase. The phase transition is known to be first-order and occurs abruptly at the transition temperature, and can also be visualized under an optical microscope as the metallic and insulating phases exhibit different contrast. The structural phase transition in the lattice structure is shown below in Fig 5.2.

(a)   (b)

<340K

Monoclinic Phase (Insulating)

>340K

Rutile Phase (Metallic)
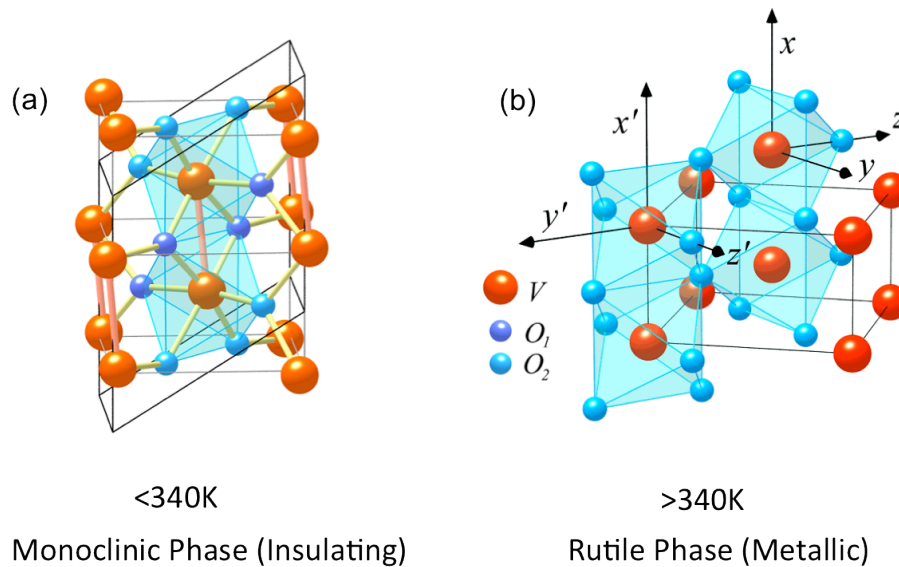
Figure 5.2 Structural phase transition of VO_2 at the transition temperature from the (a) Insulating to the (b) Metallic phase. Under no stress, this transition happens at ~68°C, i.e., 340K, and the Vanadium bond angles change from a monoclinic to a rutile lattice structure.

Single crystalline VO_2 beams have been investigated extensively as a unique platform for studying Mott metal-insulator transitions which can be induced not only by temperature, but also by strain and light [146–150]. Thin films of polycrystalline VO_2 have shown that the insulator to metal transition occurs via nucleation of isolated nanoscale puddles of metallic phases in a background of the insulator phase, which then grow and merge as the transition progresses [151]. In addition, it has been found that the V_nO_{2n-1} family has a large range of transition temperatures (from 135K in V_5O_9, to 340K in VO_2) [152]. Therefore, a mixed phase of different members of V_nO_{2n-1} family can cause the co-existence of a large number of metal-insulator interfaces over a wide temperature range (135K to 340K). Once the temperature is above 340K, or below 135K, these interfaces vanish. The thermal conductivity of poly-crystalline stoichiometric VO_2 films was studied close to ~340K and increased by as much as 60% due to the insulator to metal phase transition [62]. The VO_2 beams used in this study were synthesized using a modified vapor transport method [153], and carefully examined by electrical transport and Raman spectroscopy (see Fig 5.3 below). Bulk VO_2 powder was placed in a quartz boat in the center of a horizontal tube furnace. The typical growth temperature was 1000 ºC with Ar used as the carrier gas. The VO_2 beams were collected on a Si substrate with a 500nm thick thermally grown surface oxide downstream from the source boat. The catalyst, which determines the size of the beam, can be partially diffused away by tuning the pressure and temperature to induce tapered or asymmetrical beam growth. The Raman Spectrograph taken at room temperature shows peaks corresponding to crystal symmetries of the monoclinic insulating phase.
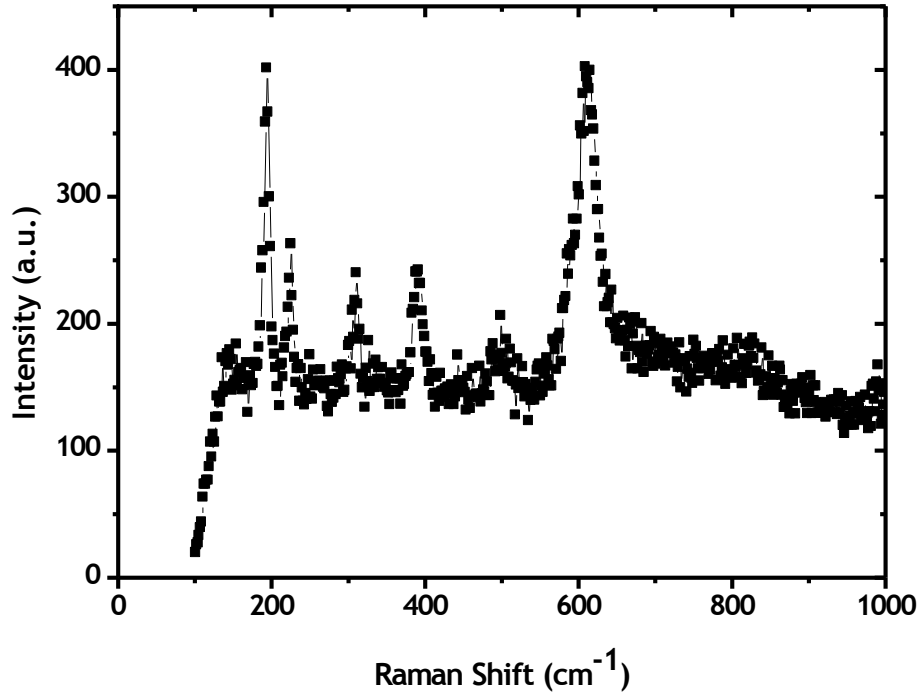
Figure 5.3 Raman spectrum of a uniform VO$_2$ beam at 300K. Raman peaks at 199, 225, 305, 392, 500 and 618 cm^{-1} correspond to A$_g$ symmetry.

5.3   MEASUREMENT OF THERMAL RECTIFICATION

The strength of our measurement platform described in detail in Chapter 2 allows us to then measure directional thermal transport through a suspended VO$_2$ beam in two different directions. Then, Equation (5.1) can be used to determine the rectification for a single beam. In order to do this, an individual 3-5 μm long VO$_2$ beam is transferred to the silicon-based microdevice so as to form a bridge between two parallel, suspended SiN$_X$ membranes, each consisting of micro-fabricated symmetric resistive Pt coils, for thermal and electrical transport measurements [52] (Fig 5.4(a)). The Pt coils are used as both heaters and resistive thermometers. To make good electrical and thermal contact, a Pt/C composite was deposited symmetrically on both ends using a Focused Ion Beam. Therefore, both thermal conductance and electrical conductance can be measured at the same temperature. A resistive heater is used to heat the whole Si chip uniformly inside a cryostat to control the global device temperature, T_G. Again, the measurement is performed in a cryostat at ~2 μTorr to prevent conduction and convection losses.
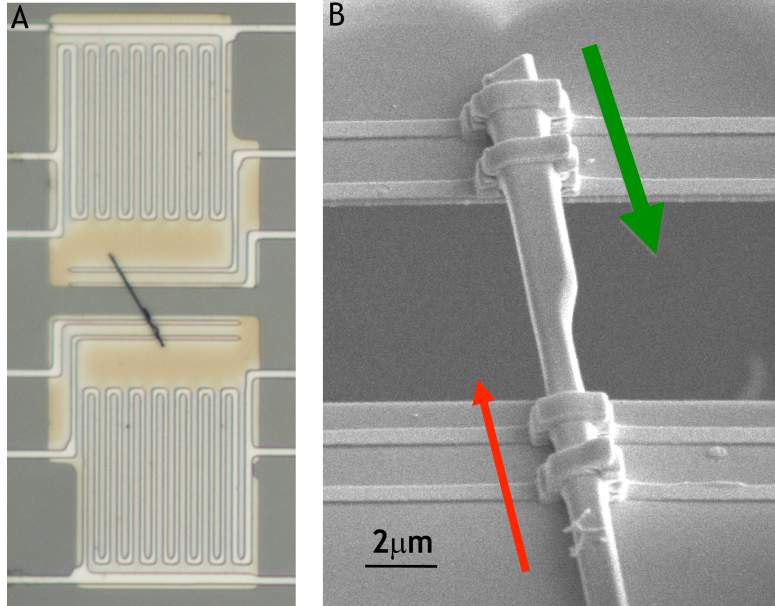
Figure 5.4 (a) Optical microscope image of an asymmetrical VO$_2$ beam on suspended membranes for thermal conductance measurement. (b) Scanning electron microscopy (SEM) image of an asymmetrical VO$_2$ beam. The VO$_2$ beams used in this study have a uniform thickness (typically 500nm- 1µm), with one end of narrow width (300nm- 900nm) and the other end of wide width (600nm - 2µm). The heat flow through the beam (Q) in either direction denoted by the arrows is accurately measured while the suspended platforms are maintained as isotherms at hot and cold temperatures, T_h and T_s respectively

5.3.1 The Gate Temperature (T_G) adjustment

It is important to note that we utilized the temperature-drive phase transition in VO$_2$, which involves thermal hysteresis. Therefore, a change in the global temperature, T_G that functions as the thermal gate, can affect the measurement of thermal properties. The global temperature can be adjusted in multiple ways. First, while keeping the direction of heat flow constant, the conductance in that direction can be measured for all gate temperatures from 300-380K, ie. traversing the phase transition at around 340K. Then the direction of heat flow can be swapped and the conductance in the reverse direction can be measured again at all temperatures between 380-300K. While most convenient, this requires the beam to undergo a temperature cycle and hysteresis before properties in the reverse direction can be measured. Hence, this approach was not pursued.

To circumvent this problem, the following approach was used. At each gate temperature, T_G, the conductance is measured in both directions of the beam by switching the heating and sensing membranes. This is the most direct way of observing rectification as the conductance in both directions is measured before T_G is changed. Since the maximum $\Delta T < 2$ K, we believe that this will have marginal hysteretic effect on our conductance measurements. However, in order to accurately estimate the temperature change on the heating and sensing sides $\Delta T = \Delta T_h - \Delta T_s$, the platinum-resistance thermometer (PRT)

needs to be calibrated. At low temperatures, the change in resistance as a function of temperature is non-linear and introduces significant error in the measurement. To address this issue, the following modification was then used.

The PRT was calibrated by measuring the local change in resistance around a particular gate temperature. For example, to get an accurate value of the TCR (Temperature Coefficient of Resistivity) of the Platinum film used for temperature measurement at 200K, four-point resistance measurement on the heating and sensing sides was done at 195K, 198K, 200K, 202K and 205K. Then, the TCR obtained from the localized calibration can be utilized to accurately calculate the temperature. Rectification is observed with all three approaches described above, while the third approach unequivocally shows convergence of the conductance in both directions at low temperatures.

5.3.2 Temperature Gated Thermal Rectification Results

Fig 5.5(a) shows measured heat flow, Q, and the temperature difference, ΔT, across a tapered VO$_2$ beam at T_G of 300K below the phase transition temperature of 340 K. The heat flow, Q, increases linearly with ΔT (<1K). However, the thermal conductance, $G = Q/\Delta T$, or the slope, differs depending on the direction of heat flow. The thermal conductance of the tapered beam when heat is flowing from the narrow to the broader side (61 ± 2.7 nW/K) is significantly smaller than that in the other direction (73 ± 3.3 nW/K). This represents a 22 ± 7.8% thermal rectification, which is the highest ever reported to the best of our knowledge, with a proposed nanostructure-induced mechanism. Note that upto 75% rectification was observed in a Quartz-Graphite structure purely due to different temperature dependence of the constituent elements [154] . Also shown in Fig 5.5(b) is the δQ, which is the deviation of the heat flow in one direction, Q, from the extrapolated linear curve representing the conductance in the opposite direction. Figs 5.5(c) and 5.5(d) show similar plots for the same VO$_2$ beam at T_G = 350 K, which is higher than the phase transition temperature where the VO$_2$ beam is in the metallic phase. In contrast to Figs 5.5(a) and 5.5(b), it is clear that no rectification is observed and the thermal conductance in both directions increases to 98 ± 4.4 nW/K.
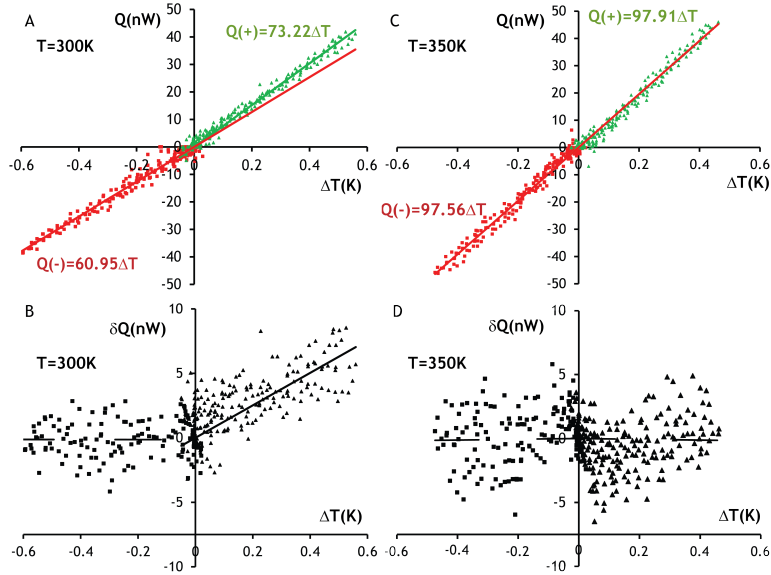
Figure 5.5 (a) and (c) heat flow (Q) as a function of temperature difference ΔT across the VO$_2$ beams at 300K and 350K, respectively. Different signs (+) and (-) of Q represent different directions of heat transfer. (b) and (d) heat flow deviation (δQ) as a function of temperature difference across the VO$_2$ beams at 300K and 350K, respectively.

The same plots of Q and δQ at 300 K of an untapered VO$_2$ beam show that there is no rectification (Fig 5.6 (a-d)).
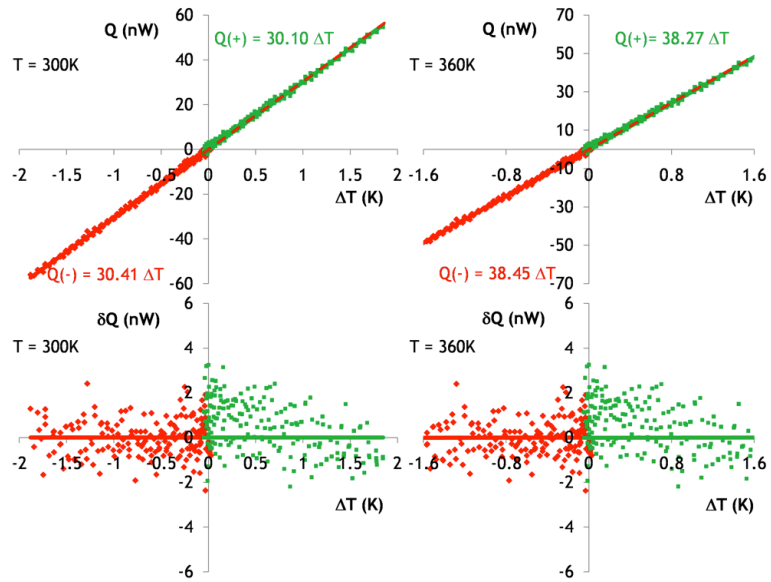
Figure 5.6 (a) and (c) heat flow (Q) as a function of temperature difference (ΔT) across the uniform VO$_2$ beams at 300K and 360K respectively. Different signs (+) and (-) of thermal power (Q) represent different directions of heat transfer. (b) and (d) heat flow deviation (δQ) from linear fit as a function of temperature difference (ΔT) across the VO$_2$ beams at 300K and 360K correspondingly.

The thermal rectifications of five asymmetrical VO_2 beams were found to be around 15%, when T_G < 340K, and reduced to below 4% and within the measurement noise for T_G > 340K (Table 5.1).

No.	300K			350K		
	G+ (nW/K)	G- (nW/K)	R (%)	G+ (nW/K)	G- (nW/K)	R (%)
I	73±3.3	60±2.7	22±7.8%	98±4.6	98±4.6	0±6.6%
II	144±7.2	123±6.1	17±8.3%	165±8.2	160±8.0	3±7.3%
III	117±5.8	103±5.2	13±8.0%	118±5.9	114±5.7	4±7.3%
IV	191±9.6	169±8.4	13±8.0%	181±9.0	179±9.0	1±7.2%
V	56±4.6	48±3.9	17±13%	53±1.4	49±1.3	8±4.0%
VI	175±8.8	156±7.8	12±7.9%	178±8.9	172±8.6	3±7.3%

Table 5.1 Thermal conductance and thermal rectification of five different VO_2 beams

5.3.2 Effect of Gate Temperature on Rectification

Since the metal and insulating phases of VO_2 depend strongly on the gate temperature, a temperature dependent measurement would shed more light on the possible mechanisms causing heat to rectify. Fig 5.7(a) shows the thermal conductance in two directions as a function of global temperature for beams with and without rectification. It is observed that the degree of rectification, R, (black open circles) peaks around 300-320K, lower than the phase transition of 340K and decreases as the temperature is increased or decreased away from the transition. Above the VO_2 insulator-metal transition temperature (~340K), the electronic density of states at the Fermi Level increase significantly and electrons start contributing to the thermal conductance, which explains a sudden increase. This is also consistent with electrical resistance measurements (see Fig 5.7(b)), which show a 2-orders of magnitude drop at 340K indicating the characteristic insulator-to-metal phase transition, consistent with reports in literature for the electronic VO_2 phase transition [149]. Below 135K, the electronic contribution is negligible and phonons dominate heat conduction. In this temperature range, we do not observe any rectification as well. The phonon mean free paths are limited by scattering from either defects, interfaces or boundaries, and the thermal conductance increases with temperature due to increase in phonon population.
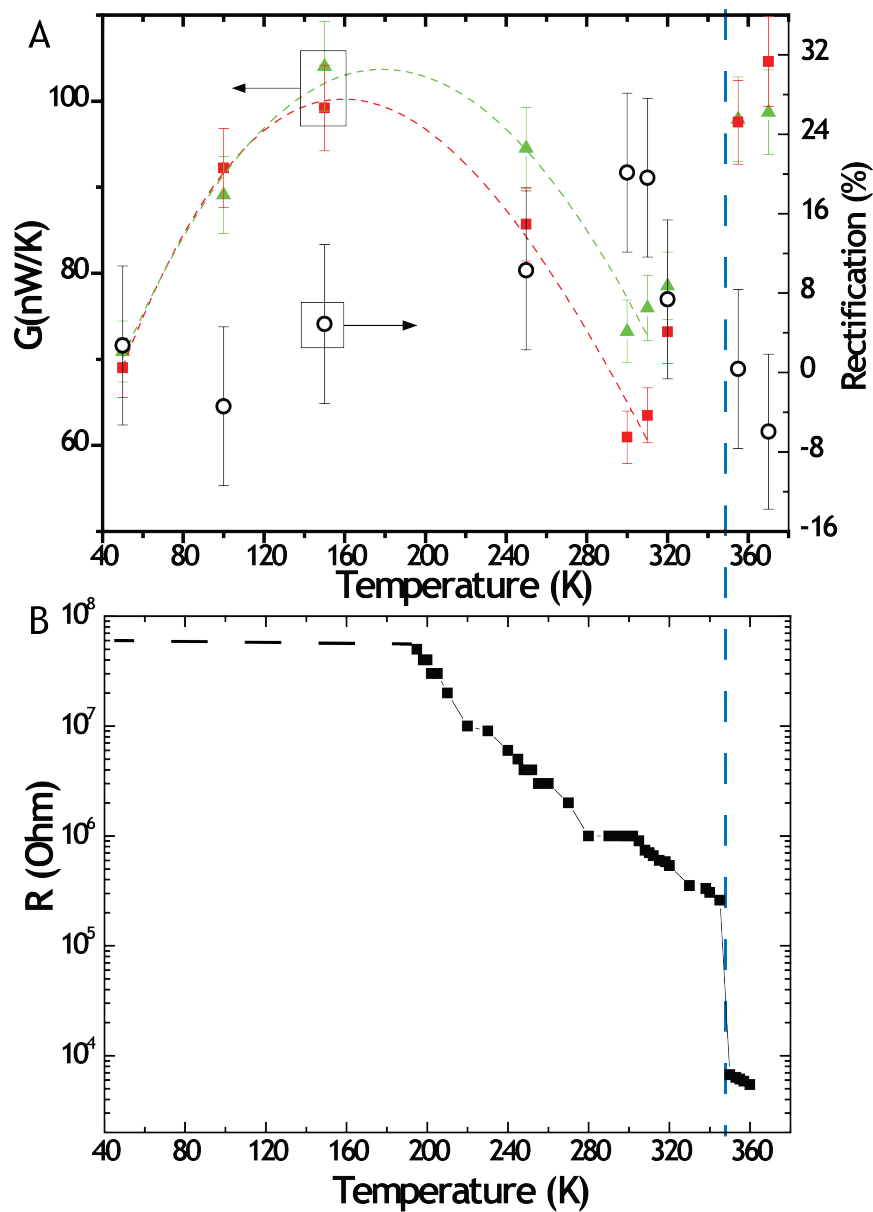
Figure 5.7 (a) Thermal conductance of an asymmetrical VO_2 beam as a function of global temperatures along two opposite directions. The thermal conductance is found to be measurably higher when heat flows from the wide end to the narrow end. At low temperatures, the rectification disappears and the conductance from either end is identical; this is expected as the whole wire is in the insulating phase and should behave as a normal dielectric. (b) the electrical resistance of VO_2 beam as a function of global temperature. The dotted line represents saturation of measured voltage for applied current (10 nA); the resistance could not be measured below 180K. The arrows in Figure 2 denote the direction of heat flow in which high (green) and low (red) thermal conductance was observed.

106

5.4 DISCUSSION AND ANALYSIS

It has been proposed that an asymmetric geometry or roughness may cause thermal rectification in materials when phonons dominate the heat conduction and the phonon mean free path is comparable to the characteristic length of the structure [135]. In order to eliminate this possibility, let us estimate the phonon mean free path in single crystal VO_2. A kinetic theory expression for the average phonon mean free path is: $\Lambda = \frac{3k}{cv}$. In the calculation, k is the thermal conductivity of VO_2 beam, the volumetric heat capacity c is taken to be the bulk value of VO_2, and v is taken to be the speed of sound. In the case of our VO_2 beam, Λ is estimated to be on the order of 1 nm at 300K. It is noted that the phonon mean free path based on kinetic theory usually leads to an underestimation of the mean free path for those phonons that are actually carrying the heat primarily for three reasons:

1. The average phonon group velocity is smaller than the speed of sound
2. Optical phonons contribute to the specific heat but little to heat transport
3. Phonon scattering is highly frequency dependent.

However, considering almost 3 orders of difference between the estimated phonon mean free path and the lateral length scale of our beams, it is believed that thermal rectification directly due to geometric effect that requires boundary scattering to be dominant is very unlikely.

Below 50 K, the phonon mean free path should increase by at least one order of magnitude. Therefore, any thermal rectification caused by asymmetrical geometry should be a lot more significant at lower temperature, which is not observed in Figure 5.7(a). So it is not possible that uneven phonon heat conduction due to asymmetrical geometry could cause the observed large thermal rectification.

It is seen that the metal-insulator phase transition in VO_2 is indeed essential for large thermal rectification observed here. Previous work has shown the co-existence of metallic and insulating phases within a single beam during phase transition [146], [147], [149]. To the best of our knowledge, except for the very early work in CuO-Cu system [155], thermal rectification due to the co-existence of metallic and insulating phases has not been observed experimentally. A recent theoretical study estimated the thermal resistance between a metal and an insulator by employing the two-temperature model to account for the lack of equilibrium between electrons and phonons near a metal-insulator interface [156] while maintaining same lattice temperature. It has been further theoretically predicted that thermal rectification could occur if metallic and insulating phases co-exist in a material system [139]. The underlying principle is the asymmetry between the energy transfer rate between electrons and phonons, when the electrons and phonons are not in equilibrium in a metal close to the interface. To observe significant thermal rectification in a metal-insulator system, the thermal resistance due to electron-phonon scattering should dominate over that from phonon-phonon coupling. Indeed, in the vanadium oxide

system, it was reported that a small 1% lattice distortion [149] in the rutile and monoclinic phases should ensure good acoustic match to reduce thermal resistance from phonon-phonon coupling. Therefore, it is possible that the electron-phonon scattering may be dominant for the contact resistance at metal-insulator interfaces in VO_2 beams, leading to measurable thermal rectification due to the abundance co-existing metallic and insulating phases.

It is intriguing that thermal rectification was observed not only near phase transition temperature 340K, but also over large span of ~100K below, provoking the question as to the role of the taper of the VO_2 beams. Even though the VO_2 beams show characteristic electronic transition temperature (340K) and Raman spectrum (supplementary materials), it has been known that vanadium oxide can form Magnéli phases with a deficiency of oxygen, given by the general formula V_nO_{2n-1}. These are crystallographic shear compounds with a rutile VO_2 backbone [157]. The role of stoichiometry in $V_nO_{2n-1} = V_2O_3 + (n-2)VO_2$ single crystals has been studied in meticulous details [152]. As observed in Figure 4A, the 'on' state of rectification exists between 250K and 340K, where the V_2O_3 shear planes would be metallic and the VO_2 matrix would be insulating. Therefore, a small variation in stoichiometry of vanadium oxide can cause the existence of metal-insulator interfaces over a very large range of temperature [152]. As shown in Figure 5.7(a), between 250 K and 340K where rectification exists, the conductance decreases with increasing temperatures. It can be caused by phonon-phonon Umklapp scattering, but can also be attributed to the appearance of interfaces created by the formation and co-existence of multiple phases of vanadium oxide that may be not electronically connected, but impede phonons due to interface scattering. We have indeed found the signature of mixed vanadium oxide phases in tapered beams using Auger Electron Spectroscopy (AES) seen below in Fig 5.8.
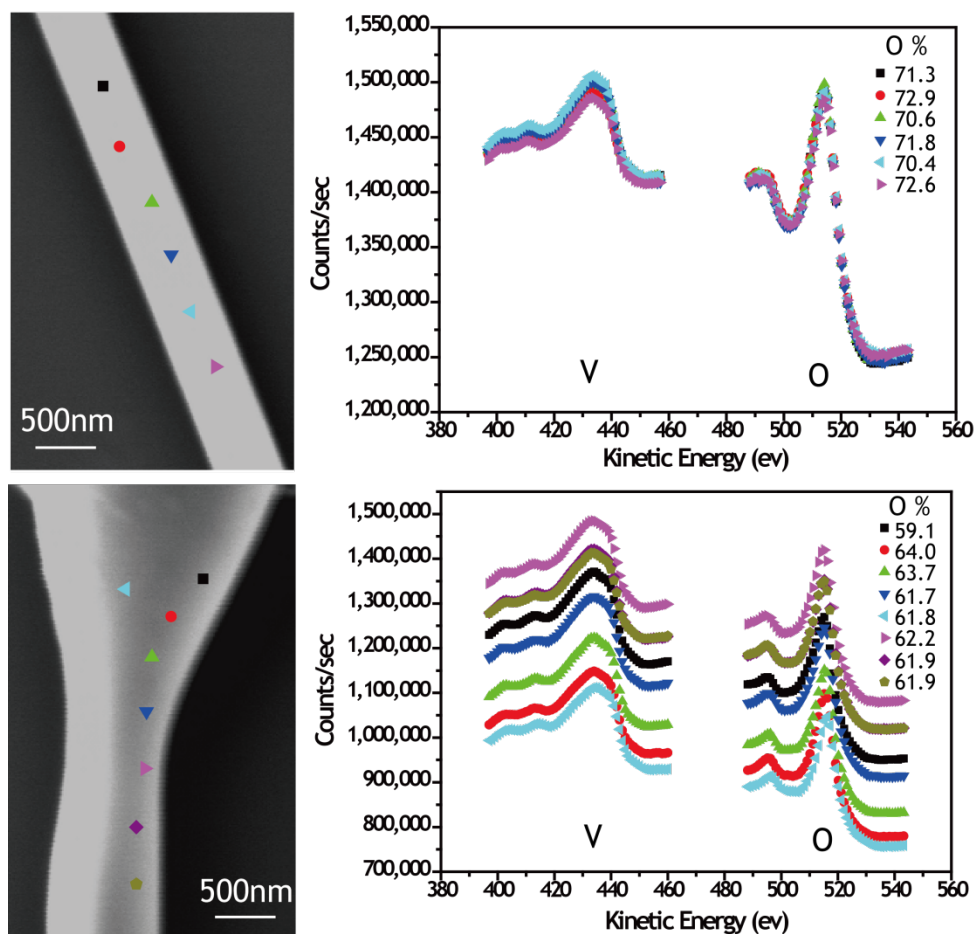
Figure 5.8 (a) Scanning Electron Microscopy (SEM) image of a uniform VO_2 beam, with colored symbols represent locations used (~10nm resolution) for stoichiometry analysis. (b) Auger Electron Spectra for the uniform VO_2 beam, with different colors representing the places labeled in (a). (c) Scanning Electron Microscopy (SEM) image of an asymmetric VO_2 beam, with colored symbols represent places for stoichiometry analysis. (d) Auger Electron Spectra for the asymmetric VO_2 beam, with different colors represent the places labeled in (c).

It is observed that the oxygen composition on the surface of the uniform beam is higher than 66.7% (as in VO_2). This oxygen-rich surface can be attributed to the general oxygen rich environment, as the beams are exposed to air during storage. It has been demonstrated in literature that exposing bulk VO_2 single crystals to an oxygen environment can produce surface oxidation tending towards V_2O_5 (71.4% oxygen) [158]. Such a study has not been performed on VO_2 beams grown using our techniques, but given the larger surface-to-volume ratio of such nano/micro scale beams, it is highly likely that the surface of the VO_2 beams in our study is oxygen-rich. Interestingly, it is observed that the oxygen composition on the surface of an asymmetric beam is lower than 66.7% (Fig 5.8(d)), despite the general oxygen rich environment. As discussed

earlier, the phase transition temperature is very sensitive to the stoichiometry of V_nO_{2n-1}. Hence, we expect these oxygen-deficient spots to remain in a metallic phase over a large range of temperatures (down to 135K for V_2O_3) [157], [159].

Also it is noteworthy that recent work shows that the phase transition also depends on the stress fields within single VO_2 beams [149]. It is likely that a taper created during beam growth may lead to stress concentrations which could potentially produce geometrical and size distributions of metallic and insulating domains and interfaces near the taper, which could amplify the rectification achieved by single interfaces. Similar distributions were previous reported by bending the beam [146]. Hence, while the metal-insulator phase transition is critical to thermal rectification, the taper and composition variation may also contribute to the effect due to unique distributions of metal-insulator domains. Over the last few decades, while tremendous efforts has been made in understanding the complexity of the metal-insulator phase transition in the family of vanadium oxide, the underlying physics still remains largely illusive [160]. Its impact on thermal transport is yet to be fully understood.

5.5 CONCLUSION

In summary, we report an unprecedented large thermal rectification up to 22% in VO_2 beams that is gated by environmental temperature. Such a three terminal device exhibits an "on" state over large range of temperature (T_G = 250-340 K) and "off" state (T_G < 250 K or T_G > 340K). Hence, by changing temperature, one can switch the rectification, much like a gate voltage switches a thyristor between two states of electrical conductance. Such novel all-thermal devices may spur interesting applications in autonomous thermal flow control and efficient energy harvesting.

CHAPTER 6

CONCLUSIONS AND OUTLOOK

This thesis describes the use of a microfabricated platform to measure thermal conductivity and establish a one-one relation between the characterized structure and the thermal properties of three different material systems. In Chapter 1 we provide an introduction to phonons and how heat travels in dielectric solids. In Chapter 2 we describe the details of measurement of thermal conductivity using the platform and the limits that define accurate estimation of nanowire thermal properties. State-of-the-art measurements ensure a sensitivity down to ~4 pW with μK temperature resolution. In our system, we can measure thermal conductance down to ~1 nW/K. On the other hand, the limit to measuring larger conductances lies in the contribution due to thermal contact resistance, which is around 1-15 K/μW depending on the geometry of the system being measured. Knowing these limits can ensure accurate measurement of thermal conductivity of different material systems. In the subsequent chapters, the thesis describes three novel materials, each exhibiting unique thermal properties.

In Chapter 3, we've carefully studied the effect of morphology on the thermal conductivity of rough Silicon Nanowires. Scanning Transmission Electron Microscopy (STEM), TEM and three-dimensional tomography were used to characterize single-crystalline nanowires roughened with three separate roughening chemistries. Key structural details such as porosity, non-circular cross-section, extended defects, necks, residual metal particles and amorphous native oxide regions were identified and incorporated in the geometrical reconstruction of the nanowires. Thermal conductivity of rough single nanowires was then measured on those exact same nanowires whose structure was characterized with electron microscopy. A correlation that related a spectrally determined surface roughness parameter, α_p to the measured thermal conductivity was found. When α_p is larger, the nanowire is rougher and the thermal conductivity is lower. α_p captures the amplitude of the rough surface of the nanowire where the roughness matches the dominant wavelength of phonons contributing to thermal conductivity ($\lambda \sim 1 - 100 nm$ at 300K).

In Chapter 4, we study the anisotropy of thermal transport in Bismuth nanowires. Here we move from a semiconductor (Silicon) in Chapter 3, to a semimetal, where both electrons and phonons contribute to thermal conductivity. We find that both carriers have their mean free path restricted by diameter. More interestingly, the thermal conductivity depends on crystal direction. This can occur due to a difference in group velocity in

different crystal directions. Again, the thermal measurement platform provides a convenient tool to characterize the crystal growth direction of different nanowires with Selected Area Diffraction (SAD) and link it with changes in thermal conductivity.

Finally, in Chapter 5, we study for the first time, the thermal properties of a single crystal of correlated electron material, Vanadium Dioxide. While this interesting material undergoes a structural and electronic phase transition at ~68°C, how this transition affects phonons has not been studied so far. We find that imperfect growth of beams of the Vanadium-Oxide family, V_nO_{2n-1} result in the possibility of many metal-insulator interfaces co-existing. These manifest in asymmetric thermal transport across the VO_x beam, which switches off at high (>68°C) and low (<-140°C) temperatures, but provides thermal rectification of up to 22% in the intermediate temperature range. Again, the measurement platform comes in handy, as we can perform simultaneous electrical and thermal measurements on the VO_2 beams, while the same samples can be used for TEM as well as Auger Spectroscopy.

Overall, we've strived to utilize the thermal measurement platform to study properties of different materials system, gaining unique understanding on their structure and morphology and hence advancing the field of thermal transport in nanostructures.

Considering the bigger picture, heat plays an ever-more important role in the world today. 65% of all energy conversion losses occur in the form of heat [161]. Hence, designing and tailoring heat is an important challenge that engineers and scientists face. Nanostructuring has provided a new tool to experiment with in the past couple of decades, and has shown promising developments, as outlined briefly in Chapter 1 and shown in detail in the subsequent chapters for three different material systems. However, the next new wave of discoveries surely lies in understanding the wave nature of phonons.

High quality nanostructures can now be made that have their critical length scales close to the dominant phonon wavelength contributing to thermal conductivity, such as epitaxially grown superlattices, advanced nanofabricated structures and nanowires. Studying the thermal properties of such nanostructures is challenging on two fronts: (1) design and preparation of sub-10nm samples for thermal studies, and (2) exploring the limits of sensitivity of thermal measurements in order to probe their properties. The broadband nature of phonons is an impediment to clearly observing wavelike behavior of phonons, as the phonons interact with each other in an energy bandwidth given by ~k_BT. Of course in the perfectly harmonic approximation, there are no interactions between phonons. Waves travel freely without attenuation and have infinite mean free paths, but this is far from the actual scenario. In reality, interactions in dielectrics with low defect density can be restricted to normal and umklapp scattering. Normal scattering conserves phonon momentum; umklapp scattering changes total phonon momentum. Hence, in the regime of normal scattering, phases of the phonon waves can possibly be preserved. Then, by introducing nanoparticles or rationally designed surfaces, coherent scattering of the phonons can be induced. The effects of these on thermal conductivity is unexplored territory and can lead to phenomena such as time reversal, multiple coherent backscattering and Anderson localization. Such experiments have been performed on Bose Einstein Condensates (matter waves) [162], electrons [163], [164], photons [165],

elastic waves [166], acoustics[167], [168], and even water waves [169]! Probing these wave phenomena, of course, is a formidable task. Far from experimental realization, such wave phenomenon has received little formal theoretical treatment for phonons [170].

Further, while steady state thermal conductivity measurements on nanostructures are state of the art, transient measurements need to be designed to probe the time scales of scattering of thermal phonons. This thesis emphasizes the 1-1 correlation between solid-state structure and thermal properties. In-situ experiments where the transient measurements of nanostructures can be probed while observing changes in structure and/or controlling scattering rates (as a function of temperature, for example) can be designed and will further help in understand the transport of phonons in solid state systems.

Bibliography

[1]   C. Kittel, *Introduction to Solid State Physics*. Wiley, 2005.

[2]   G. Dolling, "Inelastic Scattering of Neutrons in Solids and Liquids (IAEA, Vienna, 1963)," *Vol. II*, pp. 37–45.

[3]   M. Holland, "Analysis of Lattice Thermal Conductivity," *Physical Review*, vol. 132, no. 6, pp. 2461–2471, 1963.

[4]   D. J. Griffiths, *Introduction To Quantum Mechanics*, 2nd ed. Pearson Education India, 2005.

[5]   J. Callaway, "Model for Lattice Thermal Conductivity at Low Temperatures," *Physical Review*, vol. 113, no. 4, pp. 1046–1051, 1959.

[6]   R. Eisberg and R. Resnick, "Quantum Physics." New York: John Wiley & Sons, Inc, 1974.

[7]   C. L. Tien, A. Majumdar, and F. F. M. Gerner, *Microscale Energy Transfer*. CRC Press Llc, 1998.

[8]   H.-M. Kagaya and T. Soma, "Specific Heat of Si and Ge," *Phys. Stat. Sol. (b)*, vol. 127, pp. 5–7, 1985.

[9]   J. M. Ziman, *Electrons and Phonons: The Theory of Transport Phenomena in Solids*. Clarendon, Oxford, 1960.

[10]   V. R. Peierls, "Zur kinetischen Theorie der Warmerleitung in Kristallen," *Annalen der Physik*, vol. 395, no. 8, pp. 1055–1101, 1929.

[11]   K. Esfarjani, G. Chen, and H. Stokes, "Heat transport in silicon from first-principles calculations," *Physical Review B*, vol. 84, no. 8, pp. 1–11, Aug. 2011.

[12]   P. Klemens, "The Scattering of Low-Frequency Lattice Waves by Static Imperfections," *Proceedings of the Physical Society A*, vol. 68, pp. 1113–1128, 1955.

[13]   A. Majumdar, "Microscale Heat Conduction in Dielectric Thin Films," *Journal of Heat Transfer*, vol. 115, pp. 7–16, 1993.

[14]   H. Casimir, "Note on the conduction of heat in crystals," *Physica V*, vol. 6, no. 85, pp. 495–500, 1938.

[15] D. G. Cahill, W. K. Ford, K. E. Goodson, G. D. Mahan, A. Majumdar, H. J. Maris, R. Merlin, and S. R. Phillpot, "Nanoscale thermal transport," *Journal of Applied Physics*, vol. 93, no. 2, p. 793, 2003.

[16] J. S. Heron, T. Fournier, N. Mingo, and O. Bourgeois, "Mesoscopic size effects on the thermal conductance of silicon nanowire.," *Nano letters*, vol. 9, no. 5, pp. 1861–5, May 2009.

[17] M. Siemens, Q. Li, and R. Yang, "Quasi-ballistic thermal transport from nanoscale interfaces observed using ultrafast coherent soft X-ray beams," *Nature materials*, vol. 9, no. 26, 2009.

[18] R. Cheaito, J. C. Duda, T. E. Beechem, K. Hattar, J. F. Ihlefeld, D. L. Medlin, M. a. Rodriguez, M. J. Campion, E. S. Piekos, and P. E. Hopkins, "Experimental Investigation of Size Effects on the Thermal Conductivity of Silicon-Germanium Alloy Thin Films," *Physical Review Letters*, vol. 109, no. 19, p. 195901, Nov. 2012.

[19] R. Chen, A. I. Hochbaum, P. Murphy, J. Moore, P. Yang, and A. Majumdar, "Thermal Conductance of Thin Silicon Nanowires," *Physical Review Letters*, vol. 101, no. 10, pp. 1–4, Sep. 2008.

[20] M. N. Luckyanova, J. Garg, K. Esfarjani, a. Jandl, M. T. Bulsara, A. J. Schmidt, A. J. Minnich, S. Chen, M. S. Dresselhaus, Z. Ren, E. A. Fitzgerald, and G. Chen, "Coherent Phonon Heat Conduction in Superlattices," *Science*, vol. 338, no. 6109, pp. 936–939, Nov. 2012.

[21] A. Minnich, J. Johnson, A. Schmidt, K. Esfarjani, M. Dresselhaus, K. Nelson, and G. Chen, "Thermal Conductivity Spectroscopy Technique to Measure Phonon Mean Free Paths," *Physical Review Letters*, vol. 107, no. 9, pp. 1–4, Aug. 2011.

[22] K. T. Regner, D. P. Sellan, Z. Su, C. H. Amon, A. J. H. McGaughey, and J. A. Malen, "Broadband phonon mean free path contributions to thermal conductivity measured using frequency domain thermoreflectance," *Nature Communications*, vol. 4, p. 1640, Mar. 2013.

[23] Y. K. Koh, Y. Cao, D. G. Cahill, and D. Jena, "Heat-Transport Mechanisms in Superlattices," *Advanced Functional Materials*, vol. 19, no. 4, pp. 610–615, Feb. 2009.

[24] F. Yang and C. Dames, "Mean free path spectra as a tool to understand thermal conductivity in bulk and nanostructures," *Physical Review B*, vol. 87, no. 3, p. 035437, Jan. 2013.

[25] G. Chen, *Nanoscale Energy Transport and Conversion: A Parallel Treatment of Electrons, Molecules, Phonons, and Photons*. Oxford University Press, 2005.

[26] C. Dames and G. Chen, in *Thermoelectrics Handbook: Macro to Nano-Structured Materials*, D. Rowe, Ed. 2005, pp. 1–17.

[27] K. Schwab, E. Henriksen, J. Worlock, and M. Roukes, "Measurement of the quantum of thermal conductance," *Nature*, vol. 404, no. 6781, pp. 974–7, Apr. 2000.

[28] Z. Zhang, *Nano/Microscale Heat Transfer*. McGraw-Hill Education, 2007.

[29] F. Yang, T. Ikeda, G. J. Snyder, and C. Dames, "Effective thermal conductivity of polycrystalline materials with randomly oriented superlattice grains," *Journal of Applied Physics*, vol. 108, no. 3, p. 034310, 2010.

[30] M. Holland, "Phonon Scattering in Semiconductors from Thermal Conductivity Studies," *Physical Review*, vol. 134, no. 2A, pp. A471–480, 1964.

[31] T. Klitsner and R. Pohl, "Phonon scattering at silicon crystal surfaces," *Physical Review B*, vol. 36, no. 12, pp. 6551–6565, 1987.

[32] M. Asheghi, Y. K. Leung, S. S. Wong, and K. E. Goodson, "Phonon-boundary scattering in thin silicon layers," *Applied Physics Letters*, vol. 71, no. May, pp. 1798–1800, 1997.

[33] Y. Ju and K. Goodson, "Phonon scattering in silicon films with thickness of order 100 nm," *Applied Physics Letters*, vol. 74, no. 20, pp. 3005–3007, 1999.

[34] E. H. Sondheimer, "Advances in Physics The mean free path of electrons in metals," *Advances in Physics*, vol. 1, no. 1, 1952.

[35] D. Li, Y. Wu, P. Kim, L. Shi, P. Yang, and A. Majumdar, "Thermal conductivity of individual silicon nanowires," *Applied Physics Letters*, vol. 83, no. 14, p. 2934, 2003.

[36] A. I. Hochbaum, R. Chen, R. D. Delgado, W. Liang, E. C. Garnett, M. Najarian, A. Majumdar, and P. Yang, "Enhanced thermoelectric performance of rough silicon nanowires," *Nature*, vol. 451, no. 7175, pp. 163–7, Jan. 2008.

[37] B. Taylor, H. Maris, and C. Elbaum, "Phonon Focusing in Solids," *Physical Review Letters*, vol. 23, no. 8, pp. 416–420, 1969.

[38] H. J. Maris, "Enhancement of Heat Pulses in Crystals due to Elastic Anisotropy," *Journal of the Acoustic Society of America*, vol. 50, no. 3, pp. 812–818, 1971.

[39] A. McCurdy, H. Maris, and C. Elbaum, "Anisotropic Heat Conduction in Cubic Crystals in the Boundary Scattering Regime," *Physical Review B*, vol. 2, no. 10, pp. 4077–4083, 1979.

[40] G. Northrop and J. Wolfe, "Ballistic phonon imaging in germanium," *Physical Review B*, vol. 22, no. 12, 1980.

[41] H. Bommel and K. Dransfeld, "Excitation and Attenuation of Hypersonic Waves in Quartz," *Physical Review*, vol. 117, no. 5, pp. 1245–1252, 1960.

[42] R. von Gutfelt and J. Nethercot, AH, "Heat pulses in quartz and sapphire at low temperatures," *Physical Review Letters*, vol. 12, no. 23, 1964.

[43] J. P. Wolfe, *Imaging phonons: acoustic wave propagation in solids*. Cambridge University Press, 2005.

[44] V. Narayanamurti, "Phonon Optics and Phonon Propagation in Semiconductors," *Science*, vol. 213, no. 4509, pp. 717–723, 1981.

[45] V. Narayanamurti, H. Stormer, M. Chin, A. Gossard, and W. Wiegmann, "Selective Transmission of High-Frequency Phonons by a Superlattice: The 'Dielectric' Phonon Filter," *Physical Review Letters*, vol. 43, no. 27, 1979.

[46] V. Narayanamurthi and R. Dynes, "Observation of Second Sound in Bismuth," *Physical Review Letters*, vol. 28, no. 22, pp. 1461–1465, 1972.

[47] R. Dynes, V. Narayanamurti, and M. Chin, "Monochromatic Phonon Propagation in Ge:Sb Using Superconducting Tunnel Junctions," *Physical Review Letters*, vol. 26, no. 4, pp. 181–184, 1971.

[48] R. Venkatasubramanian, "Lattice thermal conductivity reduction and phonon localization like behavior in superlattice structures," *Physical Review B*, vol. 61, no. 4, pp. 3091–3097, 2000.

[49] W. Kim, J. Zide, A. Gossard, D. Klenov, S. Stemmer, A. Shakouri, and A. Majumdar, "Thermal Conductivity Reduction and Thermoelectric Figure of Merit Increase by Embedding Nanoparticles in Crystalline Semiconductors," *Physical Review Letters*, vol. 96, no. 4, pp. 1–4, Feb. 2006.

[50] K. Hippalgaonkar, B. Huang, R. Chen, K. Sawyer, P. Ercius, and A. Majumdar, "Fabrication of microdevices with integrated nanowires for investigating low-dimensional phonon transport.," *Nano letters*, vol. 10, no. 11, pp. 4341–8, Nov. 2010.

[51] P. Kim, L. Shi, a. Majumdar, and P. McEuen, "Thermal Transport Measurements of Individual Multiwalled Nanotubes," *Physical Review Letters*, vol. 87, no. 21, pp. 19–22, Oct. 2001.

[52] L. Shi, D. Li, C. Yu, W. Jang, D. Kim, Z. Yao, P. Kim, and A. Majumdar, "Measuring Thermal and Thermoelectric Properties of One-Dimensional Nanostructures Using a Microfabricated Device," *Journal of Heat Transfer*, vol. 125, no. 5, p. 881, 2003.

[53] C. Yu, S. Saha, J. Zhou, L. Shi, A. M. Cassell, B. a. Cruden, Q. Ngo, and J. Li, "Thermal Contact Resistance and Thermal Conductivity of a Carbon Nanofiber," *Journal of Heat Transfer*, vol. 128, no. 3, p. 234, 2006.

[54] A. Mavrokefalos, M. T. Pettes, F. Zhou, and L. Shi, "Four-probe measurements of the in-plane thermoelectric properties of nanofilms.," *The Review of scientific instruments*, vol. 78, no. 3, p. 034901, Mar. 2007.

[55] D. Li, "Thermal Transport in Individual Nanowires and Nanotubes," UC Berkeley, 2002.

[56] M. T. Pettes and L. Shi, "Thermal and Structural Characterizations of Individual Single-, Double-, and Multi-Walled Carbon Nanotubes," *Advanced Functional Materials*, vol. 19, no. 24, pp. 3918–3925, Dec. 2009.

[57] F. P. Incropera and D. P. DeWitt, *Introduction to Heat Transfer*. Wiley, 2001.

[58] I. Utke, P. Hoffmann, and J. Melngailis, "Gas-assisted focused electron beam and ion beam processing and fabrication," *Journal of Vacuum Science & Technology B: Microelectronics and Nanometer Structures*, vol. 26, no. 4, p. 1197, 2008.

[59] G. R. Hadley, "Thermal conductivity of packed metal powders," *International Journal of Heat and Mass Transfer*, vol. 29, no. 6, pp. 909–920, 1986.

[60] V. N. Andreev, F. A. Chudnovskii, A. V Petrov, and E. I. Terukov, "Thermal Conductivity of VO2, V3O5, and V2O3," *Physica Status Solidi (A)*, vol. 48, pp. K153–156, 1978.

[61] C. Berglund and H. Guggenheim, "Electronic Properties of VO, near the Semiconductor-Metal Transition," *Physical Review*, vol. 185, no. 3, pp. 1022–1033, 1969.

[62] D.-W. Oh, C. Ko, S. Ramanathan, and D. G. Cahill, "Thermal conductivity and dynamic heat capacity across the metal-insulator transition in thin film VO_2," *Applied Physics Letters*, vol. 96, no. 15, p. 151906, 2010.

[63] H.-K. Lyeo and D. Cahill, "Thermal conductance of interfaces between highly dissimilar materials," *Physical Review B*, vol. 73, no. 14, pp. 1–6, Apr. 2006.

[64] J. Lim, K. Hippalgaonkar, S. C. Andrews, A. Majumdar, and P. Yang, "Quantifying surface roughness effects on phonon transport in silicon nanowires.," *Nano letters*, vol. 12, no. 5, pp. 2475–82, May 2012.

[65] A. I. Boukai, Y. Bunimovich, J. Tahir-Kheli, J.-K. Yu, W. A. Goddard, and J. R. Heath, "Silicon nanowires as efficient thermoelectric materials," *Nature*, vol. 451, no. 7175, pp. 168–71, Jan. 2008.

[66] M. C. Wingert, Z. C. Y. Chen, E. Dechaumphai, J. Moon, J.-H. Kim, J. Xiang, and R. Chen, "Thermal conductivity of Ge and Ge-Si core-shell nanowires in the phonon confinement regime.," *Nano letters*, vol. 11, no. 12, pp. 5507–13, Dec. 2011.

[67] S. Sadat, Y. J. Chua, W. Lee, Y. Ganjeh, K. Kurabayashi, E. Meyhofer, and P. Reddy, "Room temperature picowatt-resolution calorimetry," *Applied Physics Letters*, vol. 99, no. 4, p. 043106, 2011.

[68] S. Sadat, E. Meyhofer, and P. Reddy, "High resolution resistive thermometry for micro/nanoscale measurements.," *The Review of scientific instruments*, vol. 83, no. 8, p. 084902, Aug. 2012.

[69] S. Sadat, E. Meyhofer, and P. Reddy, "Resistance thermometry-based picowatt-resolution heat-flow calorimeter," *Applied Physics Letters*, vol. 102, no. 16, p. 163110, 2013.

[70] V. Gopal, V. R. Radmilovic, C. Daraio, S. Jin, P. Yang, and E. a. Stach, "Rapid Prototyping of Site-Specific Nanocontacts by Electron and Ion Beam Assisted Direct-Write Nanolithography," *Nano Letters*, vol. 4, no. 11, pp. 2059–2063, Nov. 2004.

[71] A. S. Henry and G. Chen, "Spectral Phonon Transport Properties of Silicon Based on Molecular Dynamics Simulations and Lattice Dynamics," *Journal of Computational and Theoretical Nanoscience*, vol. 5, no. 7, pp. 1193–1204, Jul. 2008.

[72] M. Asheghi, K. Kurabayashi, R. Kasnavi, and K. E. Goodson, "Thermal conduction in doped single-crystal silicon films," *Journal of Applied Physics*, vol. 91, no. 8, p. 5079, 2002.

[73] J. Tang, H.-T. Wang, D. H. Lee, M. Fardy, Z. Huo, T. P. Russell, and P. Yang, "Holey silicon as an efficient thermoelectric material.," *Nano letters*, vol. 10, no. 10, pp. 4279–83, Oct. 2010.

119

[74] C. Chiritescu, D. G. Cahill, N. Nguyen, D. Johnson, A. Bodapati, P. Keblinski, and P. Zschack, "Ultralow thermal conductivity in disordered, layered WSe$_2$ crystals.," *Science (New York, N.Y.)*, vol. 315, no. 5810, pp. 351–3, Jan. 2007.

[75] G. Joshi, H. Lee, Y. Lan, X. Wang, G. Zhu, D. Wang, R. W. Gould, D. C. Cuff, M. Y. Tang, M. S. Dresselhaus, G. Chen, and Z. Ren, "Enhanced thermoelectric figure-of-merit in nanostructured p-type silicon germanium bulk alloys.," *Nano letters*, vol. 8, no. 12, pp. 4670–4, Dec. 2008.

[76] N. Mingo, "Calculation of Si nanowire thermal conductivity using complete phonon dispersion relations," *Physical Review B*, vol. 68, no. 11, p. 113308, Sep. 2003.

[77] P. Martin, Z. Aksamija, E. Pop, and U. Ravaioli, "Impact of Phonon-Surface Roughness Scattering on Thermal Conductivity of Thin Si Nanowires," *Physical Review Letters*, vol. 102, no. 12, pp. 1–4, Mar. 2009.

[78] J. Carrete, L. Gallego, L. Varela, and N. Mingo, "Surface roughness and thermal conductivity of semiconductor nanowires: Going below the Casimir limit," *Physical Review B*, vol. 84, no. 7, pp. 1–4, Aug. 2011.

[79] A. L. Moore, S. K. Saha, R. S. Prasher, and L. Shi, "Phonon backscattering and thermal conductivity suppression in sawtooth nanowires," *Applied Physics Letters*, vol. 93, no. 8, p. 083112, 2008.

[80] Z. Wang, Z. Ni, R. Zhao, M. Chen, K. Bi, and Y. Chen, "The effect of surface roughness on lattice thermal conductivity of silicon nanowires," *Physica B: Condensed Matter*, vol. 406, no. 13, pp. 2515–2520, Jul. 2011.

[81] Y.-H. Park, J. Kim, H. Kim, I. Kim, K.-Y. Lee, D. Seo, H.-J. Choi, and W. Kim, "Thermal conductivity of VLS-grown rough Si nanowires with various surface roughnesses and diameters," *Applied Physics A*, vol. 104, no. 1, pp. 7–14, May 2011.

[82] H. Kim, Y.-H. Park, I. Kim, J. Kim, H.-J. Choi, and W. Kim, "Effect of surface roughness on thermal conductivity of VLS-grown rough Si1−x Ge x nanowires," *Applied Physics A*, vol. 104, no. 1, pp. 23–28, May 2011.

[83] E. I. Givargizov, "FUNDAMENTAL ASPECTS OF VLS GROWTH," *Journal of Crystal Growth*, vol. 31, pp. 20–30, 1975.

[84] A. I. Hochbaum, D. Gargas, Y. J. Hwang, and P. Yang, "Single crystalline mesoporous silicon nanowires.," *Nano letters*, vol. 9, no. 10, pp. 3550–4, Oct. 2009.

[85]   Z. Huang, N. Geyer, P. Werner, J. de Boor, and U. Gösele, "Metal-assisted chemical etching of silicon: a review.," *Advanced materials*, vol. 23, no. 2, pp. 285–308, Jan. 2011.

[86]   K. Peng, Y. Yan, S. Gao, and J. Zhu, "Dendrite-Assisted Growth of Silicon Nanowires in Electroless Metal Deposition," *Advanced Functional Materials*, vol. 13, no. 2, pp. 127–132, Feb. 2003.

[87]   M. Ge, J. Rong, X. Fang, and C. Zhou, "Porous doped silicon nanowires for lithium ion battery anode with long cycle life.," *Nano letters*, vol. 12, no. 5, pp. 2318–23, May 2012.

[88]   A. Jostsons and J. G. Napier, "The Determination of Foil Thickness by Scanning Transmission Electron Microscopy," *Phys. Stat. Sol.*, vol. 31, pp. 771–780, 1975.

[89]   S. Pennycook and L. Boatner, "Chemically Sensitive structure-imaging with a scanning transmission electron microscope," *Nature*, vol. 336, no. 8, pp. 565–567, 1988.

[90]   D. B. Williams and C. B. Carter, *The Transmission Electron Microscope*. Springer, 1996.

[91]   B. Fultz and J. Howe, *Transmission electron microscopy and diffractometry of materials*. Springer Verlag, 2012.

[92]   P. Ercius, M. Weyland, D. a. Muller, and L. M. Gignac, "Three-dimensional imaging of nanovoids in copper interconnects using incoherent bright field tomography," *Applied Physics Letters*, vol. 88, no. 24, p. 243116, 2006.

[93]   J. Sadhu and S. Sinha, "Room-temperature phonon boundary scattering below the Casimir limit," *Physical Review B*, vol. 84, no. 11, pp. 1–6, Sep. 2011.

[94]   M. Goodnick, R. G. Gann, R. J. Sites, D. K. Ferry, C. W. Wilmsen, D. Fathy, and O. Krivanek, "Surface roughness scattering at the Si-SiO$_2$ interface," *Journal of Vacuum Science & Technology B: Microelectronics and Nanometer Structures*, vol. 1, no. 3, pp. 803–808, 1983.

[95]   S. Goodnick, D. Ferry, C. Wilmsen, Z. Liliental, D. Fathy, and O. Krivanek, "Surface Roughness at the Si(100)-SiO$_2$ interface," *Physical Review B*, vol. 32, no. 12, pp. 8176–8186, 1985.

[96]   S. Yamakawa, H. Ueno, K. Taniguchi, C. Hamaguchi, K. Miyatsuji, and U. Ravaioli, "Study of interface roughness dependence of electron mobility in Si inversion layers using the Monte Carlo method," *Journal of Applied Physics*, vol. 79, no. 2, pp. 911–916, 1996.

[97]   D. H. Santamore and M. C. Cross, "Effect of surface roughness on phonon thermal conductance in the quantum limit," *Physica B: Condensed Matter*, vol. 316–317, pp. 389–392, May 2002.

[98]   J. Yang, Y. Yang, S. W. Waltermire, T. Gutu, A. a Zinn, T. T. Xu, Y. Chen, and D. Li, "Measurement of the Intrinsic Thermal Conductivity of a Multiwalled Carbon Nanotube and Its Contact Thermal Resistance with the Substrate.," *Small (Weinheim an der Bergstrasse, Germany)*, no. 16, pp. 2334–2340, Jun. 2011.

[99]   L. Liu and X. Chen, "Effect of surface roughness on thermal conductivity of silicon nanowires," *Journal of Applied Physics*, vol. 107, no. 3, p. 033501, 2010.

[100] M. G. Ghossoub, K. V Valavala, M. Seong, B. Azeredo, K. Hsu, J. S. Sadhu, P. K. Singh, and S. Sinha, "Spectral Phonon Scattering from Sub-10 nm Surface Roughness Wavelengths in Metal-Assisted Chemically Etched Si Nanowires.," *Nano letters*, vol. 13, no. 4, pp. 1564–71, Apr. 2013.

[101] F. X. Alvarez, D. Jou, and a. Sellitto, "Phonon hydrodynamics and phonon-boundary scattering in nanosystems," *Journal of Applied Physics*, vol. 105, no. 1, p. 014317, 2009.

[102] J. W. Roh, K. Hippalgaonkar, J. H. Ham, R. Chen, M. Z. Li, P. Ercius, A. Majumdar, W. Kim, and W. Lee, "Observation of anisotropy in thermal conductivity of individual single-crystalline bismuth nanowires.," *ACS nano*, vol. 5, no. 5, pp. 3954–60, May 2011.

[103] C. F. Gallo, B. S. Chandrasekhar, and P. H. Sutter, "Transport properties of bismuth single crystals.," *Journal of Applied Physics*, vol. 34, no. 1, pp. 144–152, Jun. 1963.

[104] K. Liu, C. L. Chien, P. C. Searson, and K. Yu-Zhang, "Structural and magneto-transport properties of electrodeposited bismuth nanowires," *Applied Physics Letters*, vol. 73, no. 10, p. 1436, 1998.

[105] Z. Zhang, X. Sun, and J. Y. Ying, "Electronic transport properties of single-crystal bismuth nanowire arrays," vol. 61, no. 7, pp. 4850–4861, 2000.

[106] B. Abeles and S. Meiboom, "Galvanomagnetic Effects in Bismuth," *Physical Review*, vol. 101, no. 2, pp. 544–560, 1956.

[107] J. Galt, W. Yager, F. Merritt, B. Cetlin, and A. Brailsford, "Cyclotron Absorptrion in Metallic Bismuth and its Alloys," *Physical Review*, vol. 114, no. 6, 1959.

[108] B. S. Chandrasekhar, "The Seebeck Coefficient of Bismuth Single Crystals," *Journal of Physics and Chemistry of Solids*, vol. 11, no. l, pp. 268–273, 1959.

[109] D. Shoenberg and Z. M. Uddin, "The Magnetic Properties of Bismuth II - The de Haas-van Alphen Effect," *Proceedings of the Royal Society of London. Series A, Mathematical and Physical Sciences*, pp. 701–720, 1936.

[110] J. Aubrey and R. Chambers, "Cyclotron Resonance in Bismuth," *Journal of Physics and Chemistry of Solids*, vol. 3, no. 1, pp. 128–132, 1957.

[111] S. Lee, J. Ham, K. Jeon, J.-S. Noh, and W. Lee, "Direct observation of the semimetal-to-semiconductor transition of individual single-crystal bismuth nanowires grown by on-film formation of nanowires.," *Nanotechnology*, vol. 21, no. 40, p. 405701, Oct. 2010.

[112] Y.-M. Lin, S. B. Cronin, J. Y. Ying, M. S. Dresselhaus, and J. P. Heremans, "Transport properties of Bi nanowire arrays," *Applied Physics Letters*, vol. 76, no. 26, p. 3944, 2000.

[113] G. K. White and S. B. Woods, "The thermal and electrical resistivity of bismuth and antimony at low temperatures," *Philosophical Magazine*, vol. 3, no. 28, pp. 342–359, Apr. 1958.

[114] Y. Eckstein, A. Lawson, and D. Renekker, "Elastic Constants of Bismuth," *Journal of Applied Physics*, vol. 31, no. 9, pp. 1534–1538, 1960.

[115] L. Hicks and M. Dresselhaus, "Thermoelectric figure of merit of one-dimensional conductor," *Physical Review B*, vol. 47, no. 24, pp. 12727–12731, 1993.

[116] L. Hicks and M. Dresselhaus, "Effect of quantum-well structures on the thermoelectric figure of merit," *Physical Review B*, vol. 47, no. 19, pp. 727–731, 1993.

[117] Y. Lin, X. Sun, and M. S. Dresselhaus, "Theoretical investigation of thermoelectric transport properties of cylindrical Bi nanowires," *Physical Review B*, vol. 62, no. 7, pp. 4610–4623, 2000.

[118] X. Sun, Z. Zhang, and M. S. Dresselhaus, "Theoretical modeling of thermoelectricity in Bi nanowires," *Applied Physics Letters*, vol. 74, no. 26, pp. 4005–4007, 1999.

[119] W. Shim, J. Ham, K.-I. Lee, W. Y. Jeung, M. Johnson, and W. Lee, "On-film formation of bi nanowires with extraordinary electron mobility.," *Nano letters*, vol. 9, no. 1, pp. 18–22, Jan. 2009.

[120] J. P. Heremans, "Low-Dimensional Thermoelectricity," vol. 108, no. 4, pp. 609–634, 2005.

[121] A. L. Moore, M. T. Pettes, F. Zhou, and L. Shi, "Thermal conductivity suppression in bismuth nanowires," *Journal of Applied Physics*, vol. 106, no. 3, p. 034310, 2009.

[122] J. Ham, W. Shim, D. H. Kim, S. Lee, J. Roh, S. W. Sohn, K. H. Oh, P. W. Voorhees, and W. Lee, "Direct growth of compound semiconductor nanowires by on-film formation of nanowires: bismuth telluride.," *Nano letters*, vol. 9, no. 8, pp. 2867–72, Aug. 2009.

[123] W. Shim, J. Ham, J. Kim, and W. Lee, "Shubnikov–de Haas oscillations in an individual single-crystalline bismuth nanowire grown by on-film formation of nanowires," *Applied Physics Letters*, vol. 95, no. 23, p. 232107, 2009.

[124] F. Zhou, J. Szczech, M. T. Pettes, A. L. Moore, S. Jin, and L. Shi, "Determination of transport properties in chromium disilicide nanowires via combined thermoelectric and structural characterizations.," *Nano letters*, vol. 7, no. 6, pp. 1649–54, Jun. 2007.

[125] J. Heremans and C. M. Thrush, "Thermoelectric power of bismuth nanowires," vol. 59, no. 19, pp. 579–583, 1999.

[126] M. Tian, N. Kumar, M. Chan, and T. Mallouk, "Evidence of local superconductivity in granular Bi nanowires fabricated by electrodeposition," *Physical Review B*, vol. 78, no. 4, p. 045417, Jul. 2008.

[127] M. Tian, J. Wang, Q. Zhang, N. Kumar, T. E. Mallouk, and M. H. W. Chan, "Superconductivity and quantum oscillations in crystalline Bi nanowire.," *Nano letters*, vol. 9, no. 9, pp. 3196–202, Sep. 2009.

[128] Z. Ye, H. Zhang, H. Liu, W. Wu, and Z. Luo, "Observation of superconductivity in single crystalline Bi nanowires.," *Nanotechnology*, vol. 19, no. 8, p. 085709, Feb. 2008.

[129] T. Huber, A. Adeyeye, A. Nikolaeva, L. Konopko, R. Johnson, and M. Graf, "Surface state mobility and thermopower in semiconducting bismuth nanowires," *arxiv*, pp. 1–20, 2013.

[130] N. Mingo and D. Broido, "Lattice Thermal Conductivity Crossovers in Semiconductor Nanowires," *Physical Review Letters*, vol. 93, no. 24, p. 246106, Dec. 2004.

[131] W. DeSorbo, "Low temperature Heat Capacity of Bismuth and Tungsten," *Journal of Physical Chemistry*, vol. 62, pp. 965–967, 1958.

[132] J. B. J. Fourier, *Théorie analytique de la chaleur*. Chez Firmin Didot, père et fils, 1822.

[133] G. S. Ohm, *Die galvanische kette: mathematisch*. T. H. Riemann, 1827.

[134] S. Chu and A. Majumdar, "Opportunities and challenges for a sustainable energy future," *Nature*, vol. 488, no. 7411, pp. 294–303, Aug. 2012.

[135] B. Li, L. Wang, and G. Casati, "Thermal Diode: Rectification of Heat Flux," *Physical Review Letters*, vol. 93, no. 18, pp. 1–4, Oct. 2004.

[136] N. Li, J. Ren, L. Wang, G. Zhang, P. Hänggi, and B. Li, "Colloquium: Phononics: Manipulating heat flow with electronic analogs and beyond," *Reviews of Modern Physics*, vol. 84, no. 3, pp. 1045–1066, Jul. 2012.

[137] R. Xie, C. T. Bui, B. Varghese, Q. Zhang, C. H. Sow, B. Li, and J. T. L. Thong, "An Electrically Tuned Solid-State Thermal Memory Based on Metal-Insulator Transition of Single-Crystalline VO_2 Nanobeams," *Advanced Functional Materials*, vol. 21, no. 9, pp. 1602–1607, May 2011.

[138] C. W. Chang, D. Okawa, A. Majumdar, and A. Zettl, "Solid-State Thermal Rectifier," *Science (New York, N.Y.)*, vol. 314, pp. 1121–1124, Jan. 2006.

[139] N. A. Roberts and D. G. Walker, "A review of thermal rectification observations and models in solid materials," *International Journal of Thermal Sciences*, vol. 50, no. 5, pp. 648–662, May 2011.

[140] C. Dames, "Solid-State Thermal Rectification With Existing Bulk Materials," *Journal of Heat Transfer*, vol. 131, no. 6, p. 061301, 2009.

[141] N. Yang, G. Zhang, and B. Li, "Thermal rectification in asymmetric graphene ribbons," *Applied Physics Letters*, vol. 95, no. 3, p. 033107, 2009.

[142] Y. Xia, P. Yang, Y. Sun, Y. Wu, B. Mayers, B. Gates, Y. Yin, F. Kim, and H. Yan, "One-Dimensional Nanostructures: Synthesis, Characterization, and Applications," *Advanced Materials*, vol. 15, no. 5, pp. 353–389, Mar. 2003.

[143] Y. Cui, Q. Wei, H. Park, and C. M. Lieber, "Nanowire nanosensors for highly sensitive and selective detection of biological and chemical species," *Science (New York, N.Y.)*, vol. 293, no. 5533, pp. 1289–92, Aug. 2001.

[144] Z. L. Wang and J. Song, "Piezoelectric nanogenerators based on zinc oxide nanowire arrays," *Science (New York, N.Y.)*, vol. 312, no. 5771, pp. 242–6, Apr. 2006.

[145] J. Xiang, A. Vidan, M. Tinkham, R. M. Westervelt, and C. M. Lieber, "Ge/Si nanowire mesoscopic Josephson junctions," *Nature nanotechnology*, vol. 1, no. 3, pp. 208–13, Dec. 2006.

[146] J. Cao, E. Ertekin, V. Srinivasan, W. Fan, S. Huang, H. Zheng, J. W. L. Yim, D. R. Khanal, D. F. Ogletree, J. C. Grossman, and J. Wu, "Strain engineering and one-dimensional organization of metal-insulator domains in single-crystal vanadium dioxide beams," *Nature nanotechnology*, vol. 4, no. 11, pp. 732–7, Nov. 2009.

[147] J. Wei, Z. Wang, W. Chen, and D. H. Cobden, "New aspects of the metal – insulator transition in single-domain vanadium dioxide nanobeams," *Nature Nanotechnology*, vol. 4, no. 141, pp. 420–424, 2009.

[148] S. Zhang, J. Y. Chou, and L. J. Lauhon, "Direct correlation of structural domain formation with the metal insulator transition in a VO_2 nanobeam," *Nano letters*, vol. 9, no. 12, pp. 4527–32, Dec. 2009.

[149] J. Wu, Q. Gu, B. S. Guiton, N. P. De Leon, L. Ouyang, and H. Park, "Strain-Induced Self Organization of Metal−Insulator Domains in Single-Crystalline VO_2 Nanobeams," *Nano letters*, vol. 6, no. 10, pp. 2313–17, 2006.

[150] A. Cavalleri, C. Tóth, C. Siders, J. Squier, F. Ráksi, P. Forget, and J. Kieffer, "Femtosecond Structural Dynamics in VO_2 during an Ultrafast Solid-Solid Phase Transition," *Physical Review Letters*, vol. 87, no. 23, pp. 1–4, Nov. 2001.

[151] M. M. Qazilbash, M. Brehm, B.-G. Chae, P.-C. Ho, G. O. Andreev, B.-J. Kim, S. J. Yun, a V Balatsky, M. B. Maple, F. Keilmann, H.-T. Kim, and D. N. Basov, "Mott transition in VO_2 revealed by infrared spectroscopy and nano-imaging," *Science (New York, N.Y.)*, vol. 318, no. 5857, pp. 1750–3, Dec. 2007.

[152] S. Kachi, K. Kosuge, and H. Okinaka, "Metal-Insulator Transition in V_nO_{2n-1}," *Journal of Solid State Chemistry*, vol. 6, no. 2, pp. 258–270, Feb. 1973.

[153] S. Kodambaka, J. Tersoff, M. C. Reuter, and F. M. Ross, "Germanium nanowire growth below the eutectic temperature," *Science (New York, N.Y.)*, vol. 316, no. 5825, pp. 729–32, May 2007.

[154] A. Jezowski and J. Rafalowicz, "Heat Flow Asymmetry on a Junction of Quartz with Graphite," *Phys. Stat. Sol.*, vol. 47, pp. 229–232, 1978.

[155] C. Starr, "The Copper Oxide Rectifier," *Physics*, vol. 7, no. 1929, pp. 15–19, 1936.

[156] A. Majumdar and P. Reddy, "Role of electron–phonon coupling in thermal conductance of metal–nonmetal interfaces," *Applied Physics Letters*, vol. 84, no. 23, p. 4768, 2004.

[157] A. F. Wells, *Structural Inorganic Chemistry*. OUP Oxford, 2012.

[158] J. Parker, "Raman Scattering from VO2 single crystals: A study of the effects of surface oxidation," *Physical Review B*, vol. 42, no. 5, pp. 3164–3166, 1990.

[159] S. Kachi, K. Kosuge, and H. Okinaka, "Metal-insulator transition in V_nO_{2n-1}," *Journal of Solid State Chemistry*, vol. 6, no. 2, pp. 258–270, Feb. 1973.

[160] Z. Tao, T.-R. Han, S. Mahanti, P. Duxbury, F. Yuan, C.-Y. Ruan, K. Wang, and J. Wu, "Decoupling of Structural and Electronic Phase Transitions in VO_2," *Physical Review Letters*, vol. 109, no. 16, pp. 1–5, Oct. 2012.

[161] J. M. Cullen and J. M. Allwood, "Theoretical efficiency limits for energy conversion devices," *Energy*, vol. 35, no. 5, pp. 2059–2069, May 2010.

[162] J. Billy, V. Josse, Z. Zuo, A. Bernard, B. Hambrecht, P. Lugan, D. Clément, L. Sanchez-Palencia, P. Bouyer, and A. Aspect, "Direct observation of Anderson localization of matter waves in a controlled disorder.," *Nature*, vol. 453, no. 7197, pp. 891–4, Jun. 2008.

[163] P. L. Mceuen, M. Bockrath, D. H. Cobden, Y. Yoon, and S. G. Louie, "Disorder, pseudospins, and backscattering in carbon nanotubes," *Physical Review Letters*, vol. 83, no. 24, pp. 5098–5101, 1999.

[164] C. Gómez-Navarro, P. J. de Pablo, J. Gómez-Herrero, B. Biel, F. J. Garcia-Vidal, a Rubio, and F. Flores, "Tuning the conductance of single-walled carbon nanotubes by ion irradiation in the Anderson localization regime.," *Nature materials*, vol. 4, no. 7, pp. 534–9, Jul. 2005.

[165] C. M. Aegerter and G. Maret, "Coherent Backscattering and Anderson Localization of Light," *Progress in Optics*, vol. 52, pp. 1–62, 2009.

[166] H. Hu, A. Strybulevych, J. H. Page, S. E. Skipetrov, and B. a. van Tiggelen, "Localization of ultrasound in a three-dimensional elastic network," Disordered Systems and Neural Networks; Mesoscale and Nanoscale Physics, May 2008.

[167] T. R. Kirkpatrick, "Localization of Acoustic Waves," *Physical Review B*, vol. 31, no. 9, pp. 5746–5755, 1985.

[168] M. Fink, "Time Reversed Acoustics," *Physics Today*, no. March, 1997.

[169] a. Przadka, S. Feat, P. Petitjeans, V. Pagneux, a. Maurel, and M. Fink, "Time Reversal of Water Waves," *Physical Review Letters*, vol. 109, no. 6, p. 064501, Aug. 2012.

[170] S. R. Nagel, G. S. Grest, and A. Rahman, "Phonon Localization and Anharmonicity in Model Glasses," *Physical Review Letters*, vol. 53, no. 4, pp. 1–4, 1984.